Quantification of aeroacoustic noise sources from wind turbines

Christina Ekrem Dimmen

A master's thesis in Energy

Geophysical Institute
University of Bergen

June 01, 2022

Acknowledgements

This 60 ECTS master thesis is written as a part of the Integrated Masters programme in Energy at the Geophysical Institute, University of Bergen.

First and foremost, I would like to express my sincere gratitude to my supervisor Mostafa Bakhoday Paskyabi for giving me the opportunity to write this thesis, always having faith in me and pushing me to do my best. Thank you for the guidance along the way, for letting me use your code for the PE model and for providing feedback on the analysis and results.

I would also like to extend my thanks to Christof Ocker for providing me with important experimental data and for answering my requests even when on parental leave. A thank you to Fabio Casagrande Hirono for publishing his code on the Amiet model for open use. Thanks should also go to the University of Bergen for the financial grant allowing me to take part in the EERA Deep Wind conference.

Further, I am so grateful to all of my friends and fellow students that I have had the pleasure of spending the last five years with. I will always appreciate this time of our life. A special thanks go to my master group Tore, Martine, Tiril and Adrian. This thesis would have been significantly more difficult without your daily support, encouragement, help and entertainment.

To my loving roommates Torill and Johanne, thank you for making our apartment feel like home. I always look forward to seeing your kind faces after long days at the university. A big thank you to Katharina for proofreading my thesis and for always being just a call away. Lastly, I would like to thank my family for the unconditional support and love throughout my life and especially in this last year.

Christina Ekrem Dimmen
Bergen, June 01, 2022

Abstract

One of the major environmental concerns regarding wind energy is an increase in noise levels, both in the atmosphere and the ocean. In this study, the generation and propagation of aeroacoustic noise from wind turbines were studied using available measurements together with several signal processing tools, as well as some well-known models within the field.

The thesis starts by introducing some general and more advanced concepts in regard to wind energy and aeroacoustics. Observational measurements conducted in a gust wind tunnel on a scaled wind turbine model were used to quantify noise characteristics from wind turbines. The experiment was conducted using 48 microphones in a ring array, with a known distance from the source. Then, a simple beamforming algorithm based on delay-and-sum in both 1D and 2D has been applied to identify the distribution of acoustic source strength on the turbine blade and subregions. However, our beamforming tool did not account for the sound source to be rotating and an idealised case with a fixed source has therefore been provided for the illustration of the method.

An open-source program for the Amiet model was adjusted for studying the turbulence interaction and noise generation on the same NACA4412-airfoil, with some simplifications applied. Next, the low-frequency Parabolic Equation model (PE-model) for an inhomogeneous atmosphere was used to study the effect of different atmospheric stability conditions on noise propagation from a wind turbine. Tests for three stability conditions (stable, neutral, and unstable) for variations of source frequencies, as well as for different topography were presented and discussed.

The studies conducted in this thesis illustrate the complexity of aeroacoustic noise and the different parts that need to be accounted for in the development of new wind farms, both onshore and offshore.

Contents

1 Introduction **1**
1.1 Background . . . 1
1.1.1 The evolution of wind turbines . . . 1
1.1.2 The role of wind power in the current energy transition . . . 2
1.2 Motivation . . . 4
1.2.1 Positive impacts of wind power . . . 4
1.2.2 Negative impacts of wind power . . . 5
1.3 Objectives . . . 6
1.4 EERA DeepWind Conference 2022 . . . 7

2 Theory **8**
2.1 Fundamental acoustics . . . 8
2.1.1 Sound and noise . . . 8
2.1.2 Quantification of sound . . . 9
2.1.3 Intensity Level (IL) and Sound Pressure Level (SPL) . . . 9
2.1.4 Frequency spectrum . . . 10
2.1.5 Turbulence spectra . . . 11
2.2 Structure and design of a wind turbine . . . 11
2.2.1 Aerodynamics . . . 13
2.3 Sound generation . . . 15
2.3.1 Background Noise . . . 15
2.3.2 Mechanical noise . . . 15
2.3.3 Aerodynamical noise . . . 17
2.4 Sound propagation in air . . . 23
2.4.1 Directivity . . . 23
2.4.2 Atmospheric factors . . . 24
2.4.3 Terrain effects . . . 27

3 Measurements and data **28**
3.1 Noise measurements from wind turbines . . . 28
3.1.1 In Situ . . . 28
3.1.2 Scaled wind turbine in a wind tunnel . . . 29
3.2 Data used in this thesis . . . 29
3.2.1 Experimental dataset from Stuttgart . . . 29
3.2.2 FINO1 data . . . 32

4 Methods **33**
4.1 Signal processing 33
4.1.1 Spectral analysis 33
4.1.2 Time-frequency analysis 34
4.2 Localization models 35
4.2.1 Delay-and-sum beamforming 35
4.2.2 Amiet model 37
4.3 Propagation model 39
4.3.1 Parabolic equation method 40

5 Results and discussion **44**
5.1 Noise generation 44
5.1.1 Histogram and statistical calculations 45
5.1.2 Power spectrum 49
5.1.3 Sound pressure levels 52
5.1.4 1/3 octave band filter 52
5.1.5 Spectrogram 54
5.1.6 Beamforming 57
5.1.7 Amiet model 59
5.2 Propagation of noise 65
5.2.1 Parabolic equation model 65

6 Summary and conclusion **79**

List of Tables

3.1 Technical details of the wind tunnel test site. 30

4.1 Variables for the idealised wind and temperature profiles used in the parabolic equation model. 42

5.1 The calculated mean value, variation, standard deviation, skewness and kurtosis of the measured sound pressure for all measured time signals. . 48
5.2 Important values from FINO1 dataset used in further analysis. 59
5.3 Airfoil geometry for the NACA4412 airfoil on a scaled wind turbine. . . 60
5.4 Values of transmission loss [dB] for all three stability conditions at varying source frequencies measured at a range of 1500 m and 3000 m. No terrain. 71
5.5 The change in transmission loss between 1500 m and 3000 m for three heights and varying atmospheric stabilities and frequencies. No terrain. 72
5.6 Values of transmission loss [dB] for all three stability conditions at varying source frequencies measured at a range of 1500 m and 3000 m. With terrain. 77
5.7 The change in transmission loss from a range of 1500 m to 3000 m for three heights, varying atmospheric stabilities and frequencies. Including terrain. 78

List of Figures

1.1 Size evolution of wind turbines . . . 2
1.2 Norwegian offshore wind resources . . . 4

2.1 Sound pressure level of wind turbine . . . 10
2.2 A-weighting filter . . . 11
2.3 Energy spectrum of turbulence. . . . 11
2.4 Illustration of HAWT and VAWT. . . . 12
2.5 Foundation types . . . 13
2.6 Lift and drag forces on an airfoil . . . 14
2.7 Generation of lift . . . 14
2.8 Mechanical noise . . . 16
2.9 Frequency spectra for 75 kW WT. . . . 16
2.10 Aerodynamic sources. . . . 17
2.11 Turbulent boundary layer trailing edge noise. . . . 18
2.12 Separation-stall noise . . . 19
2.13 Laminar boundary layer vortex shedding noise. . . . 20
2.14 Tip vortex formation noise. . . . 21
2.15 Trailing edge bluntness vortex shedding noise. . . . 22
2.16 Turbulent inflow noise. . . . 23
2.17 Directivity . . . 24
2.18 Absorption of sound in the atmosphere . . . 25
2.19 Logarithmic wind speed profile with height. . . . 26
2.20 Wind-induced refraction on acoustic rays . . . 27

3.1 Test site, Stuttgart . . . 30
3.2 NACA4412 airfoil dimensions . . . 31
3.3 Microphone array . . . 31

4.1 Delay and sum . . . 35
4.2 Example of two-dimensional delay-and-sum . . . 37
4.3 Amiet model setup . . . 39
4.4 Wind and temperature profile for three different stability conditions . . . 43

5.1 Timeseries of sound pressures at a wind speed of 5 m/s and a 0 degree pitch . . . 45
5.2 Histogram of averaged sound pressures for varying pitch angles with a wind speed of 5 m/s and 7 m/s. . . . 46

5.3 Histogram of averaged sound pressures for varying pitch angles with a wind speed of 11 m/s and 13 m/s. 47
5.4 Power spectrum for varying pitch angles and wind speeds 50
5.5 Power spectrum for wind speeds of 5 m/s and 13 m/s 51
5.6 Power spectrum for pitch angles of 2 degrees and 8 degrees 51
5.7 Sound pressure level as a function of the pitch angle and the relative velocity at the rotor tip 52
5.8 Measured noise levels with $1/3$ octave band filter for a 5 m/s wind speed 53
5.9 Measured noise levels with $1/3$ octave band filter for 13 m/s windspeed 54
5.10 Spectrogram for varying pitch angles for a wind speed of 5 m/s. 55
5.11 Spectrogram for varying pitch angles for a wind speed of 13 m/s. 56
5.12 Spectrogram for varying wind speeds with a pitch angle of 2 degrees. . 56
5.13 Spectrogram for varying wind speeds with a pitch angle of 8 degrees. . 57
5.14 Delay-and-sum beamforming 58
5.15 Acoustic source map, 5 m/s 58
5.16 Acoustic source map, 13 m/s 59
5.17 Turbulence intensity 59
5.18 Pressure jump and source strength distribution over airfoil 61
5.19 Normalised directivity under various conditions 62
5.20 Normalised directivity for a subcritical gust 63
5.21 Near-field radiation over the 2D cut of airfoil 64
5.22 Transmission loss for three different stability conditions and for varying frequencies. No terrain 66
5.23 Transmission loss for an unstable atmosphere at three different heights. No terrain 68
5.24 Transmission loss for a neutral atmosphere at three different heights. No terrain 69
5.25 Transmission loss for a stable atmosphere at three different heights. No terrain 70
5.26 Transmission loss for three different stability conditions and for varying frequencies. With terrain. 73
5.27 Transmission loss for an unstable atmosphere at three different heights. With terrain. 74
5.28 Transmission loss for a neutral atmosphere at three different heights. With terrain. 75
5.29 Transmission loss for a stable atmosphere at three different heights. With terrain. 76

Chapter 1

Introduction

1.1 Background

The European Union (EU) has pledged to reach net-zero greenhouse gas emissions by 2050, abating the 3.7 gigatonnes of CO_2-equivalents it is currently emitting per year (European Environment Agency, 2021; European Parliament, 2019). To reach this goal, a rapid shift towards large scale renewable energy must occur.

1.1.1 The evolution of wind turbines

The harvesting and utilisation of wind energy have been practised by humans for centuries, with simple wind devices dating back thousands of years. The first designs of the vertical axis windmills stem all the way back to the Persian-Afghan border around 200 BC, while the horizontal axis windmill from the Netherlands was developed much later (1300 AD) and was often used to grind grain or pump water (Kaldellis and Zafirakis, 2011). The first known modern wind turbine used for the production of electricity was built in Scotland in 1887 by Professor James Blyth, and by the beginning of the 1900s, there was a large use of small wind-electric generators in several countries (Price, 2005).

After World War II, due to a shortage of fuels and an increasing demand for electricity, a more widespread interest in wind energy arose leading to new research going into understanding the science of wind energy and wind turbines. In more economically developed countries, multiple research and development programmes for wind energy were initiated during the 1970s, and significant technological advances were made (Fleming and Proben, 1984).

With these advances, turbine sizes have increased rapidly in recent decades - both in height and blade length - generating more energy per turbine. The typical wind turbines in the 1980s had a rated capacity of 0.075 megawatts (MW) and a rotor diameter of 17 m, see Figure 1.1, with modern onshore wind turbines today generating an output of around 2-5 MW with an average rotor diameter of 125 m (in 2020) (Office of Energy Efficiency and Renewable Energy, 2021b). Up-scaling of wind turbines is mainly driven by cost reductions, making electricity generated from wind turbines a competitive energy source. The more energy generated per turbine, the fewer turbines

are needed, leading to lower manufacturing and installation costs. The optimum sizes for both onshore and offshore turbines are still being explored, and with larger turbine blades and higher towers, some issues are arising.

Transportation of large turbine blades for onshore installations is considered a complex operation because their shape and form after construction can not be bent or changed in any way. This limits the radius that the trucks can turn and the routes they can take. The topography and possible obstacles like bridges, highway overpasses or roundabouts, must be reviewed and expensive altercations to the roads and shores may be needed (Office of Energy Efficiency and Renewable Energy, 2021b). Any further increase in the size of onshore turbines will therefore be restricted by logistic constraints, as well as regulations concerning noise and visibility that will be discussed further in subsection 1.2.2. Offshore up-scaling, on the other hand, will be easier due to the fact that it can be engineered at industrial ports and transported directly by ships to the site (International Energy Agency, 2013).

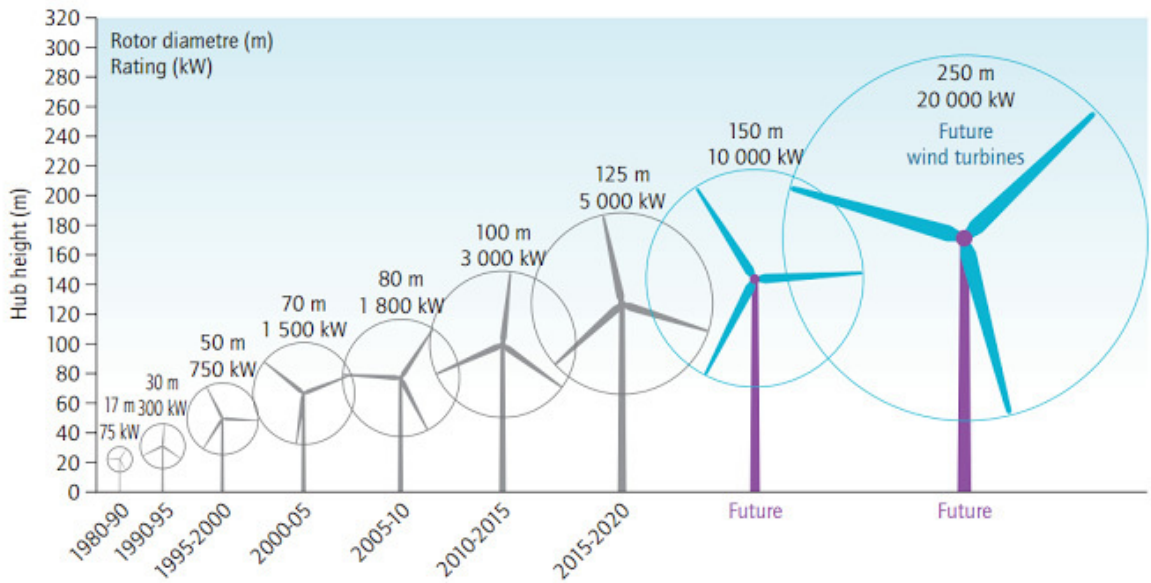

Figure 1.1: Illustration of the size evolution of wind turbines since 1980 and prospect. Figure from International Energy Agency (2013).

1.1.2 The role of wind power in the current energy transition

As other economies struggled under the weight of continuously new lockdowns caused by Covid-19 in the last couple of years, additions of renewable sources of energy increased by 3% in 2020, the fastest rate it has had in two decades (Cozzi and Gould, 2021; IEA, 2021). The wind industry had a growth of 93 GW in 2020, largely driven by installations in China, and the industry is expected to exceed 1 TW in the global cumulative installation of onshore and offshore installations by 2025 (Lee and Zhao, 2021).

Wind energy in Europe

In Europe, wind energy currently covers 16% (approximately 220 GW) of the annual electricity demand, saving 118 million tonnes of CO_2-equivalents per year. By 2030 it is estimated an installed wind energy capacity of 350 GW, supplying up to 24% of the electricity demand and save 270 million tonnes of CO_2-equivalents - the same as Spain's annual CO_2-emissions (Wind Europe, 2022a). Denmark is, not surprisingly given its history, the country with the highest wind energy shares in Europe, with a total of 46% of its electricity being supplied from wind farms (Wind Denmark, 2022).

The European Commission predicts that wind energy will be the technology providing the largest contribution to the EU renewable energy targets for 2020 and beyond. There are numerous research and innovation projects already established in the EU, aiming to lower the cost and increase the performance and reliability of wind energy technology, especially offshore (European Commision, 2022).

Wind energy in Norway

Norway is one of the countries with the best resources of wind in Europe, as shown in Figure 1.2. This can be credited to the long coastline with direct access to the Atlantic Ocean and high mountains. Wind energy has met a lot of resistance amongst the population in Norway, with demonstrations focusing on the wrecking of nature, noise and disturbance of wildlife. Even with this negative publicity, Norway installed a record of 1.5 GW in 2020, all onshore (European Commision, 2022). Amongst these installations was the Fosen Vind Complex, with a capacity of 1 GW as the largest onshore project in Europe (Statkraft, 2021). At the end of 2021, Norway had an installed capacity of 4650 MW from wind energy (NVE, 2022c).

Offshore wind energy market

In 2010, offshore wind was still a relatively new and developing technology but has since seen a rapid maturity in technology and lower cost. Between 2010 and 2019, there was a ninefold increase in cumulative installed capacity, from 3 GW to 28 GW (International Renewable Energy Agency, 2020). Europe is the global leader in the offshore wind industry, accounting for over 80% of the installed capacity in 2018 (IEA, 2019).

With larger areas available, as well as more stable and stronger wind resources, the International Renewable Energy Agency (IRENA) predicts that the offshore wind market will grow significantly over the next three decades. They await a rapid increase to a total capacity of 228 GW in 2030 and as much as 1000 GW in 2050 (IRENA, 2019).

Currently, turbines are being installed in 40 metres of water depths up to 80 kilometres from shore. These turbines, with monopile or jacket foundations rooted in the seabeds, are restricted to waters less than 60 metres in depth (Equinor, 2022). Given that up to 80% of the available offshore wind resources in both Europe and Japan, two of the largest producers of offshore wind energy, are in waters deeper than 60 metres,

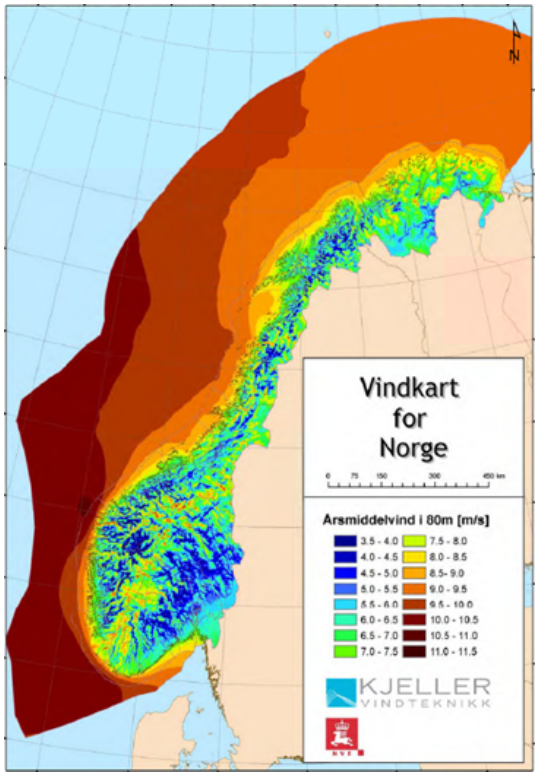

Figure 1.2: Map over the Norwegian offshore wind resources, made by Kjeller Vindteknikk (2009) on behalf of The Norwegian Water Resources and Energy Directorate (NVE).

this imposes a big technological limit (EU-Japan Centre, 2021). Floating wind farms are therefore one of the most sophisticated developments in ocean energy technologies, offering many important opportunities (IRENA, 2019).

1.2 Motivation

1.2.1 Positive impacts of wind power

Wind energy is considered one of the most environmentally friendly and cleanest energy sources, with many positive impacts both from local and global perspectives (European Commision, 2022). The long term impact on our environment is in most aspects positive. There are many reasons why wind energy is considered a good choice, for instance:

1. It is cost-competitive compared to other energy sources. Mayor technology improvements and reduced installation costs mean that onshore wind is now in the same price category, and often cheaper than traditional fossil fuels (Amim, 2015). In 2020, several new onshore wind projects, with a total installed capacity of 100 GW, were commissioned with a cheaper LCOE (Levelized Cost Of Electricity) than the most cost-efficient fossil-fueled power generation (International Renewable Energy Agency, 2020).

2. It produces no greenhouse gases after production and therefore reduces the threat

posed by climate change (Wind Europe, 2022a).

3. It has one of the lowest CO_2-emissions and energy use throughout its life cycle. Compared to the carbon footprint of coal and natural gas, releasing roughly 980 g CO_2/kWh and 465 g CO_2/kWh respectively, wind energy is considered close to emission-free with a carbon footprint of only 11 g CO_2/kWh (Office of Energy Efficiency and Renewable Energy, 2021a). The energy payback time, i.e. the required period in which the wind turbine can produce the same amount of electricity as the total energy consumed of its entire life cycle, varies from around 3-9 months for onshore turbines. For offshore wind turbines, the energy payback time is usually a bit longer (Pichs Madruga et al., 2012).

4. It generates no air pollutants when in production. Exposure to high-level air pollutants over time can also cause a variety of serious health problems, like respiratory infections, heart diseases and lung cancer (World Health Organization, 2019). Wind energy is therefore a wiser energy source choice when talking about health impact.

5. It emits no micro-plastics, which are also a large cause of lung cancer and respiratory diseases reducing the general life expectancy (Wind Europe, 2022b). Microplastics come from thermoplastics, like acrylic, polyester, polypropylene, Teflon and nylon, and are becoming an ever-increasing issue for the environment and our health. Even though wind turbines contain plastic in many of their components, they are not made from the thermoplastics that microplastic comes from. The blades on the turbine, that suffers the most tear, are made up of composite fibres, consisting mostly of glass fibre from sand (70%) and thermosetting plastic (30%)(Carstairs, 2021; Svensk Vindenergi, 2021). Compared to car tires or clothes, a wind turbine emits significantly fewer microplastics during its lifetime, and there is no scientific consensus to support claims that wind turbines increase microplastic pollution (Carstairs, 2021; NORWEA, 2021).

6. It uses almost no water in operation, unlike other electric power plants (i.e. nuclear and thermal power plants using water for cooling purposes). Energy production is accountable for 44% of the European water consumption, more than both agriculture, public water supply and industry. An important step towards safekeeping the water resources in Europe is therefore to replace nuclear and thermal power stations with wind energy (Koulouri and Moccia, 2014).

7. It is almost fully recyclable, with between $85-90\%$ of the wind turbines' total mass being recyclable. Turbine blades have, however, represented a challenge for the industry, due to their complex composite material that requires a special recycling process (Wind Europe, 2020). Coming up with a solution to this is of high importance for the wind industry, as the number of decommissioned wind turbines in the next couple of years will grow rapidly.

1.2.2 Negative impacts of wind power

Despite broad public support for renewable energy, the development of wind farms is often met with resistance from a local level. Although some opposition to wind power

often is based on pure misconceptions about the technology, it is important to understand the underlying issues and concerns behind this personal stand, such as the aesthetics, land use, impact on birds, fish and mammals, and noise levels (NREL, 2005).

An issue that arises when the sun is low in the sky, is light shining through the wind turbine. The turbine blades rotate, casting a moving shadow over nearby areas, perceived as a "flicker". This shadow flickering effect is the largest close to the turbine and will have both daily and seasonal variability depending on the position of the sun and the cloud cover (NVE, 2022b). Wind project developers can use computer programs to estimate when, where and to what extent shadow flickering will be an issue when choosing sites and therefore reduce this issue already before the commission (Office of Energy Efficiency & Renewable Energy, 2011). When in operation, it is possible to shut down the wind turbines for shorter periods of time, for instance in the morning or evening, when the effect is most noticeable. This initiative is done by many onshore wind farms in Norway today (NVE, 2022b).

People living close to wind farms have numerous times reported various negative health impacts arising from wind turbine noise. For that reason, noise pollution is to be considered the most critical impact wind turbines have on the environment. In Norway, the noise regulation for wind turbines is more rigid than for other industries, as well as for roads and railways. Seeing as the noise varies with wind speed, direction, vegetation and other atmospheric factors (which will be discussed in section 2.4), many find this to be more disturbing than other noise sources, even with an upper noise level of 45 dB, the same noise level as a modern fridge (Home-X, 2022; NVE, 2022a). Noise from wind turbines is therefore a key subject in studies and research in the pursuit of improving the overall performance and the environment in close proximity to the turbines.

1.3 Objectives

The primary objective of this thesis is to study the generation and propagation of aeroacoustic noise from wind turbines, using available measurements and a variety of signal processing tools. The thesis starts by introducing some general and a few more advanced concepts in regard to wind energy and aeroacoustics, before moving on to looking at experimental datasets where the noise characteristics from wind turbines will be studied.

We will be using the Amiet model to understand the turbulence interaction and noise generation on an airfoil. Next, we move on to the sound propagation, where the low-frequency Parabolic Equation model (PE-model) for an inhomogeneous atmosphere will be used to study the effect of different atmospheric stability conditions on noise propagation, with and without terrain and for varying source frequencies. A deeper understanding of noise arising from wind turbines will make it possible to drive the technology and the utilisation of wind energy further in the future.

1.4 EERA DeepWind Conference 2022

As a part of my thesis, I had the opportunity to attend the annual European Energy Research Alliance (EERA) DeepWind conference in January 2022. Due to COVID-19, restrictions on travel and social gatherings made it not possible to attend the conference physically, and all presentations were conducted online. In October, an abstract was sent in on my thesis with the expected discoveries and further work described. The current work was presented in front of a panel of experienced people in the offshore wind industry/field of study. This was a great opportunity to present my work, as well as learn from ongoing research and innovations related to offshore wind technologies

Chapter 2

Theory

A wind turbine transforms kinetic energy in the wind, from mechanical energy in the shaft to electrical energy in a generator (Office of Energy Efficiency & Renewable, 2013). The maximum available energy, E_{max} in joule [J], extracted from the wind can be calculated with the formula:

$$E_{max} = \frac{1}{2} m V_0^2 = \frac{1}{2} \rho A V_0^3, \tag{2.1}$$

where m is the mass flow, V_0 is the wind speed, ρ is the density of the air and A is the rotor area. The power increases with the cube of wind speed and linearly with density and area, as seen in the formula. Available wind conditions at the site are therefore one of the first things to look into in a planning process. In practice, the maximum available power from Equation (2.1) is not obtainable, so a power coefficient C_p is defined as the ratio between the actual power output and the maximum available power given in the above equation. Modern wind turbines operate with C_p up to 0.5, with a theoretical maximum efficiency given by Betz limit with $C_p = \frac{16}{27} = 0.593$ or 59.3% (Hansen, 2008).

2.1 Fundamental acoustics

In preparatory to the following chapters, a number of basic acoustic concepts and terminology will be introduced. For more details regarding the theory discussed here, see Dowling and Williams (1983) and Kinsler et al. (1999), which has been used in preparation for this section.

2.1.1 Sound and noise

Sound exists as the result of weak pressure disturbances, or oscillations, travelling in an elastic media (e.g. air, water, solids), causing small variations in the density and velocity of the wave. These disturbances occur from vibrating surfaces or turbulent fluid flows and generate energy across the media. The more energy generated from the vibrations, the louder the sound gets. The way to measure sound levels is with the decibel scale [dB] (Vargas, 2008).

Noise is an unwanted sound, that has both an objective, physical component, and a subjective component, e.g. the perception and reaction to a sound varies from person to person, and it can be difficult to assess the extent of the noise and how it affects the nearby environment. It is defined as noise if the sound is of no use or value, or if it causes annoyance, distress or pain (Harrison, 2011; Vargas, 2008).

2.1.2 Quantification of sound

The sound pressure, P, is defined as the force of a sound on a surface area perpendicular to the direction of the sound, expressed in pascals [Pa]. 1 Pa is defined as 1 N/m^2 in the SI system of units. Sound intensity, I, is defined as the rate of power transmission through a surface, expressed in watts per square meter [W/m^2]. If we consider ourselves in a free-field environment, i.e a region in space where sound may propagate free from any form of obstruction, the sound intensity is defined as,

$$I = \frac{P^2}{2\rho c}, \tag{2.2}$$

where ρ is the density of air [kg/m^3], and c is the speed of sound [m/s]. The total energy produced from a sound source per unit of time is called the sound power, W, measured in watts. The power from a sound source emitting spherical waves can be written as:

$$W = \int_A I dA = 4\pi r^2 I, \tag{2.3}$$

where A and r are the area and radius of the spherical wave.

2.1.3 Intensity Level (IL) and Sound Pressure Level (SPL)

Sound pressures and intensities are typically described using the numerically more compact logarithmic scale. A reason for this is that even though the fluctuations are small, the range in amplitudes is very large for both sound pressures and intensities; the audible intensities range from approximately 10^{-12} to 10 W/m^2. The intensity level, IL, of a sound is defined as

$$IL = 10\log(I/I_{ref}), \tag{2.4}$$

where I_{ref} is a reference intensity, IL is expressed in decibels ref. to I_{ref} (dB *re* I_{ref}) and "log" is the logarithm to base 10. Since the intensity and pressure can be related by Equation (2.2) when ρc is the same, the intensities in Equation (2.4) can be replaced with expressions of the pressure:

$$SPL = 20\log(P/P_{ref}), \tag{2.5}$$

where SPL is expressed in dB *re* P_{ref}. P_{ref} is the reference pressure amplitude in pascals [Pa]. In the air, the internationally agreed reference value of pressure is given as 2×10^{-5} Pa and corresponds to the threshold of hearing (0 dB). The sound pressure level will depend on factors such as distance from the source, the directivity of the source and the propagation path.

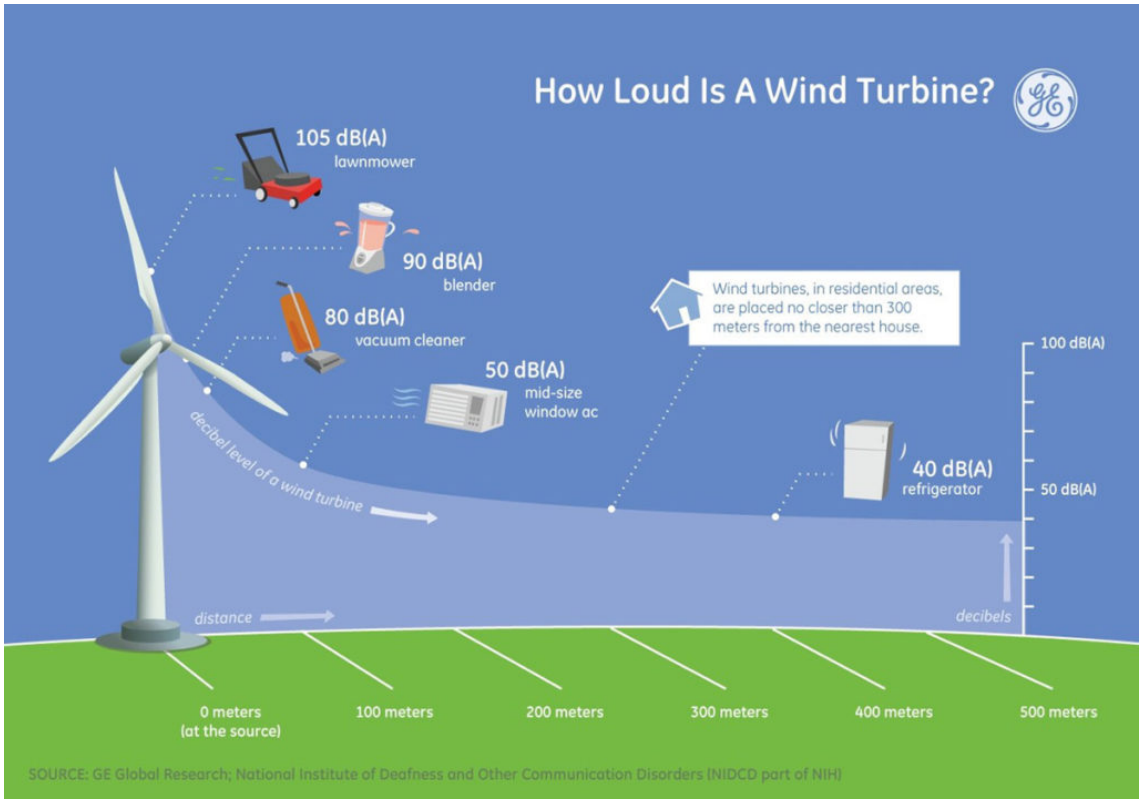

Figure 2.1: The sound pressure level of a typical wind turbine at different ranges. Figure from GE Global Research (2014).

2.1.4 Frequency spectrum

Sound rarely consists of single-frequency signals and is usually a combination of multiple frequencies put together. The frequency spectrum of the acoustic source is a way of characterising the sound. Some commonly used spectrums are the octave band and the 1/3 octave band. An octave refers to the range between one frequency and its double or its half. There is one octave between the frequency 1000 Hz and the frequency 2000 Hz, and similarly between 1000 Hz and 500 Hz. An octave band is therefore a band where the highest frequency is twice the lowest frequency. To give an example, an octave filter with a centre frequency of 1 kHz has a lower frequency of 707 Hz and an upper frequency of 1.414 kHz (Dopico, 2020). A 1/3 octave band is between two frequencies with a ratio $2^{1/3} : 1$ and will give more detailed information about the structure of the noise than the octave band (Hansen, 1951). For a 1/3 octave filter with the same middle frequency of 1 kHz, we now get a lower frequency of 891 Hz and a higher frequency of 1.122 kHz.

The human ear can hear frequencies from about 20 Hz to 20 kHz and is built in such a way that it responds more strongly to certain frequencies than others. When sound meters assess the annoyance caused by a sound, they must take this sensitivity into account. One way of doing that is to weigh the sound pressure level in each frequency band by a factor. The most common factor or curve to use is 'A-weighting' (see Figure 2.2), measured in dBA, which emphasises the higher frequencies and de-emphasises the more audible lower frequencies (Hubbard and Shepherd, 1988).

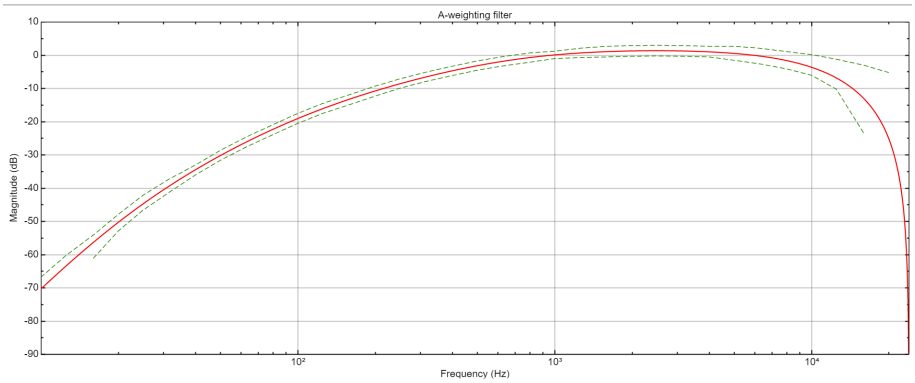

Figure 2.2: A-weighting filter plotted in Matlab.

2.1.5 Turbulence spectra

The turbulence spectra is an important concept in wind energy, as it gives the distribution of kinetic energy in the wind with respect to frequency. The energy is mainly concentrated in the high-frequency area, i.e. long wavelengths and large eddies, see Figure 2.3. Turbulent energy is gained at the expense of instabilities in a mean flow (Garratt, 1992), creating large eddies that dissipate to smaller and smaller eddies, eventually fading into viscosity.

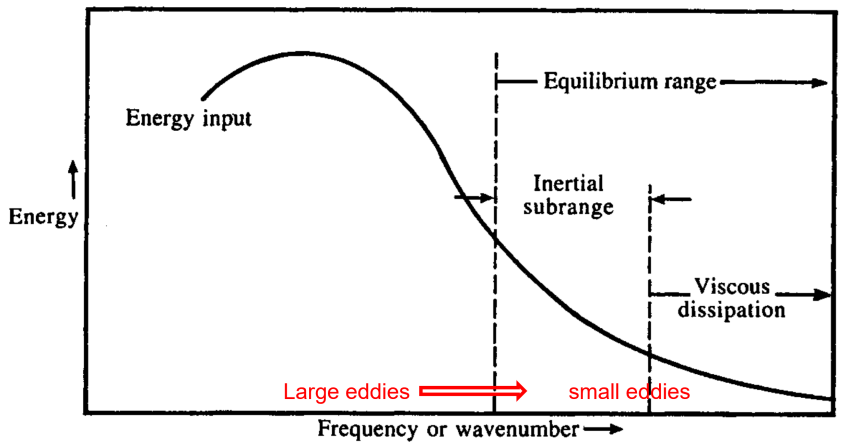

Figure 2.3: Schematic representation of the energy spectrum of turbulence. Figure adapted from Garratt (1992).

Turbulence intensity, TI, is a measure of the intensity of the wind velocity fluctuations in percentage [%], and can be found in the equation (Caires et al., 2019):

$$TI = \frac{\sigma_U}{U_{mean}} \tag{2.6}$$

where σ_U is wind speed standard deviation, and U_{mean} is the mean wind speed.

2.2 Structure and design of a wind turbine

Wind turbines are usually separated into two main categories based on their connection between the shaft and blades. If the blades are connected to a vertical shaft, the

turbine is called a vertical-axis machine (VAWT). Today, almost all commercial wind farms consist of horizontal-axis wind turbines (HAWT) (Office of Energy Efficiency & Renewable, 2013). This type of turbine is described in terms of the number of blades, the rotor diameter, the rated power and the type of control strategy. Figure 2.4 shows an illustration of both a HAWT and VAWT. When referring to wind turbines, the term WT is preferably used from now on for a HAWT, if not stated otherwise.

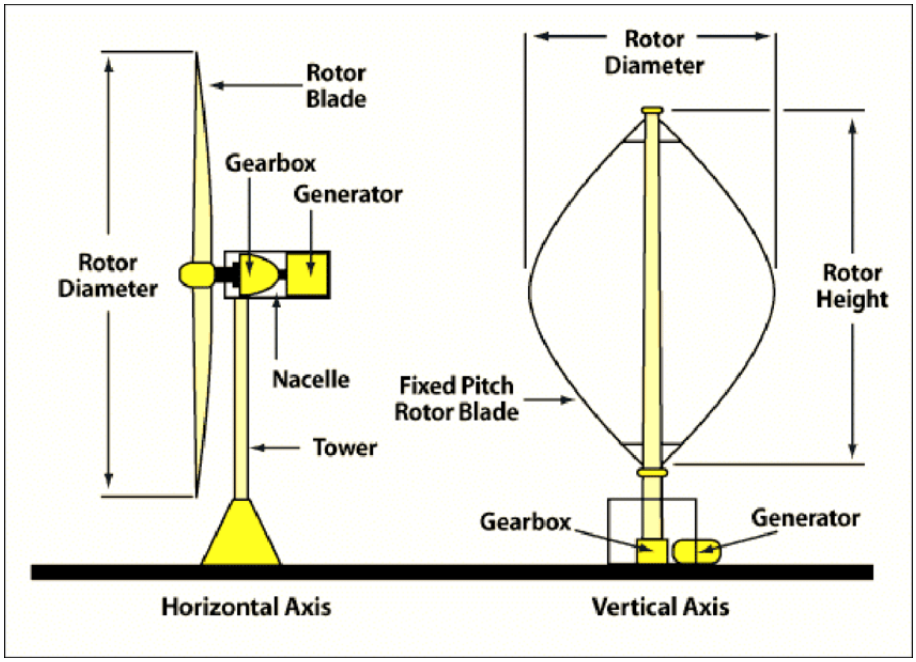

Figure 2.4: Illustration of HAWT and VAWT. Figure from Ba Alawi (2018).

A WT can be separated into five assembled parts (Office of Energy Efficiency & Renewable, 2013):

- Tower - the supporting structure of the turbine. The height of the tower is significant for the energy captured and electricity generated, due to the fact that wind speed increases with height. Winds above roughly 30 metres are also less turbulent, giving more stable electricity production and less fatigue loading on the mechanical parts (Brand et al., 2011).

- Rotor blades - usually two- or three-bladed. Both versions with their own advantages and disadvantages. The two-bladed turbines are cheaper to construct due to less material needed, but they have a higher rotational speed, i.e. they are perceived as more flickering. Because of that, most turbines today are three-bladed, as they appear calmer and less disturbing in the landscape. The aerodynamic efficiency of the turbine is also higher with three blades compared to two. Blades vary in length, from around 40 metres for a 1.5 MW turbine to a record 115 metres for the Vestas V236 - 15 MW turbine (Vestas, 2022).

- Rotor hub - the connection between the blades and the main shaft. The placement of the rotor can either be upwind or downwind. Downwind turbines have the tower positioned in front of the blades, creating a structural hindrance, while upwind turbines receive the wind directly. Studies show that WTs with downwind

rotors create more noise than upwind rotors when the aerodynamic wake from the tower interacts with the turbine blades. In addition to other performance issues, upwind WTs are generally preferred (Hubbard and Shepherd, 1988).

- Nacelle - the location of all the electrical components, like the gear-box, low- and high-speed shafts, generator and brakes. It sits on top of the tower and the yaw bearing that allows for rotation towards the changing wind direction.
- Foundation - the structure made for fixing the tower to the ground. There are several different types of foundations for both onshore and offshore WTs, see Figure 2.5. For floating WTs there are no solid foundations, instead, mooring lines with a form of anchoring system are used to safely keep the turbines in the required position. Depending on the seabed, type of mooring lines, cost etc. there are several anchoring techniques to choose from. Some examples are gravity-base, suction, drag-embedded and driven pile anchor (Floating Wind Turbunes, 2022).

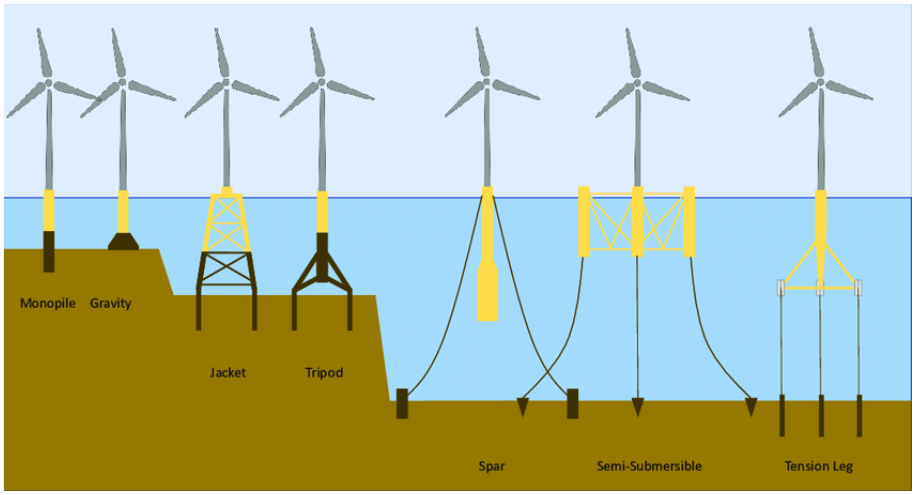

Figure 2.5: Common offshore wind foundation types. From left to right: monopile, gravity, jacket, tripod, spar, semisubmersible and tension-leg platform. Figure from Dornhelm et al. (2019).

2.2.1 Aerodynamics

Wind flowing across the turbine blades creates a difference in air pressure across the two sides giving ground for both lift and drag forces. These forces are the components perpendicular and parallel to the direction of the relative wind respectively. Figure 2.6 shows an illustration of the forces. When the force of the lift is stronger than the drag force, this causes the rotor to spin.

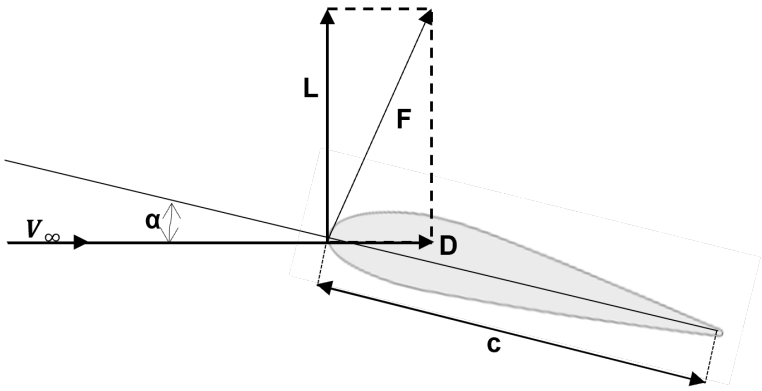

Figure 2.6: Illustration of lift and drag forces on an airfoil.

The lift and drag coefficients C_l and C_d are defined as:

$$C_l = \frac{L}{\frac{1}{2}\rho V^2 c}, \tag{2.7}$$

$$C_d = \frac{D}{\frac{1}{2}\rho V^2 c}, \tag{2.8}$$

where L is the lift force and D is the drag force, both in Newton, ρ is the air density, c is the chord length of the airfoil and V is the wind speed. Lift can be explained by the shape of the airfoil forcing the streamlines to curve around the geometry of the profile, as shown in Figure 2.7. To curve the streamlines, a pressure gradient is necessary and will work as a centripetal force. Far from the airfoil there will be atmospheric pressure, there will therefore be a lower than atmospheric pressure on the upper side of the airfoil (suction side) and a higher than atmospheric pressure on the lower side of the profile (pressure side) (Hansen and Did, 1998). This pressure difference is what generates the lifting force.

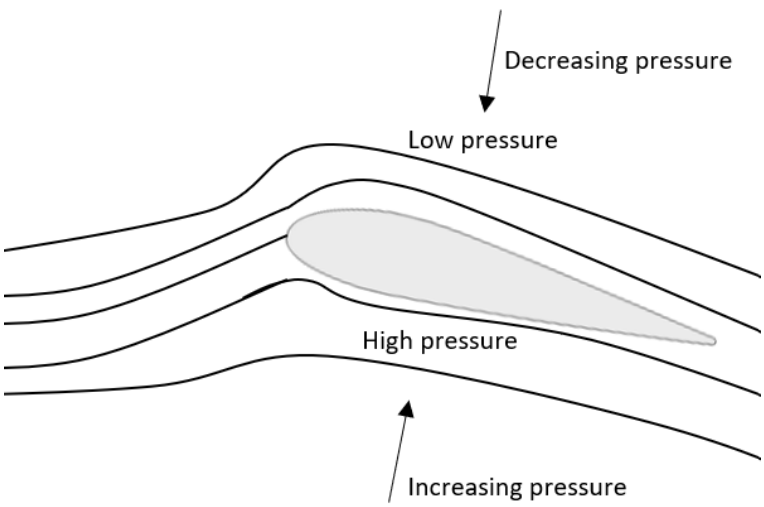

Figure 2.7: Explanation of the generation of lift.

The most important parameter of the airfoil is characterised by the lift-to-drag ratio, L/D, with the maximum lift-to-drag ratio on modern WTs being up to 200 times. Having a high ratio tends to increase the efficiency of the turbine (Hansen, 2008).

2.3 Sound generation

Noise from wind turbines ranges in frequencies from low inaudible values to higher values in the audible range. There are many components in a wind turbine that can generate noise, in general, the noise can be characterised as either mechanical or aerodynamical.

2.3.1 Background Noise

When estimating the total sound level from wind turbines, it is however important to first determine the background noise at the given site. Background noise can arise from several different sources and should be accounted for by site measurements prior to construction (without the turbine operating). Sources of background noise can be wind interacting with other objects, like trees, vegetation, housing and terrain. Natural wind noises can end up masking the wind turbine noise, due to the fact that their broadband spectra are similar to the ones of the wind turbines (Vargas, 2008). If the background noise levels are higher than the corresponding wind turbine noise levels, the WT noise will generally not be perceived. Human activities (farm harvesting, traffic etc.) and wildlife are other background noise sources.

2.3.2 Mechanical noise

Mechanical noise originates from components inside the turbine's hub knocking or moving against each other, for example in the gearbox, generator or the hydraulic system. These noise sources are illustrated in Figure 2.8. This gives rise to tonal and low-frequency vibrations that are transmitted in two ways. If the noise is directly radiated to the atmosphere, like the noise emitted by the gearbox through the openings in the nacelle, it is called airborne. To reduce the airborne noise, manufacturers have developed a type of wind turbine without gearboxes known as a direct-drive wind turbine. The rotor here is connected directly to the generator, allowing for easier installation and maintenance (ABB, 2019). Moreover, it is reducing the number of moving parts causing vibration and noise (Osmanbasic, 2020). The vibrations can also propagate through the different components and transmission elements to the nacelle casing and further down the tower before reaching the atmosphere. This indirect noise is called structure-borne and is the main contribution of mechanical noise (Szasz and Fuchs, 2010).

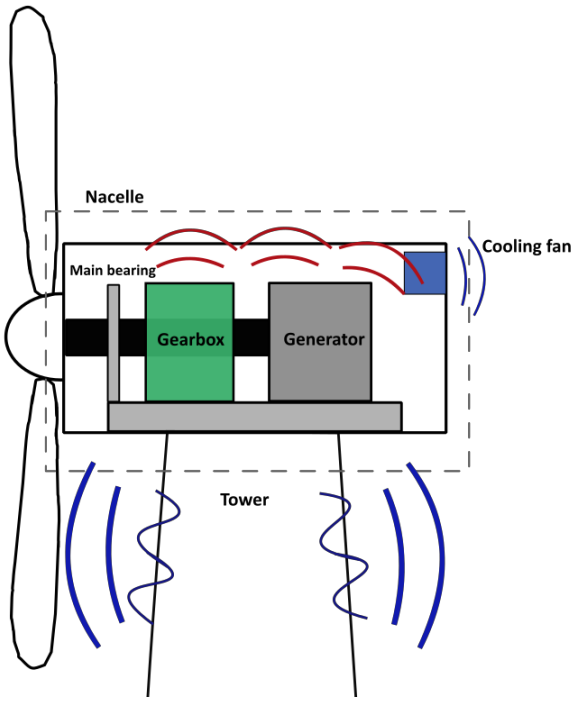

Figure 2.8: Examples of mechanical noise from the wind turbine nacelle. Figure based on INC Engineering Co. Ltd. (2022).

Figure 2.9 shows a typical 1/3 octave band for a small 75 kW WT measured by Ohlrich (Pinder, 1992). The mechanical noise spectra from the nacelle and the tower are more tonal than the 'smooth' and more broadband rotor noise. The aerodynamic noise is dominant in most frequency bands, except around 1000 Hz where noise from the nacelle contributes most to the overall level.

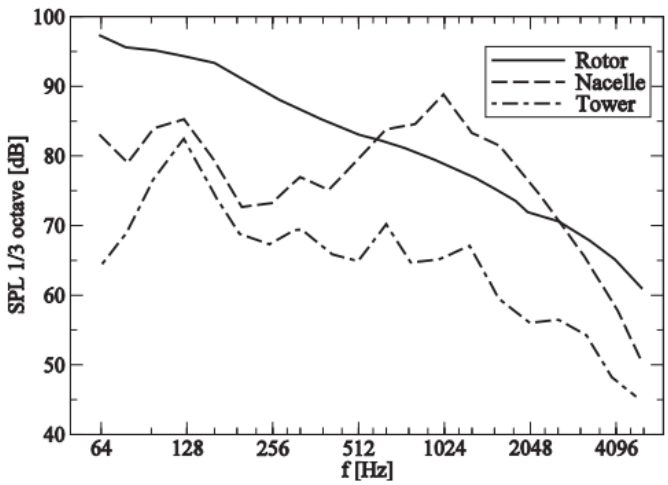

Figure 2.9: Typical noise frequency spectra of different components for a 75 kW WT. Figure from Pinder (1992).

Avoiding or damping the mechanical noise is possible, but requires a certain amount of maintenance and some added expenses for soundproofing or extra insulation material (Oerlemans, 2011). For modern large scale WTs such improvements are usually given and the mechanical noise can be neglected, while for small scale wind turbines and some VAWTs it will still have some contribution to the total acoustic sound pressure.

2.3.3 Aerodynamical noise

Aerodynamical noise is associated with the air flowing over the blades. This is typically the most dominant component of acoustic emissions from WTs. As Figure 2.10 shows, several complex flow phenomena occur around the blade, that each gives rise to some level of noise. The aerodynamic noise generally increases rapidly with the rotor speed. These noises are unavoidable and cannot be attenuated in the same manner as mechanical noise. The various aerodynamic noise mechanisms can be divided into three groups: inflow turbulent noise, tonal/low-frequency noise and airfoil self-noise. These mechanisms will be discussed further in the following sections.

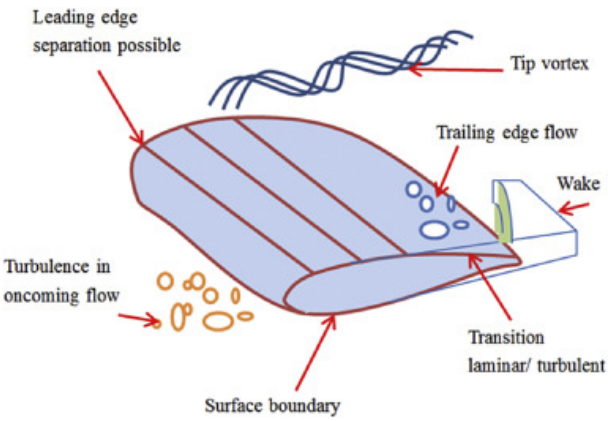

Figure 2.10: Sketch of aerodynamic sources from Liu (2017).

Some key measures for aerodynamical noise that should be mentioned are the Mach, Strouhal and Reynold numbers. These numbers are used in the empirical relations presented for each noise source. The Mach number is defined as the relative velocity at the blade v, over the speed of sound c_0 (Ocker et al., 2021):

$$M = \frac{v}{c_0}, \tag{2.9}$$

The rotor-based Strouhal number, being the ratio of inertial forces due to turbulence in the flow, is defined as (Engineering Toolbox, 2014):

$$St = \frac{fD}{v}, \tag{2.10}$$

where f is the frequency [Hz], $D = 2R$ is the rotor diameter [m] and v is the relative velocity [m/s]. Lastly, the Reynolds number is a measure of the inertia force to friction force, and can be expressed as :

$$Re = \frac{uL}{\nu}, \tag{2.11}$$

where u is the flow velocity [m/s], L is the characteristic length [m], and ν is the kinematic viscosity $[m^2/s]$.

Airfoil Self Noise

Airflow self-noise occurs as a result of the interaction between the airfoil and the flow. Turbulence in the airfoil boundary layer is produced and a broadband noise gets radiated as a result of the interaction of the flow with the trailing edge. Brooks et al. (1989)

have conducted measurements and formulated empirical relations to predict the noise source levels. The noise intensity for all the airfoil self-noise sources is directly proportional to the turbulent boundary layer displacement thickness, δ^*, and to the fifth power of the mean velocity or Mach number, M^5, and inversely proportional to the square of the distance between the airfoil trailing edge and the observer (Moriarty and Migliore, 2003).

By reference to Figure 2.10 and based on the findings by Brooks et al. (1989), the airfoil self-noise can be divided as follows:

- **Turbulent Boundary Layer Trailing-Edge Noise (TBL-TE)** is considered the most common source of noise from an airfoil and occurs when the turbulent boundary layer interacts with the trailing edge of the airfoil, see Figure 2.11. It usually takes place at high Reynolds numbers and moderate angles of attack (Brooks et al., 1989; Moriarty and Migliore, 2003). Turbulent boundary layer noise can appear on both sides of the airfoil, the sound pressure levels are therefore given for both the pressure and suction side as follows.

  The pressure side of the airfoil (subscript p):

$$\mathrm{SPL}_p = 10\log\left(\frac{\delta_p^* M^5 L\bar{D}_h}{r_e^2}\right) + A\left(\frac{St_p}{St_1}\right) + (K_1 - 3) + \Delta K_1. \tag{2.12}$$

  The suction side of the airfoil (subscript s):

$$SPL_s = 10\log\left(\frac{\delta_s^* M^5 L\bar{D}_h}{r_e^2}\right) + A\left(\frac{St_s}{St_1}\right) + (K_1 - 3), \tag{2.13}$$

  where $\delta^* = \delta^*(\alpha, Re_c)$ is the boundary layer displacement thickness and based on the angle of attack (α [deg]) and the Reynolds number (Re_c) based on the airfoil chord. The other parameters in Equations (2.12) and (2.13) are the span of the airfoil; L [m], the directivity function; D_h (see Equation (2.31) in subsection 2.4.1), the effective distance to observer; r_e [m], and an empirical spectral shape based on the Strouhal number; A. The Strouhal number is given as $St = (f\delta^*/U)$, where f is the frequency of the vortex shedding in hertz [Hz], and U is the local mean velocity of the flow [m/s]. Some other empirical relations that are used, $St_1 = 0.02M^{0.6}$, an amplitude function $K_1 = K_1(Re_c)$ and a corrective term for nonzero angles of attack $\Delta K_1 = \Delta K_1(\alpha, Re_{\delta^*})$ (Moriarty and Migliore, 2003; Vargas, 2008).

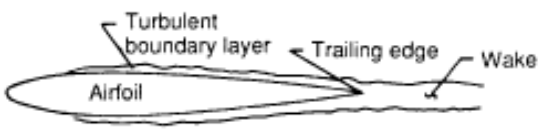

Figure 2.11: Turbulent boundary layer trailing edge noise.

- **Separation-Stall Noise (SEP)** occurs when the blade airfoil is operating at high angles of attack. When fully at stall, the noise radiates from the unsteady flow over the airfoil chord as a whole instead of just along the trailing edge. This is illustrated in Figure 2.12, where at small angles only boundary-layer separation is present, while for higher angles large-scale separation occurs. In fluid dynamics, a stall is defined as a sudden reduction in the lift as the angle of attack increases on the airfoil (SKYbrary Aviation Safety, 2020). Under certain conditions, the stall noise can produce amplitude modulation noise, i.e. regular variations in the sound pressure coming from the rotation of the turbine blades. This amplitude modulation is found to be the noise from wind turbines that causes the most annoyance compared to other environmental noise of the same level (Bertagnolio et al., 2019; Makarewicz and Gołębiewski, 2018). Because wind turbine blades often operate at high angles of attack, thus creating stall, this is a significant noise source (Moriarty and Migliore, 2003). Brooks et al. (1989) formulated the separation stall noise as:

$$\mathrm{SPL}_{\alpha} = 10\log\left(\frac{\delta_p^* M^5 L \bar{D}_h}{r_e^2}\right) + B\left(\frac{St_p}{St_2}\right) + K_2, \tag{2.14}$$

where B is a spectral shape function based on the Strouhal number and K_2 is an amplitude function in respect to the separation noise.

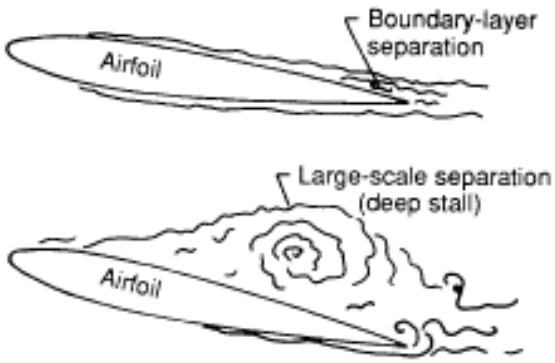

Figure 2.12: Separation-stall noise illustrated as an increase in the angle of attack.

The TBL-TE and SEP noise can be expressed together as:

$$SPL_{TOT} = 10\log(10^{SPL_p/10} + 10^{SPL_s/10} + 10^{SPL^{\alpha}/10}). \tag{2.15}$$

- **Laminar Boundary Layer Vortex Shedding Noise (LBL-VS)** is likely to occur with a lower Reynolds number, i.e for a laminar flow. A laminar boundary layer will be present over at least one side of the airfoil and develop into the trailing edge, illustrated in Figure 2.13. The noise from this source is coupled to a feedback loop between vortices being shed at the trailing edge and instability waves. The source of the noise occurs on the pressure side of the airfoil most of the time and is of a tonal nature because of feedback amplification. For large scale wind

turbines this noise source hardly exist since they operate at larger Reynolds numbers (> 1 million), especially at their blade tips (Moriarty and Migliore, 2003).

The empirical relation for the sound pressure level is given as:

$$SPL_{LBL-VS} = 10\log\left(\frac{\delta_p M^5 L\bar{D}_h}{r_e^2}\right) + G_1\left(\frac{St'}{St'_{peak}}\right) + G_2\left(\frac{Re_c}{(Re_c)_0}\right) + G_3(\alpha_*), \tag{2.16}$$

where the Strouhal number is defined as:

$$St' = \frac{f\delta_p}{U}, \tag{2.17}$$

$$St'_{peak} = St'_1 \times 10^{-0.04\alpha_*}, \tag{2.18}$$

and

$$St'_1 = \begin{cases} 0.18 & (Re_c \leq 1.3\times 10^5) \\ 0.001756 Re_c^{0.3931} & (1.3\times 10^5 \leq Re_c \leq 4.0\times 10^5) \\ 0.28 & (4.0\times 10^5 < Re_c) \end{cases}, \tag{2.19}$$

with Re_c being a reference Reynolds number. Most other variables in Equation (2.16) are the same as those in Equation (2.12): δ_p is the boundary layer thickness on the pressure side of the airfoil and G_1, G_2 and G_3 are empirical shape functions for fitting the experimental data (Vargas, 2008).

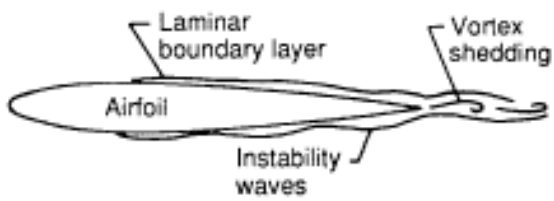

Figure 2.13: Laminar boundary layer vortex shedding noise.

- **Tip Vortex Formation Noise (TIP-VF)** stems from the interaction of the tip vortex with the blade tip and trailing edge close to the blade tip. The flow promoted by the pressure differential between the airfoil surfaces assumes a three-dimensional characteristic due to no boundary limitation at the blade's tip, see Figure 2.14. The flow is convected from the pressure side to the suction side of the airfoil, creating a tip vortex as shown in Figure 2.14. Tip vortex formation noise is usually less than the sound pressure level from trailing edges but can have a significant contribution to high-frequency broadband noise (Moriarty and Migliore, 2003; Vargas, 2008).

The empirical function for TIP-VF noise is found to be:

$$SPL_{TIP-VF} = 10\log\left(\frac{M^2 M_{max}^3 l^2 \bar{D}_h}{r_e^2}\right) - 30.5\left(\log(St'') + 0.3)\right)^2 + 126, \quad (2.20)$$

where the Strouhal number is

$$St'' = \frac{fl}{U_{max}}, \quad (2.21)$$

and the flow velocity

$$U_{max} = c_0 M_{max}. \quad (2.22)$$

Here M_{max} is the maximum Mach number of the separated flow near the tip, defined as $M_{max}/M \approx (1 + 0.036\alpha_{TIP})$. α_{TIP} is the equivalent angle of attack at the tip in degrees and l is the spanwise extent of the separation zone in metres.

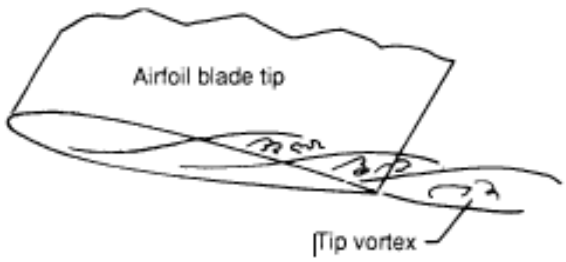

Figure 2.14: Tip vortex formation noise.

- **Trailing Edge Bluntness Vortex Shedding Noise (TEB-VS)** arise from vortex shedding from a blunt trailing edge, with noise characteristics highly depending on the shape and thickness of the trailing edge. Figure 2.15 illustrates the occurrence of TEB-VS noise. If the thickness of the trailing edge is significantly larger than the thickness of the boundary layer at the trailing edge, this noise source will become dominant in the total noise level (Moriarty and Migliore, 2003). The noise is found to be described as:

$$SPL_{TEB-VS} = 10\log\left(\frac{M^{5.5} h L \bar{D}_h}{r_e^2}\right) + G_4\left(\frac{h}{\delta^*_{avg}}, \Psi\right) + G_5\left(\frac{h}{\delta^*_{avg}}, \Psi, \frac{St'''}{St'''_{peak}}\right), \quad (2.23)$$

where the Strouhal definitions are

$$St''' = \frac{fh}{U}, \quad (2.24)$$

$$St'''_{peak} = \begin{cases} \frac{0.212 - 0.0045\Psi}{1 + 0.235(h/\delta^*_{avg})^{-1} - 0.0132(h/\delta^*_{avg})^{-2}}, & (0.2 \leq h/\delta^*_{avg}) \\ 0.1(h/\delta^*_{avg}) + 0.095 - 0.00243\Psi, & (h/\delta^*_{avg} < 0.2) \end{cases}, \quad (2.25)$$

with the average displacement thickness for both sides of the airfoil is given as

$$\delta^*_{avg} = \frac{\delta^*_p + \delta^*_s}{2}, \tag{2.26}$$

where Ψ is the solid angle between both airfoil surfaces upstream from the trailing edge [deg] and G_4 and G_5 are empirical functions.

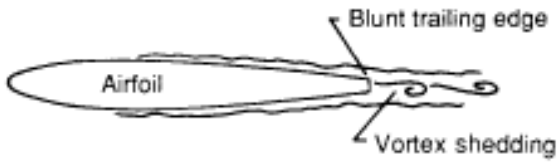

Figure 2.15: Trailing edge bluntness vortex shedding noise.

Turbulent Inflow Noise

Generated by the interaction between atmospheric turbulence and the rotor blade happening due to pressure fluctuations, this noise source depends more on the atmospheric boundary layer and upstream flow conditions than the actual airfoil. The atmospheric boundary layer is defined as the part directly influenced by the earth's surface, with turbulent scales varying from 1 mm to the order of 100 m. This mechanism is a significant source of broadband frequency sound and becomes of importance when the length scale of the turbulent eddies is large compared to the leading edge radius of an airfoil (Moriarty and Migliore, 2003; Vargas, 2008). The empirical expression is found to be:

$$SPL_{Inflow} = SPL^H_{Inflow} + 10\log\left(\frac{K_c}{1+K_c}\right), \tag{2.27}$$

where

$$SPL^H_{Inflow} = 10\log\left[\bar{D}_h \rho^2 c_0^2 L \frac{\Delta l}{r^2} M^3 TI^2 k^3 (1+k^2)^{-7/3}\right] + 58.4, \tag{2.28}$$

and ρ_o is the air density $[kg/m^3]$, c_o is the speed of sound [m/s], l is a turbulence length scale [m], u is the mean wind speed [m/s], TI is the turbulence intensity [%], and K_c is a low frequency correction factor given by:

$$K_c = 10S^2 M \frac{\hat{k}^2}{\beta^2}, \tag{2.29}$$

with S being the compressible Sears function expressed as:

$$S^2 = \left(\frac{2\pi\hat{k}}{\beta^2} + (1+2.4\frac{\hat{k}}{\beta^2})^{-1}\right)^{-1}, \tag{2.30}$$

here $\beta^2 = 1 - M^2$ and $\hat{k} = \frac{\pi f c}{V_{rel}}$ is a local wave number, f is the frequency of interest [Hz], c is the local airfoil chord length [m], and V_{rel} is the local velocity over the airfoil section [m/s].

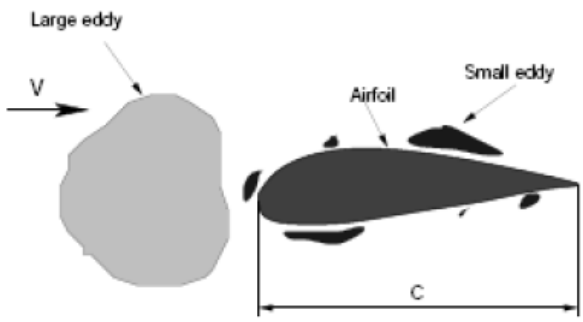

Figure 2.16: Turbulent inflow noise.

2.4 Sound propagation in air

The noise generation mechanisms are now accounted for, however, the knowledge of these noise sources is not sufficient to predict the sound perceived at a given location. As a result of the initial energy in the sound spreading over a continuously larger area, the sound pressure level decreases with distance from the source. If we assume a spherical propagation with no atmospheric effects, the sound pressure level is reduced by 6 dB per doubling of distance (Rogers et al., 2002). This decrease in acoustic energy with distance from the source is what we normally describe as geometric spreading. While the sound wave travels through the atmosphere, several factors affect the propagated aeroacoustic sound pressure levels and must be taken into account in the propagation models (parabolic equation method, ray tracing etc.). The most significant factors are source characteristics, distance, refraction, atmospheric absorption and turbulent scattering, which will be further introduced in the following sections.

2.4.1 Directivity

The directivity of sound is a phenomenon where the sound level emitted from a source is reduced depending on the position of the receiver relative to the noise source (Vargas, 2008). If a sound is directional it means that the strength of the sound varies in different directions, while if it is omnidirectional the energy from the source is radiated equally in all directions.

Brooks et al. (1989) illustrates directivity with an example of a stationary observer and a flat plate in motion, see Figure 2.17. The trailing edge of the plate is the sound source, representing an airfoil. θ_e and Φ_e are the directivity angles in this local coordinate system, with r_e being the distance between the source position and the observer position. The functions for sound directivity are given by:

$$\bar{D}_h(\theta_e, \phi_e) \approx \frac{2sin^2(\theta_e/2)sin^2\phi_e}{(1+Mcos\theta_e)[1+(M-M_c)cos\theta_e]^2}, \tag{2.31}$$

where $M_c \approx 0.8M$. This formula is valid for all high-frequency self-noise sources previously discussed, with the exception of the stall airfoil noise that can be given with an

alternative function for low-frequency noise:

$$\bar{D}_l(\theta_e, \phi_e) \approx \frac{sin^2(\theta_e/2)sin^2\phi_e}{(1+Mcos\theta_e)^4}. \tag{2.32}$$

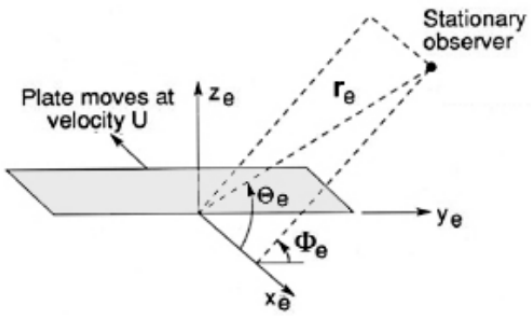

Figure 2.17: Directivity example with angles used. Figure from Vargas (2008).

2.4.2 Atmospheric factors

Air absorption

Atmospheric absorption is the dissipation of energy from an acoustic source when the sound pressure waves travels through the air. The energy converts to heat through several molecular processes, such as viscous interactions, thermal conductivity and molecular relaxation (Hubbard and Shepherd, 1988). The amount of atmospheric absorption depends on the absolute temperature, relative humidity and atmospheric pressure, but is influenced the most by the sound frequency. Figure 2.18 shows how the atmospheric absorption rate, α in dB/km varies with increasing frequency for different relative humidities at a temperature of 20 °C and a pressure of 1 atm. For low frequencies, the absorption is considered low, but at large distances and for high frequencies the atmospheric absorption can give a substantial reduction in sound pressure levels (Fritzell, 2019).

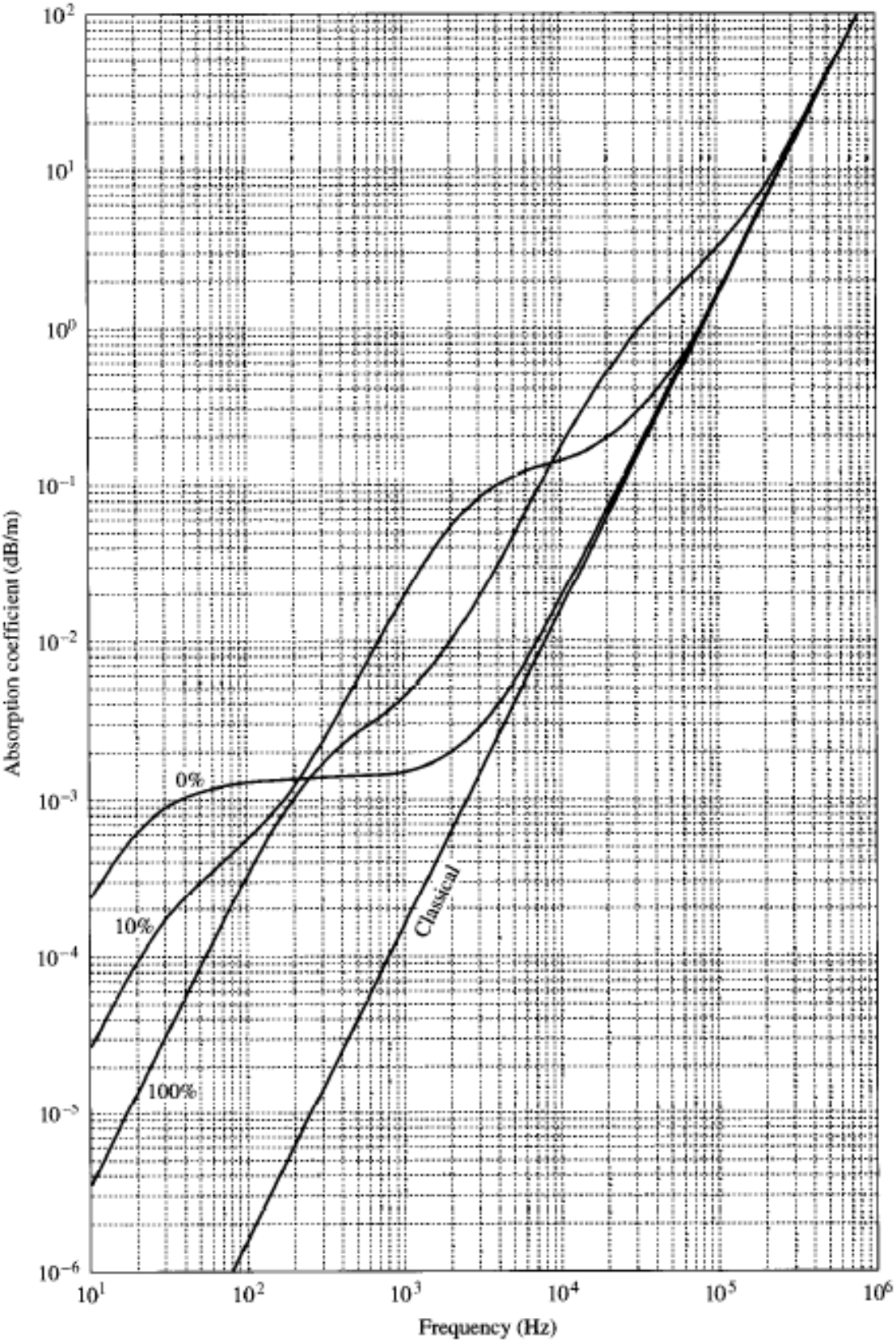

Figure 2.18: Absorption of sound in the atmosphere at 20°C and 1 atm for various relative humidities. Figure from Kinsler et al. (1999).

Wind speed profile

The wind speed is generally low at the surface due to the roughness of the ground generating friction. It increases thereafter with height to the top of the atmospheric boundary layer at around 200 m. This leads to a speed gradient between the lower and higher levels in the atmosphere, and will successively influence the speed of sound at these levels. The wind profile power law gives the wind speed at a given height, compared to another at a different height:

$$U_z = U_r \left(\frac{z}{z_r} \right)^{\alpha}, \tag{2.33}$$

where U_z is the mean wind speed at a height z above ground, U_r is the mean wind speed at a reference height z_r and α is the power-law exponent that varies depending on the atmospheric stability and surface roughness. In general, we can say that the rougher the surface, the larger the exponent.

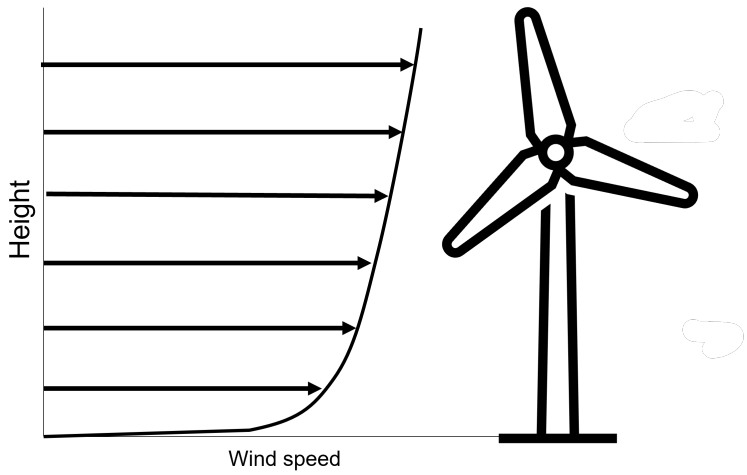

Figure 2.19: Logarithmic wind speed profile with height.

Stability here refers to the state of the atmosphere close to the surface. An unstable atmosphere occur when the air near the ground heats up while the upper air remains cold. Due to warmer air being less dense, it will rise and the cold air gravitates downwards as it is denser, i.e. heavier. This creates a mixing of air that destabilises the airflow. In a stable atmosphere, there will be no vertical motion or mixing and we often get a stronger horizontal wind shear (Tonin, 2012).

Refraction from wind and temperature gradients

Refraction, or bending of the acoustic waves, originates from wind and temperature gradients, causing different densities and therefore also different sound speeds in the layers of the lower atmosphere. Figure 2.20 shows a simple illustration of refraction caused by a vertical wind-shear gradient around an elevated point source.

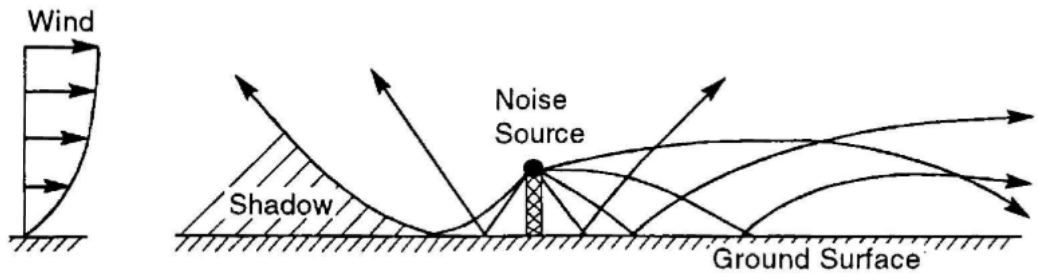

Figure 2.20: Wind-induced refraction on acoustic rays radiating from an elevated point source. Figure from Hubbard and Shepherd (1988).

The speed of sound in air is approximately 340 m/s. The sound travels with the wind direction and gain speed from the wind. When the wind speed increases with height, the upper sound rays will travel faster than the sound rays at the ground. This causes the rays to eventually bend towards the ground, enhancing the sound for a receiver at a downwind position. In the other case, when the sound is going against the wind direction, the speed of the sound will be reduced. Now the upper rays have a lower speed than the rays underneath, bending the sound wave upwards into the atmosphere. This often leads to the formation of shadow zones, where no sound rays enter (Tonin, 2012).

Vertical temperature gradients also affect the stability of the atmosphere, and therefore the speed of sound. Sound travels faster in warm air, which will create the same refraction mechanisms as with wind gradients. When discussing sound propagation from wind turbines, the effects from wind gradients usually dominate over those from temperature gradients (Tonin, 2012).

2.4.3 Terrain effects

Terrain effects include phenomena like reflection, diffraction and ground absorption (Hubbard and Shepherd, 1988). The topography of the landscape will affect how the wave propagates and spreads. Trees, hills, buildings and rivers are some examples of topography that can act as either an amplifier or a reducer for the sound level.

Interaction with the ground surface will affect the sound propagation. One key parameter in evaluating sound propagation over the ground is the impedance of the surface. The Editors of Encyclopedia (2017) define acoustic impedance as the absorption of sound in a fluid or at a surface, given as the ratio between sound pressure at the surface boundary and the sound flux (sound velocity times area).

Chapter 3

Measurements and data

3.1 Noise measurements from wind turbines

As mentioned in previous sections, low-frequency noise emissions from wind turbines can give rise to negative health effects for both humans and animals nearby. Wind turbines and farms in operation need to follow local or national rules for acceptable noise power levels. Conducting accurate noise measurements is, therefore, a vital part of the planning process. There are currently no common international standards or regulations for sound pressure levels from wind turbines. Every country defines its own noise limits and regulation for human exposure (Pantazopoulou, 2010). In Norway, the recommended upper noise limit is L_{den} = 45 dB in areas with noise-sensitive properties, like homes, schools, cabins, kindergartens etc. The term L_{den} (d=day, e=evening, n= night) is an A-weighted equivalent sound level over a 24 hour period. For evening hours between 19:00 to 23:00, a penalty of 5 dB is added, while for nighttime hours from 23:00 to 07:00 the penalty increases to 10 dB (European Environment Agency, 2001). A penalty here means that the noise limit is lowered. Even though this noise indicator is recommended by both the World Health Organisation (WHO) and the European Union (EU), most countries still use the Equivalent Continuous Sound Pressure Level, or L_{Aeq}, to measure the constant noise level with an A-weighting (NVE, 2022a).

3.1.1 In Situ

When conducting noise measurements from wind turbines in situ it should be done according to the internationally recognised standard 61400-11 from the International Electrotechnical Commission (IEC), "Wind turbines - Part 11: Acoustic noise measurement techniques". This standard provides a uniform methodology describing the measurement procedures that enable noise emissions of a wind turbine to be characterised (DNV, 2012). Its purpose is to ensure consistency and accuracy in the measurements and analysis of acoustical emissions from wind turbines (Department of Energy, 2018). The method measures the sound levels from the turbine at a downwind position and calculates the sound power level corresponding to the wind speed 10 m above the ground. The measurements of the sound pressure level and the wind speeds are conducted simultaneously over a short period of time and for a wide range of wind speeds. The standardised procedure makes the measurements of sound power levels

from wind turbines under different environmental conditions comparable to one another under reference conditions. For terrain, the reference condition is a roughness length of 50 mm, typical for an open landscape, and for the wind speed height, it is the standard anemometer height of 10 m (Tonin, 2012).

3.1.2 Scaled wind turbine in a wind tunnel

The study of noise generated from wind turbines can be difficult to do on-site, due to constantly varying meteorological conditions, which makes it hard to replicate the experiment later on. Running the measurements in a wind tunnel on a scaled wind turbine offers a more controlled environment for the localisation and quantification of aeroacoustic noises. An example of a wind tunnel with a scaled wind turbine can be seen in Figure 3.1.

When scaling a wind turbine, one would like to achieve an exact similarity in the kinematic and dynamic flow between the model and the reference turbine (Martin, 2009). Kinematic similarity implies geometrically similar flow streamlines, which can be obtained by matching the tip speed ratio (TSR), given by:

$$TSR = \frac{\omega R}{u}, \tag{3.1}$$

with ω being the rotational speed of the rotor [rad/s], R is the rotor radius [m] and u is the wind speed at the hub height [m/s].

By matching the ratio of the forces acting on the scaled model and the full-scale airfoils, dynamic similarity can be achieved. This requires matching the chord-based Mach and Reynolds numbers (Martin, 2009).

3.2 Data used in this thesis

In this section, the different data used in this thesis will be introduced and explained in detail.

3.2.1 Experimental dataset from Stuttgart

The observational measurements used in parts of this thesis were conducted at the Institute of Aerodynamics and Gas Dynamics of the University of Stuttgart in Germany (Ocker et al., 2021). Their gust wind tunnel is of the Eiffel-type with an open flow and no re-circulation (Würz, 2022). The cross-section of the gust wind tunnel is shown in Figure 3.1. An overview of the technical details for the testing site can be found in Table 3.1.

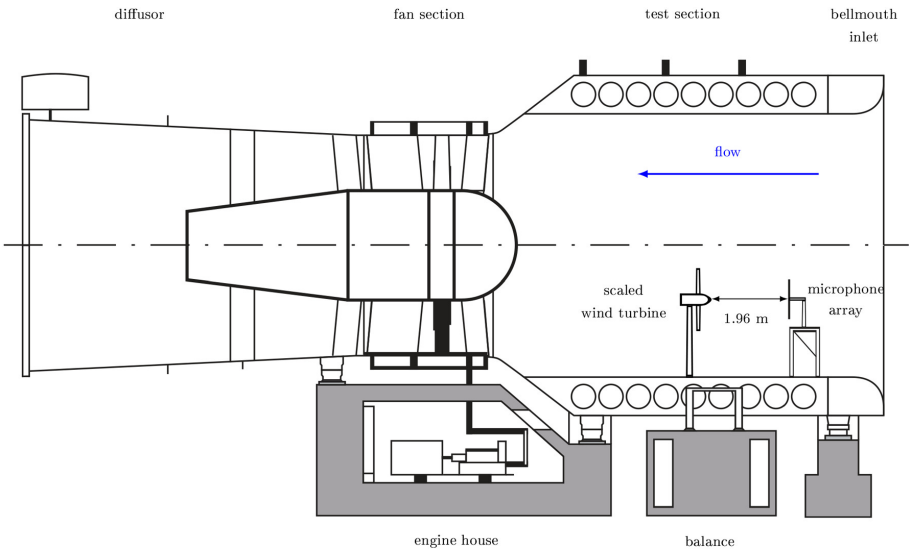

Figure 3.1: Cross-section of the test site, including the wind tunnel, wind turbine and microphone array. Figure from Ocker et al. (2021).

Table 3.1: Technical details of the wind tunnel test site.

Technical details	**Specifications**
Size of test section	Diameter = 6.3 m, length = 6.5 m
Maximum wind velocity	17 m/s
Cross-section of test section	31 m^2
Total length	21.9 m
Fan	8 blades, diameter = 5.6 m
Motor	Electrical power = 315 kW. Hydraulic motor in the hub.

A scaled wind turbine with a hub height of 1.80 m was installed in the gust wind tunnel. The three blades on the turbine had a geometry based on a NACA 4412 airfoil. The dimensions of this blade are shown in Figure 3.2. The span width of the airfoil measures 55 cm and the chord length of the blade is 11.5 cm in the hub region. The total diameter of the wind turbine is 150 cm. The vortex generator (39 cm long) located on both sides of the blade along the span of the airfoil, is shaped like a thin zig-zag strip. This vortex generator delays the flow separation on the blade, which increases the lift and hence also the energy production of the turbine (Froese, 2017).

Most modern airfoils, including the NACA 44 series, are whats called laminar airfoils. These airfoils are shaped so that the flow boundary layer remains laminar along a long section of the chord length, giving them a very low drag over a range of angles of attack, and therefore better lift (Hau, 2006).

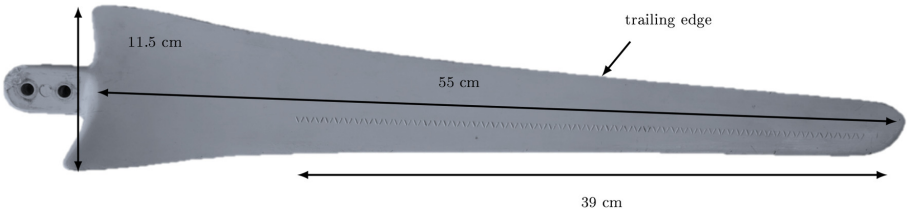

Figure 3.2: Dimensions of the NACA 4412 shaped blade used for the measurements. Figure from Ocker et al. (2021)

Acoustic measurements of the rotating wind turbine were conducted with 48 microphones on a ring array with a diameter $D_{array} = 1.0$ m, see Figure 3.3 for illustration. The array was placed at a distance of 1.96 m in front of the turbine, as shown in Figure 3.1. The data were recorded with a sampling frequency of 48 kHz for a duration of 5 seconds, giving a total of 241 664 measurement points per microphone per wind speed and pitch angle. The relative velocity at the rotor tip varied between 30 and 130 m/s, and was calculated from the formula:

$$v_{rel} = \frac{2\pi N r}{60}, \tag{3.2}$$

where N is the number of rotations per minute [rpm] and $r = 0.75$ m being the turbine radius.

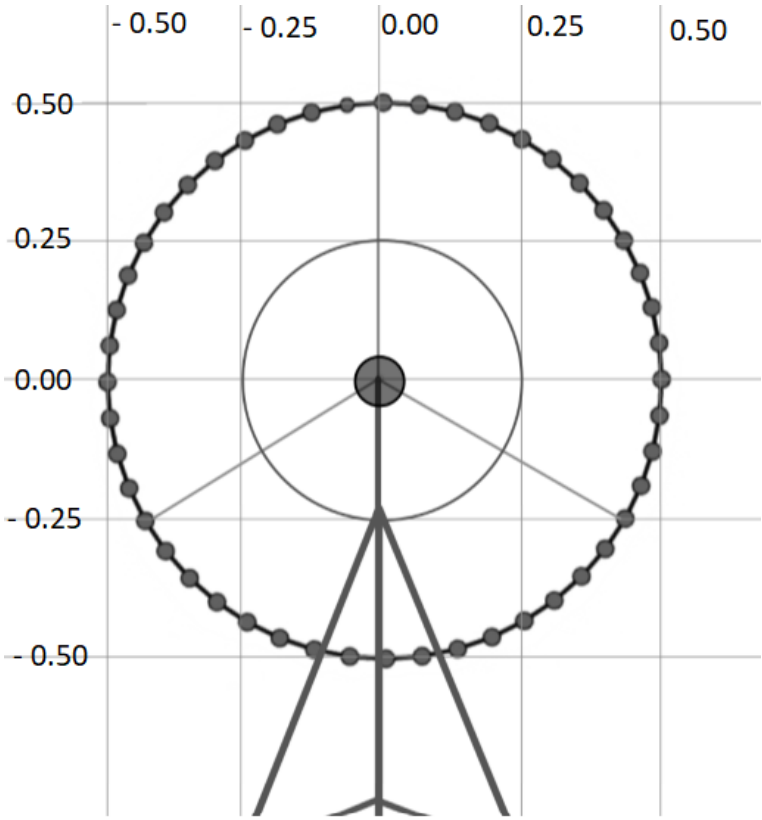

Figure 3.3: Illustration of the microphone array. Dimensions along x- and y-axis in meter.

For further technical information about the measurements and equipment used, see Ocker et al. (2021).

3.2.2 FINO1 data

Data from the FINO1 research platform was used to calculate turbulence intensity with real meteorological variables. FINO stands for *Forschungsplattform in Nord- und Ostsee* (Research platform in the North and Baltic sea), and is financed by the German Federal Ministery for Economic Affairs and Energy. The platform is located north of the German coast and nearby the offshore wind farm Alpha Ventus in the North Sea. The jacket shaped construction is placed at a depth of about 30 m, with a heavily equipped research station and meteorological mast (The FuE-Zentrum FH Kiel GmbH, 2022).

In this study, we have used sonic anemometer data from a height of 80 m in August 2015. This dataset was made available from the OBLEX-F1 research campaign (May 2015 - June 2016), conducted by the University of Bergen and Christian Michelsen Research. The sonic anemometer was operating with a sampling frequency of 15 Hz and provides the three-dimensional wind speed (The Offshore Boundary-Layer Observatory, 2016).

Chapter 4

Methods

In the following chapter, the methods and models used to study the generation and propagation of wind turbine noise are introduced. Then, the application of delay-and-sum beamforming is explained and an example with a random signal is provided. Next, a brief overview of the Amiet model used for the localisation of noise on different airfoils will be given. Lastly, a description of the Parabolic Equation (PE) model used for propagation modelling in an inhomogeneous atmosphere is described together with the software tool we used for its application.

4.1 Signal processing

In real life, all signals are continuous by nature, while computers conduct calculations sample by sample on discrete measurements (Lehto, 2014). When measurements and data of the wind turbine noise have been gathered, these audio signals need to be digitised and processed in a discrete form so that they can be further analysed and displayed. These phases of data application are called signal processing (Hammond and White, 2008). Some mathematical methods that can be applied to a signal are time-series analysis, time-frequency analysis and spectral analysis. In this section, the signal analysis methods used to study the noise from wind turbines are explained.

4.1.1 Spectral analysis

Spectral analysis is used to determine the frequency content of a continuous-time signal in the discrete-time domain (Rao and Swamy, 2018). The main objective of spectral analysis is usually to determine the Power Spectrum Density (PSD) of a random process and by that discover underlying periodicities and energetic tones.

The power spectrum gives the distribution of the signal power over the different frequencies and reveals the existence, or the absence, of repetitive patterns and correlations in a signal (Vaseghi, 2006). To get from time-domain to frequency-domain, a Fourier or wavelet transformation must be executed.

The Fourier transformation is a tool that breaks a signal or a function into an alternate representation, characterised by the sine and cosine functions of varying fre-

quencies (Bevel, 2010). By filtering the signal, it is possible to determine the different spectral components of the time series as a whole.

The Fourier Transform of a function $g(t)$ is defined as:

$$F\{g(t)\} = G(f) = \int_{-\infty}^{\infty} g(t)e^{-2\pi ift}dt, \tag{4.1}$$

where f is the continuous frequency variable, $G(f)$ is the continuous frequency spectrum, t is the time and i is the imaginary number. $G(f)$ can also be interpreted as a measure of the correlation between the signal g(t) and the complex sinusoid $e^{-2\pi ift}$. To get back to the original signal, the inverse Fourier transform equation is given as:

$$g(t) = \int_{-\infty}^{\infty} G(f)\mathrm{e}^{2\pi ift}\,\mathrm{d}f. \tag{4.2}$$

4.1.2 Time-frequency analysis

A problem with the Fourier transform is that it can't locate where in time the different frequency components occur. It can therefore be beneficial to use a short-time Fourier transform (STFT) instead. With the STFT the signal can be represented in both the time and frequency domain and is, therefore, a better fit for non-stationary signals (Ding, 2017). The STFT is expressed as:

$$\begin{aligned} STFT(\tau, f) &= \int_{-\infty}^{\infty} g(t)w(\tau - t)e^{-2\pi fit}dt \\ &= \int_{-\infty}^{\infty} G(\alpha + f)W(\alpha)e^{i2\pi\alpha}d\alpha, \end{aligned} \tag{4.3}$$

where $G(f)$ is the Fourier transform of the signal $g(t)$, and $W(f)$ is the Fourier transform of a symmetric sliding window, $w(t)$. There is a variety of windows to choose from depending on the type of signal. Some familiar windows are the rectangular, Hamming, Hanning, and Bartlett. In the code used for this thesis, the Kaiser-Bessel window is used as it seems to balance out the conflicting goals in the filtering of amplitude accuracy, side lobe distance and height (National Instruments, 2020).

Spectrogram

A non-stationary signal is a signal whose frequency content changes with time. The spectrogram is a tool that is used to illustrate how the frequency spectrum of non-stationary signals varies over a period of time. It is usually set up with one axis representing time and another for frequency while illustrating the strength or "loudness" of a particular frequency at a certain time with a colour chart (Kamp, 2020).

A spectrogram is generated by dividing a time-domain signal into shorter segments of equal length. The segments are of such a size that the frequency content of the signal does not change significantly within the segment. The short-time Fourier transform is then applied to each segment and this is used to construct the spectrogram. In this thesis, spectrograms will be used to identify the frequency content of the measured signals and relate them to known acoustic sources at the wind turbine.

4.2 Localization models

4.2.1 Delay-and-sum beamforming

Aeroacoustic beamforming is a signal processing tool with a long history in multiple fields of study. It is often used to achieve insight into the location and strength of different sources from a complex array of sound. One reason for the great success of the technique is its robustness, being able to distinguish sources in environments with higher background noise levels than the original source intensity (Santana, 2017).

One of the most common and user-friendly approaches for beamforming is the Delay-And-Sum (DAS) technique, illustrated in Figure 4.2 (Grythe, 2015; McCowan, 2001). An array of M microphones and a search grid in the plane where the noise source(s), $f(x,t)$, are most likely to be found is defined (Santana, 2017). The sound of each source will travel along various paths, thus will the microphones also capture the signals with different delays and phases. These delays can be calculated from the speed of sound, c, and the distance between the microphones in the array. The DAS beamformer shifts the signal of each microphone, delaying it by τ_n seconds. The delays are selected to maximise the microphone array's sensitivity to sound waves coming from a particular direction (Grythe, 2015). As a result, all the components from the same direction get registered with the same phase, creating constructive interference, while the signal from other directions gets displaced to be out of phase and therefore experiences destructive interference. The signals of all channels are then summed and normalised by the number of microphones to generate the beamformer output map (Lohmann, 2017; Mars et al., 2017).

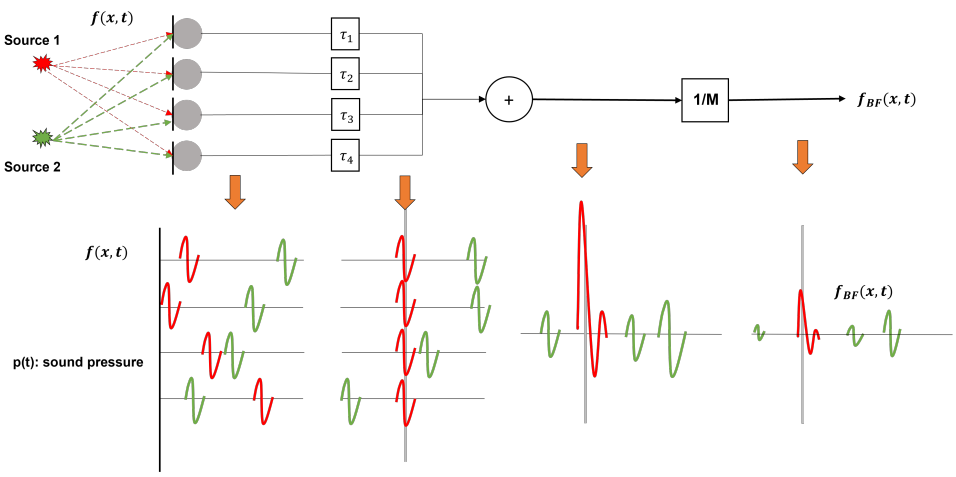

Figure 4.1: Illustration of delay and sum with $f(x,t)$ being the original signal measured by the microphones and $f_{BF}(x,t)$ is the beamformer output. τ is the retarded time delay, M is the number of microphones and w is the shifted signal before being summed together. Figure adapted from Lohmann (2017).

The beamformer output, $L(t,x_0)$, in the time domain can be expressed as:

$$L(t,x_0) = \frac{4\pi}{M}\sum_{m=1}^{M} f(x_0,t+\tau_n)|x-x_0|, \tag{4.4}$$

where f is the measured signal from each microphone, M is the number of microphones, x_0 is the position of the noise source and x is the location of the microphone (Santana, 2017). In addition to a time delay, we have a phase delay associated with each microphone. We obtain the power of the beamformer output in the frequency domain by calculating the output power as a function of these phase delays, called the steered response (Grythe, 2015).

Figure 4.2 shows how delay-and-sum beamforming can be used to localise a point source in a given plane using a microphone array. The demonstration was done by computing a random sound signal, based on the position of the microphones and the arrival angle and amplitude of the source. We conducted the test for two source frequencies of 200 Hz and 500 Hz, to show the difference in spatial resolution. Both the acoustic source maps and the steered response in the UV-space were plotted. In the last tests, Figures 4.2c) and d), a three-dimensional illustration of the main lobe and corresponding side lobe is shown, together with its normalised amplitude gain.

With the simplicity of delay-and-sum, some disadvantages also arise, like poor spatial resolution at lower frequencies and the appearance of spurious sources not coming from the actual signal. Even though this will not be discussed further in this thesis it is known that the issues from DAS beamforming can be improved by iterative deconvolution algorithms like DAMAS and CLEAN-SC (Ma et al., 2020). We will be using a simple one- and two-dimensional delay-and-sum beamformer to study the direction of arrival for wind turbine noise from the experimental setup described in subsection 3.2.1.

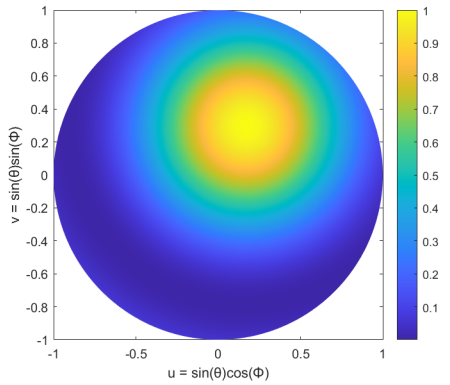

(a) f_{source} *=200 Hz.*

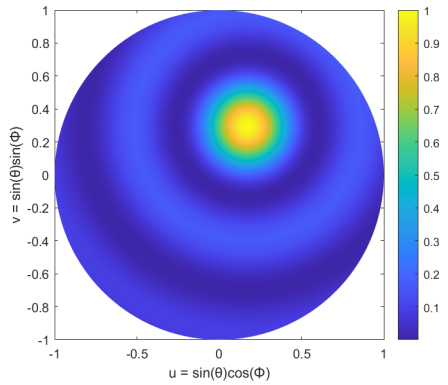

(b) f_{source} *=500 Hz.*

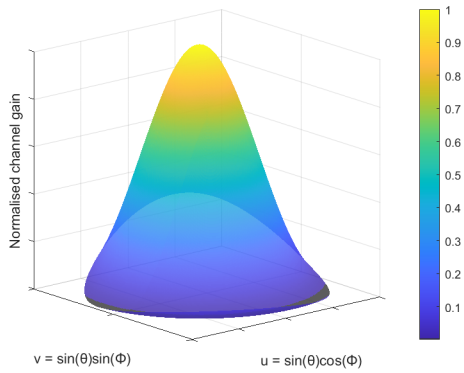

(c) Steered response in UV-space in 3D. f_{source} *=200 Hz.*

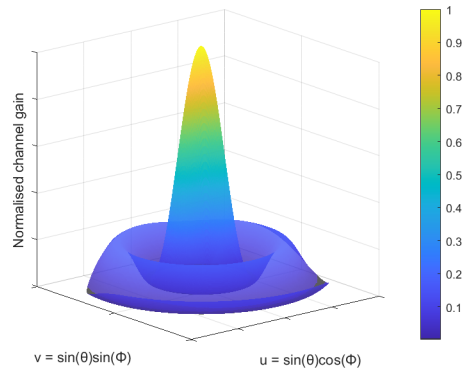

(d) Steered response in UV-space in 3D. f_{source} *=500 Hz.*

Figure 4.2: Example of a two-dimensional delay-and-sum for varying source frequencies and angles of attack, computed from a random sound signal. Subfigures a) and b) shows the acoustic source map for a signal reaching the array with the angles of attack; $\theta = 20\,°$ *,* $\phi = 60\,°$*, for two different source frequencies (200 Hz and 500 Hz).*

4.2.2 Amiet model

Moving on to the aeroacoustic source model proposed by Amiet (1975) for a fixed airfoil. Based on the linearised acoustic theory, by assuming a small disturbance in the acoustic field, the model reduces the airfoil to a flat plate with no thickness and zero angle of attack (Tian and Cotté, 2016; Tian, 2016). An illustration of the model setup is found in Figure 4.3Some key assumptions made to simplify the model are (Tian, 2016):

- the convected turbulence from the mean flow is "frozen", i.e. no changes to the turbulence properties during the convection.
- the turbulence fluctuation is negligible compared to the mean flow velocity.
- the interaction between the airfoil and the turbulent flow is inviscid, i.e. the viscous shear and normal stresses are small in comparison to internal forces, making it possible to reduce the problem to solving linearised Eulers equations.

The model is designed to be used as a benchmark for more advanced analytical airfoil noise models and experimental measurements, but can provide a preliminary

prediction in a much faster and cheaper way than modern numerical simulations. Hirono et al. (2020) defines the problem setup as follows: "A flat airfoil is immersed in a turbulent, subsonic moving medium flowing with Mach number M in the +x direction".

The pressure fluctuating on the airfoil surface can be written as (Tian and Cotté, 2016):

$$p(x,y,0,t) = \rho_0 w_0 U \frac{e^{-i\pi/4}}{\sqrt{\pi\left(\beta^2\bar{\kappa}+bK_x\right)\frac{x}{b}}} e^{i\omega t - ix(K_x - A/b) - iK_y y}, \tag{4.5}$$

with ρ_0 is the air density, $w = w_0 e^{i(\omega t - K_x - K_y)}$ is the incident gust amplitude in the Fourier domain, U is the free stream velocity, $A = -kM/\beta^2$, M is the Mach number, $\beta = 1 - M^2$ is the compressibility factor, k is the acoustic wave number, $K_x = \frac{\omega}{U_x}$ and K_y is the chord-wise and span-wise wave number and b is the half chord. Some non-dimensional parameters are also introduced to make the equation more concise: $\bar{\mu} = \frac{\omega}{U} M/\beta^2$ and $\bar{\kappa}^2 = \bar{\mu}^2 - \bar{K}_y^2/\beta^2$.

Amiet's model for turbulent inflow noise says that if we assume a dipole source, the power spectrum density on far-field acoustic pressure can be obtained from Equation 4.5 as (Amiet, 1975; Tian, 2016):

$$S_{pp}(\mathbf{x},\omega) = \left(\frac{\rho_0 \omega c x_3}{2c_0 S_0^2}\right)^2 U \int_{-\infty}^{\infty} \Phi_{ww}\left(\frac{\omega}{U}, K_y\right) \mathcal{L}^2\left(x_1, \frac{\omega}{U}, K_y\right) \operatorname{sinc}^2\left[\frac{L}{2}\left(\frac{kx_2}{S_0} - K_y\right)\right] dK_y, \tag{4.6}$$

where c_0 is the sound velocity, $\mathbf{x} = (x_1, x_2, x_3)$ is the observer coordinate, $\mathcal{L}$ is the airfoil response function describing the airfoil acoustic directivity over the chordwise angles, $\operatorname{sinc}^2(x) = \frac{\sin^2(x)}{x^2}$, S_0 is a modified distance between the source and observer, and Φ_{ww} is the turbulence energy spectrum (Tian, 2016).

For trailing edge noise, the derivation is similar to that of turbulent inflow noise. The power spectrum density of far-field sound can be expressed as:

$$S_{pp}(\mathbf{x},\omega) = \left(\frac{\omega L x_3}{4\pi c_0 S_0^2}\right)^2 \frac{c}{2\pi} \int_{-\infty}^{\infty} \Phi_{\mathrm{pp}}(\omega) \ell_y(\omega) \mathcal{L}^2\left(\frac{\omega}{U}, K_y\right) \operatorname{sinc}^2\left[\frac{L}{2}\left(\frac{kx_2}{S_0} - K_y\right)\right] dK_y, \tag{4.7}$$

with $\Phi_{\mathrm{pp}}(\omega)$ being the power spectral density of the wall pressure proposed by Rozenberg and Robert (2012) , and $\ell_y(\omega)$ being the span-wise correlation length.

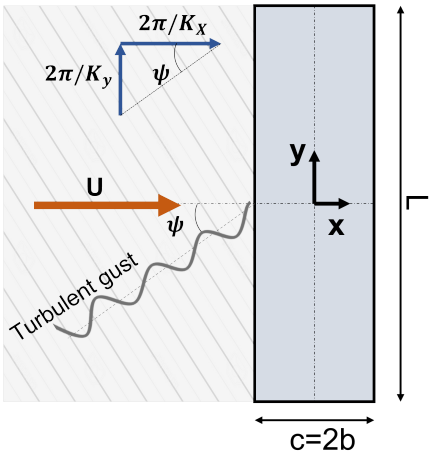

Figure 4.3: Amiet model experimental setup diagram, with gust incidence angle $\psi = arctan((2\pi/K_y)/(2\pi/K_x))$.The oblique gust have a chord-wise wavenumber K_x amd a span-wise wavenumber K_y. Figure adapted from Hirono et al. (2020).

We will be using an open-source implementation of the Amiet analytical model for turbulent inflow noise and trailing edge noise to predict the directivity. We will also perform calculations on the unsteady surface pressure jump and the radiated acoustic pressure on a flat plate airfoil. The airfoil has been defined with the same chord length and airfoil span as the NACA 4412 airfoil used for the scaled wind turbine.

4.3 Propagation model

Noise generated from a source is defined by its noise emission level and can differ from the noise immission level, i.e. the noise received by a microphone, in terms of both magnitude and spectrum properties. These differences occur during the propagation of noise through varying fluids (Tian, 2016). As mentioned in subsection 2.4.2, the propagation of sound in the atmosphere is dependent on many factors (scattering, refraction, reflection etc.) and can therefore be difficult to predict.

The three-dimensional, time-dependent wave equation is generally the theoretical basis for all acoustic propagation models. The exact form of the wave equation can vary depending on what assumptions are made and intended applications. A simplified linear, hyperbolic, second-order, time-dependent, hyperbolic partial differential equation can be used for most applications (Etter, 2012):

$$\nabla^2\Phi = \frac{1}{c^2}\frac{\partial^2\Phi}{\partial t^2}, \tag{4.8}$$

where $\nabla^2 = \left(\partial^2/\partial x^2\right) + \left(\partial^2/\partial y^2\right) + \left(\partial^2/\partial z^2\right)$ is the Laplacian operator, Φ is the potential function, c is the speed of sound and t is time. With further simplifications, the wave equation in Equation 4.8 reduces to the time-independent Helmholtz wave equation:

$$\nabla^2\phi + k^2\phi = 0, \tag{4.9}$$

where ϕ is the time-independent potential function, obtained from a harmonic solution for the potential function $\Phi = \phi e^{-i\omega t}$, $\omega = 2\pi f$ is the source frequency, f is the

acoustic frequency, $k = (\omega/c) = (2\pi/\lambda)$ is the wavenumber and λ is the wavelength (Etter, 2012).

In the following section, we will present the low-frequency parabolic equation for an inhomogeneous atmosphere that is used in this thesis to track and study the propagation of noise in three atmospheric stability conditions.

4.3.1 Parabolic equation method

The Parabolic equation (PE) was deducted from a parabolic approximation of the Helmholtz wave equation (Equation (4.8)), by Leontovich and Fock [1946] in the 1940s and applied to radio wave propagation at the Earth's surface. Since then, it has been used in many fields of computational acoustics, such as quantum mechanics, optics, earthquake wave propagation and underwater acoustics (Yang, 2016). One of the key reasons for this widespread use is that the equation can be solved numerically by the marching method and thus requires less computational effort than it would take for a full elliptic model (Bakhoday Paskyabi and Rashidi, 2005). The PE equation can be used to estimate how atmospheric turbulence and terrain variations will affect sound propagation (Yang, 2016). It is designed for the computation of acoustic transmission loss as a function of range and depth and is useful when propagation is predominantly radial and when backscatter can be neglected (Brock, 1978). The following theory on how to obtain the parabolic equation is based on the work by Tian (2016) in the paper "Modeling of wind turbine noise sources and propagation in the atmosphere".

We start with two dimensional Helmholtz equation, reduced from Equation (4.8) by the assumption of axial symmetry:

$$\left[\frac{\delta^2}{\delta x^2} + \left(\frac{\delta}{\delta z^2} + k^2\right)\right] q_c = 0, \tag{4.10}$$

where $q_c = p_c\sqrt{x}$ gives a link between the quantity q_c and the complex pressure p_c. x and z is along the propagating and vertical direction respectively, and k is as known the wavenumber. By defining an operator G_c as:

$$G_c = \left(\frac{\delta}{\delta z^2} + k^2\right), \tag{4.11}$$

we can rewrite Equation 4.10 as:

$$\left(\frac{\partial}{\partial x} + i\sqrt{G_c}\right)\left(\frac{\partial}{\partial x} - i\sqrt{G_c}\right) q_c = 0. \tag{4.12}$$

Since the Parabolic equation only accounts for the outgoing wave, we can reduce the equation to:

$$\left(\frac{\partial}{\partial x} - i\sqrt{X_c}\right) q_c = 0, \tag{4.13}$$

where

$$\sqrt{G_c} = k_a \sqrt{\frac{1}{k_a^2}\left(\frac{\partial^2}{\partial z^2} + k^2\right) - 1 + 1} = k_a\sqrt{s+1}, \tag{4.14}$$

and

$$s = \frac{1}{k_a^2}\left(\frac{\partial^2}{\partial z^2} + k^2\right) - 1. \tag{4.15}$$

Here k_a is a reference value of k at the ground surface.

Solutions of q_c can be written in the form:

$$q_c(x,z) = \psi(x,z)\exp\left(ik_a x\right), \tag{4.16}$$

where the exponential term represents a plane wave oscillation, varying faster than $\psi(x,z)$, and with the definitions made above, we can rewrite Equation (4.13) as:

$$\frac{\partial \psi}{\partial x} = ik_a(\sqrt{1+s} - 1)\psi. \tag{4.17}$$

By 1st order Taylor expansion we can approximate the square-root as:

$$\sqrt{1+s} \simeq 1 + s/2. \tag{4.18}$$

Substituting Equation (4.18) into Equation (4.17) we get the narrow-angle parabolic equation:

$$\frac{\partial \psi}{\partial x} = \frac{1}{2}ik_a s\psi = \frac{i}{2k_a}\left[\frac{\partial^2}{\partial^2 z} + \left(k^2 - k_a^2\right)\right]\psi. \tag{4.19}$$

Equation (4.19) is as the name indicates only accurate at small elevation angles (up to about 10°). Gilbert and White (1989), worked out a way to make the equation more accurate using a Padé (1,1) approximation,

$$\sqrt{1+s} \simeq \frac{1+\frac{3}{4}s}{1+\frac{1}{4}s}. \tag{4.20}$$

This makes a new wide-angle parabolic equation, valid for elevation angles up to 40°:

$$\left(1 + \frac{1}{4}s\right)\frac{\partial \psi}{\partial x} = \frac{1}{2}ik_a s\psi. \tag{4.21}$$

Application of the parabolic equation model

To perform the analysis of wave propagation over variable terrain and for different atmospheric properties, a MATLAB-based software tool was provided. The robust algorithm automatically provides a field solution for a complete vertical plane given one source frequency (West et al., 1992). For the study of noise propagation using the parabolic equation, we used three idealised wind and temperature profiles describing different atmospheric stabilities. The Obukhov length, L, is a parameter used to scale the height above the ground, z. This provides us with a dimensionless parameter, z/L,

that is used to classify the atmospheric stability and gives the basis for the wind and temperature profiles used. We only consider its sign when relating it to static stability, since its magnitude is not directly related to either the static or dynamic stability (Stull, 1988). A positive sign indicates a stable atmosphere, while a negative sign implies an unstable atmosphere. If $z/L = 0$ the atmosphere is considered statically neutral. In this work the stability cases considered when studying the noise propagation is; unstable ($z/L = -100$), neutral ($z/L = 0$) and stable ($z/L = 200$). The corresponding wind and temperature profiles for each stability condition are plotted in Figure 4.4. To calculate the speed of sound we use the equation:

$$c = c_0\sqrt{T/T_0} + U + U_t, \tag{4.22}$$

where $c_0 = 340$ m/s is the velocity of sound in air, T is a vector of the temperature at all heights [K], $T_0 = 282$ K is the temperature at the surface ($z = 0$), and U and U_t are vectors of the mean wind speed and the turbulent wind speed at all heights [m/s]. The hub height, i.e the height of the source, is 90 m above the surface. Variables used to calculate the idealised wind and temperature profiles are found in Table 4.1.

Air flowing over the surface will exert stress, transferring momentum to the ground and thus decreasing the wind speed. The magnitude of this momentum is expressed by a theoretical parameter called the friction velocity, u^*. The magnitude of the friction velocity increases with the roughness of the surface and is used to calculate how the wind changes with height close to the surface (European Centre for Medium-Range Weather Forecasts, 2019). For this study, a friction velocity of $u^* = 0.05$ m/s is used.

Table 4.1: Variables for the idealised wind and temperature profiles used in the parabolic equation model.

Variable	**Value**
Hub height	90 m
Friction velocity	$u* = 0.05$
Surface temperature	$T_0 = 282K$
Reference speed of sound	$c_0 = 340$m/s
Mean wind speed	U
Turbulent wind speed	U_t

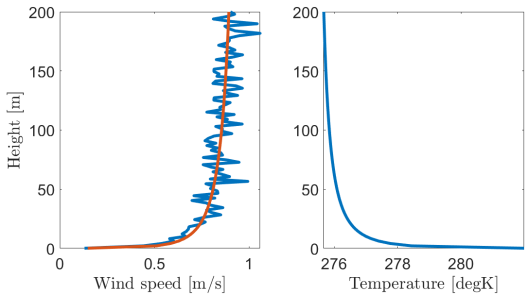

(a) Unstable conditions, Obukhov parameter = -100 m.

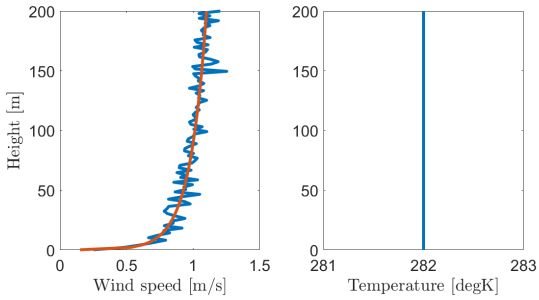

(b) Neutral conditions, Obukhov parameter = 0 m.

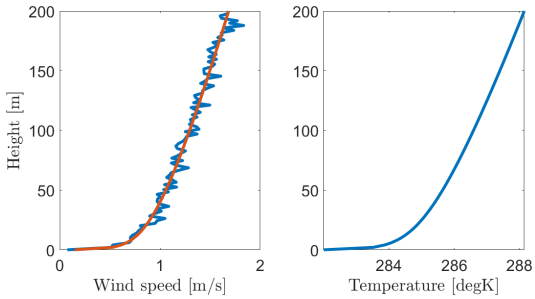

(c) Stable conditions, Obukhov parameter = 200 m.

Figure 4.4: Wind (left) and temperature (right) profile for three different stability conditions.

Chapter 5

Results and discussion

This chapter will present the results of this study on the generation and propagation of aeroacoustic noise arising from wind turbines. We start by visualising the parts of the signal processing from scaled wind turbine data, using statistical methods to describe how wind speed and pitch angles affect the pressure levels before moving on to studying the frequency spectra for each case. An attempt on beamforming using delay-and-sum is applied to the scaled wind turbine data, for both one- and two-dimensions. Results from the Amiet model for noise generation will then be presented using geometry data from the NACA4412 airfoil and real turbulence data from FINO1. Lastly, we perform a sensitivity analysis of a low-frequency PE model for noise propagation with respect to temperature variations and wind speed profiles under three atmospheric stability conditions.

5.1 Noise generation

Observational data from Stuttgart are used in the study of noise generation. Signal processing is conducted with time series and time-frequency analysis tools. This is important to get an understanding of how wind turbines respond to changing wind speeds and pitch angles. In Table 5.1 the averaged pressure signal from the 48 microphones for several variations of wind speeds and pitch angles was used to calculate the mean value, the variance, and the standard deviation, together with the skewness and the kurtosis of the histogram of the signal. Figure 5.1 shows an example of how the noise from the scaled wind turbine varies with time for a wind speed of 5 m/s and a pitch angle of 0 degrees. The pressure oscillated around zero, with a mean of 0.0028 Pa (black line) and a standard deviation of 0.6552 (red lines). Statistical values calculated for all cases can be found in Table 5.1.

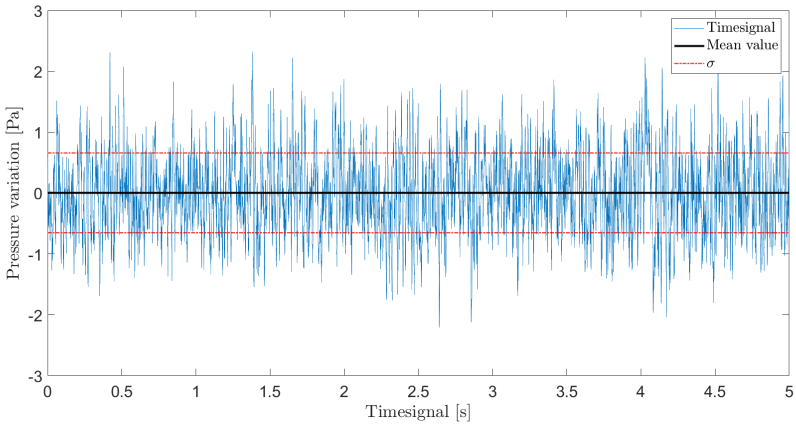

Figure 5.1: Timeseries of sound pressures at a wind speed of 5 m/s and a 0 degree pitch angle in blue, with mean and standard deviation indicated with black and red lines respectively.

5.1.1 Histogram and statistical calculations

With increasing wind speed, the variance of the pressure signal increases rapidly, so does the coherent standard deviation. This is illustrated in Figures 5.2 and 5.3 showing histograms of the pressure distribution for five pitch angles at wind speeds of 5, 7, 11 and 13 m/s. A Gaussian function, also referred to as the normal distribution, was fitted over the histograms to show how the experimental data was distributed, and if any outliers or skewness were apparent. For all cases, the normal distribution fits well, with a minor skewness towards the left side of the mean value, i.e negative pressure levels. This observation is very small and can most likely be ignored due to instrumental or experimental errors.

Changing of pitch is also a large factor in the pressure levels and its variation and standard deviation, as seen from both the histograms and values calculated. If we look at the case for a wind speed of 7 m/s, the pitch angle with the lowest mean sound pressure is 8 degree, corresponding to a mean pressure of -0.0050 Pa. These operating conditions also gives the highest standard deviation with $\sigma = 1.7496$ Pa. Therefore, it would be wise not to operate the wind turbine at large pitch angles for the given wind speed if we are to minimise the noise level. It is necessary to look at the data with more sophisticated analyses next, to be able to provide more information about the noise generation.

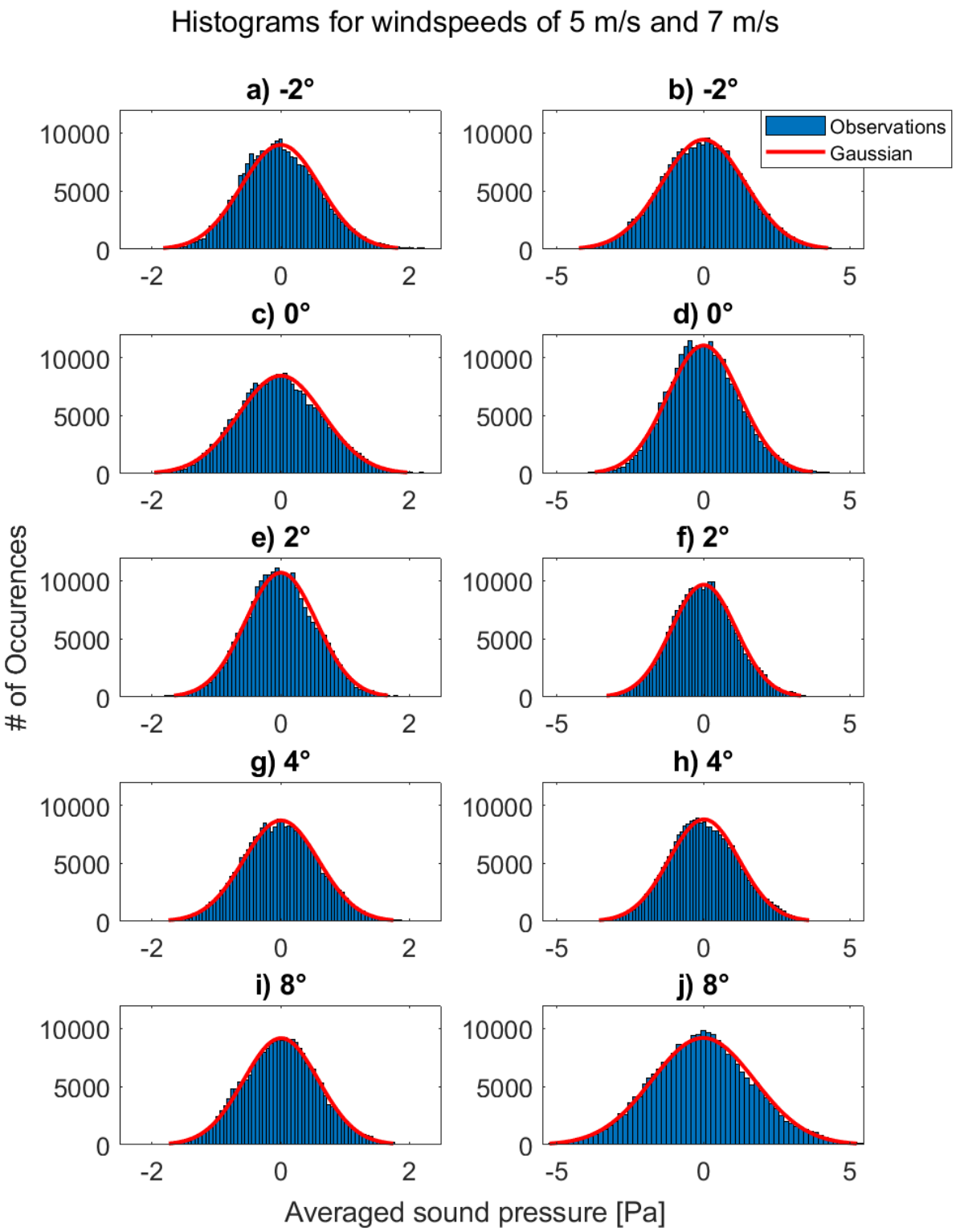

Figure 5.2: Histogram of averaged sound pressures for varying pitch angles with a wind speed of 5 m/s (left column) and 7 m/s (right column). A Gaussian normal distribution (red line) is fitted over the measured pressure values (blue bins).

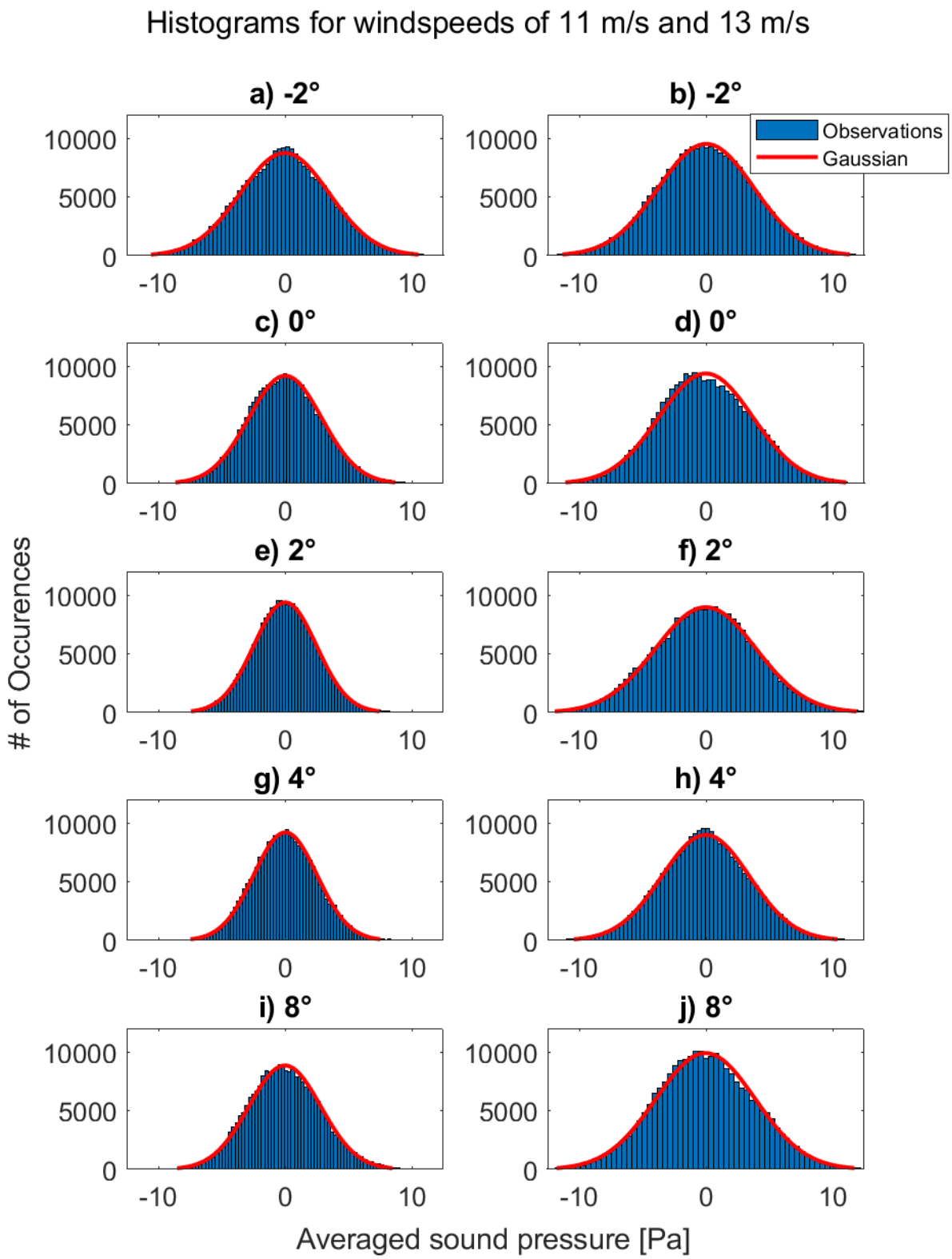

Figure 5.3: Histogram of averaged sound pressures for varying pitch angles with a wind speed of 11 m/s (left column) and 13 m/s (right column). A Gaussian normal distribution (red line) is fitted over the measured pressure values (blue bins).

Table 5.1: The calculated mean value, variation, standard deviation, skewness and kurtosis of the measured sound pressure for all measured time signals.

Wind speed [m/s]	Pitch angle [deg]	Mean sound pressure [Pa]	Variance	Standard deviation	Skewness	Kurtosis
5	-2	0.0013	0.3699	0.6082	0.8383	12.5940
	0	0.0028	0.4293	0.6552	-0.9851	4.7897
	2	0.0046	0.3060	0.5532	-1.9509	10.7994
	4	0.0059	0.3392	0.5824	-1.0112	6.0344
	8	0.0070	0.3375	0.5809	**-2.8377**	**15.1233**
7	-2	0.0064	2.0154	1.4196	-2.3547	11.4315
	0	0.0135	1.5385	1.2404	0.7838	3.8939
	2	0.0146	1.2258	1.1072	1.7483	**17.8379**
	4	0.0246	1.4310	1.1963	2.2359	10.5402
	8	-0.0050	3.0612	1.7496	0.1390	8.1277
9	-2	0.0170	3.1706	1.7806	-0.7930	4.9259
	0	-0.0066	3.2401	1.8000	-0.4521	4.6622
	2	0.0204	3.5469	1.8833	0.0760	6.5985
	4	0.0035	2.8141	1.6775	-1.0135	8.2519
	8	0.0206	3.0040	1.7332	-0.8249	7.7275
11	-2	-0.0270	12.3872	3.5196	-0.7754	4.0145
	0	0.0138	8.3486	2.8894	0.3965	5.4837
	2	0.0084	6.1478	2.4795	0.2438	5.3081
	4	0.0271	6.2364	2.4973	-0.8490	6.5357
	8	-0.170	8.0387	2.8353	-1.3915	10.1690
13	-2	0.0126	14.3037	3.7820	-0.5029	3.1582
	0	-0.0070	13.6555	3.6953	-0.1711	3.4555
	2	-0.0204	15.7548	3.9692	-1.8062	7.5975
	4	-0.0226	12.0276	3.4681	-1.7763	7.4981
	8	-0.0327	15.3460	3.9174	-0.9547	4.0715

5.1.2 Power spectrum

Introduced in chapter 4, the power spectrum for the pressure signals, averaged from the 48 microphones to generate one output, was made with a sampling frequency $f_s =$ 48 kHz. For all wind speeds and pitch angles, as shown in Figure 5.4, there is a clear peak in the output around 4.4 kHz accounting for a transmission loss of about -40 dB. The power amplitude at this frequency does not vary for changing pitch angles but will have a more significant influence on the noise characteristics at low wind speeds due to a generally lower total power level. The noise source at this frequency could therefore be assumed to be independent of aeroacoustic properties, and possibly stem from mechanical parts of the wind turbine or some constant background noise that can contribute to the sound generation, as discussed in section 2.3.

Harmonics from the noise source of interest, i.e. integer multiples of the frequency ($f_1 = 4.4$ kHz, $f_2 = 8.8$ kHz, $f_3 = 13.2$ kHz and $f_4 = 17.6$ kHz), are clearly present for the lowest wind speed of 5 m/s and is most prevalent for higher pitch angles of both 4 and 8 degrees. For higher wind speeds these harmonics generate less power than other noise sources, most likely aeroacoustic ones. They will therefore not appear as singular peaks in the spectra but are nonetheless a contributor to the power level. Studying the five different cases in Figure 5.4, there are fewer abnormalities observed for pitch angles of -2, 0 and 2 degrees, keeping a near-constant power level at higher frequencies. When increasing the pitch, the deviation between wind speeds increases as well, in addition to more variability and peaks in the output appearing at various frequencies. By observing how the power spectrum for a wind speed of 7 m/s changes with the angle of incoming airflow, we see disruption at around 13 kHz at a 2 degree pitch that relocates to frequencies around $7-8$ kHz when operating at an 8 degree pitch. For further analysis, the cases with 5 m/s and 13 m/s will be compared together, as will cases with a 2 degree pitch and 8 degree pitch. These cases were chosen as they represent the extremes in each direction, and will provide a holistic representation of the experimental dataset.

In Figure 5.5, it becomes clear how higher wind speeds affect the sound level at high frequencies. The large spikes taking place at the lower end of the spectrum at 5 m/s are no longer noticeable when operating at 13 m/s. However, for frequencies between 15 and 20 kHz, the power spectrum at 13 m/s is about 40 dB higher than for the measurements at 5 m/s, with stronger instability and power spectrum variability (larger spikes). Stronger winds lead to more vibrations and turbulent interactions with the wind turbine blades, which in turn will produce more noise.

Figure 5.6 demonstrates the airfoils response to changing the pitch angle in more details. For each windspeed in Figure 5.6a) with a 2 degree pitch angle, a similar-looking group of peaks and dips disrupting the power spectrum occur between; $5-10$ kHz for 5 m/s, $10-15$ kHz for 7 m/s and between $15-23$ kHz for 9 and 11 m/s. For 13 m/s there are no clear group of spikes, yet a curved increase in power output in the same frequency range as the two lesser wind speeds is observed. If we compare it to Figure 5.6b), for measurements with a pitch angle of 8 degrees, the group of each windspeed appear to have shifted towards lower frequencies with a more focused main

spike in each group. For measurements at 5 m/s, the group contributes to a sharper and more distinct main spike, with power levels then dropping rapidly at 5 kHz.

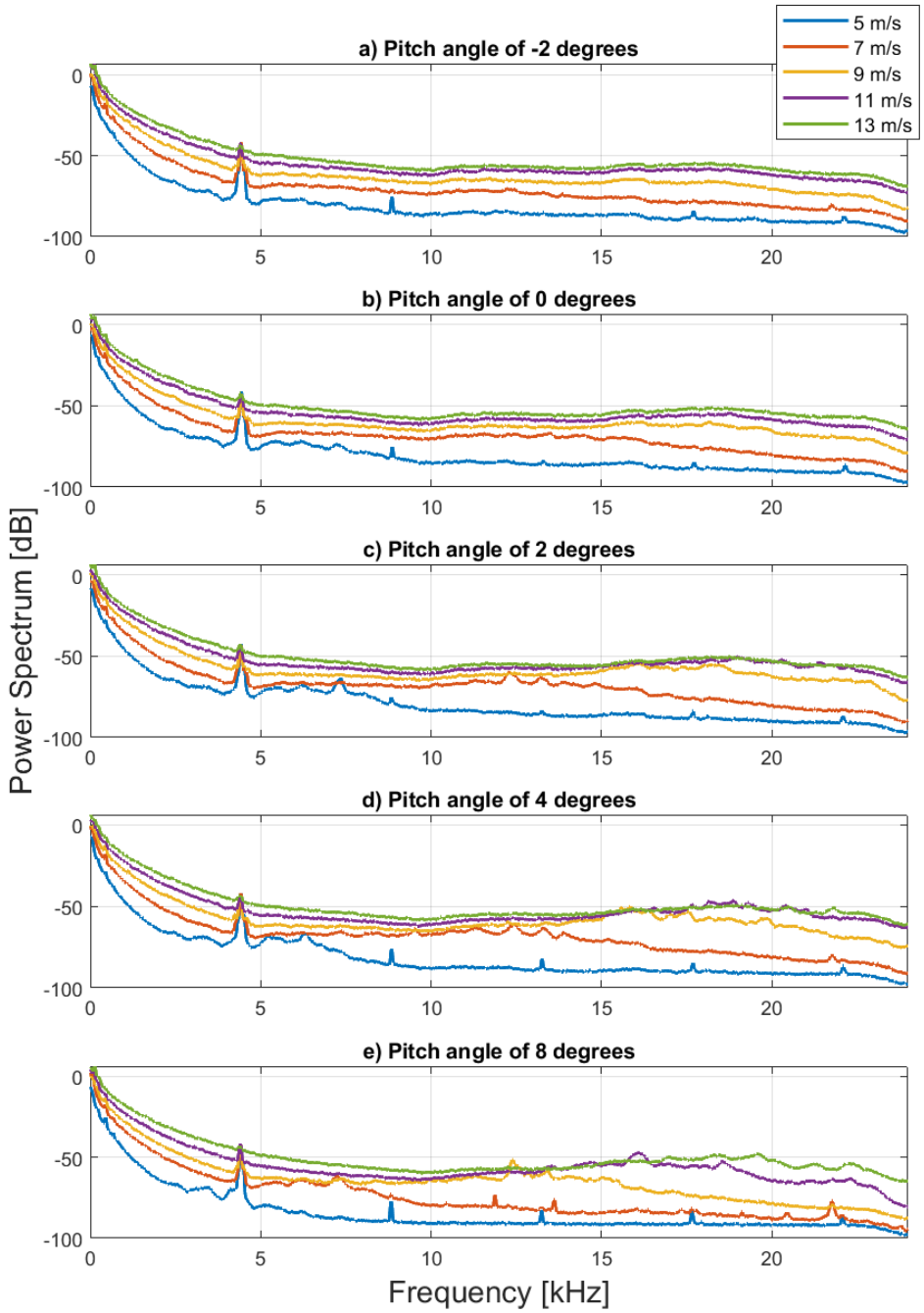

Figure 5.4: The power spectrum for a pitch angle of a) -2 degree b) 0 degree c) 2 degree d) 4 degree and e) 8 degree for wind speeds; 5 m/s (blue), 7 m/s (red), 9 m/s (yellow), 11 m/s (purple) and 13 m/s (green). The frequency along the x-axis is in kHz, while the sound power is given in dB.

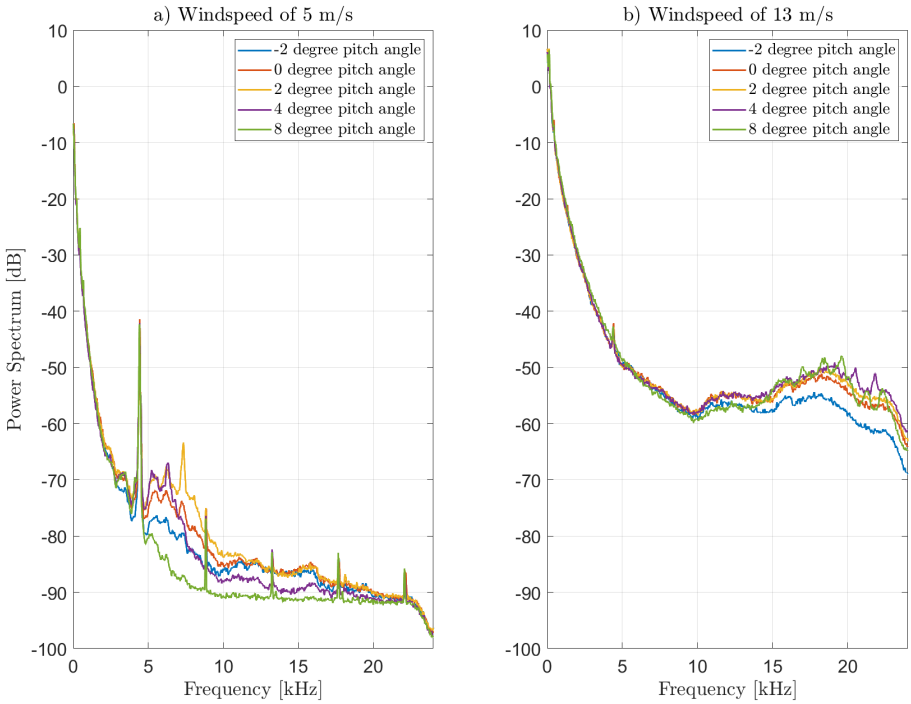

Figure 5.5: The power spectrum for wind speeds of 5 m/s and 13 m/s for varying pitch angles; -2 degree (blue), 0 degree (red), 2 degree (yellow), 4 degree (purple), 8 degree (green).

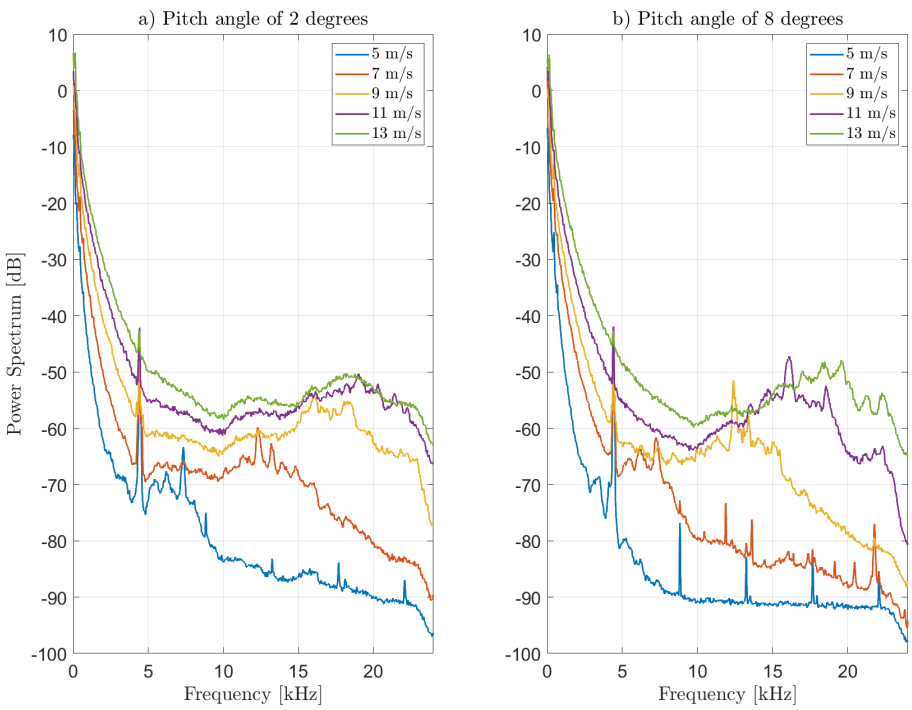

Figure 5.6: The power spectrum for pitch angles of a) 2 degrees and b) 8 degrees for varying wind speeds; 5 m/s (blue), 7 m/s (red), 9 m/s (yellow), 11 m/s (purple), 13 m/s (green).

5.1.3 Sound pressure levels

In this section, we focuse on the comparison of sound pressure levels at different wind velocities and pitch angles. By inspiration from Ocker et al. (2021), the total sound pressure levels are plotted as functions of the relative velocities at the blade tip and the pitch angles in Figure 5.7. The black lines connecting the points correspond to cases with the same wind velocity.

The maximum relative velocity at the blade tip, $v_{rel} = 133$m/s, is obtained at a wind speed of $v_{wind} = 13$m/s and a pitch angle of $\alpha = 2°$. The impact on the relative velocity by changing the pitch increases with higher wind speed, with $\Delta v_{rel} = 28$m/s for $\alpha = 2°$ and $\alpha = 8°$ at a wind speed of 13 m/s compared to $\Delta v_{rel} = 13$ m/s between the same pitch angles at a wind speed of 5 m/s. Looking at the sound pressure level (SPL) for a constant wind speed of 9 m/s, the lowest values occur at a pitch angle of 2 degrees. Under these operating conditions, the SPL corresponds to the same value as for a wind speed of 5 m/s and a 2 degree pitch, with SPL= 58 dB. The highest value of SPL = 71 dB is measured when the wind turbine is operating with pitch angles of 4° and 8° and a wind speed of 13 m/s in the wind tunnel.

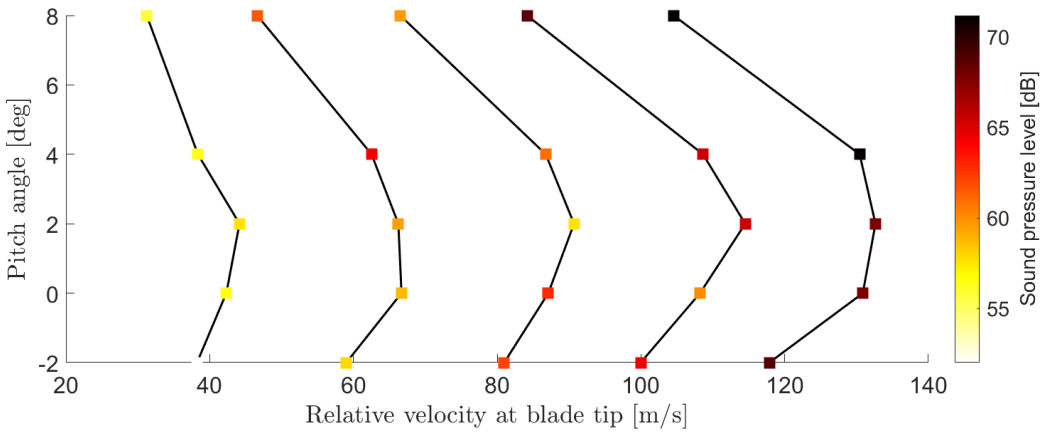

Figure 5.7: Sound pressure level as a function of the pitch angle and the relative velocity at the rotor tip. Operating points with the same wind velocity are connected with the black lines (from left to right: 5, 7, 9, 11 and 13 m/s).

5.1.4 1/3 octave band filter

Noise from wind turbines largely arises from low frequencies (up to about 200 Hz), with its energy content rapidly decreasing for higher frequencies. The power spectrum used earlier was a great way to study how a wide range of frequencies affect the signal, but it does not give a lot of details on smaller scales. It can therefore be beneficial to use a 1/3 octave band filter for the signal and then plot a power spectrum of the noise levels with this new output. We used a reference pressure of $2 \times 10^{-}5$ Pa, i.e the reference sound pressure in air (Kinsler et al., 1999), in the calculations of these spectras.

Figures 5.8 and 5.9 shows the power spectras calculated for wind speeds of 5 m/s and 13 m/s respectively. Each subplot shows the 48 microphone measurements for

the different pitch angles. As expected all cases show a peak in Sound Pressure Level (SPL) in the range between $20-200$ Hz (shaded grey area). We also recognise the spike in sound pressure at approximately 4 kHz for the case of a 5 m/s windspeed in Figure 5.8. The same accounts for the dip in SPL at around 8 kHz for a wind speed of 13 m/s, shown in Figure 5.9.

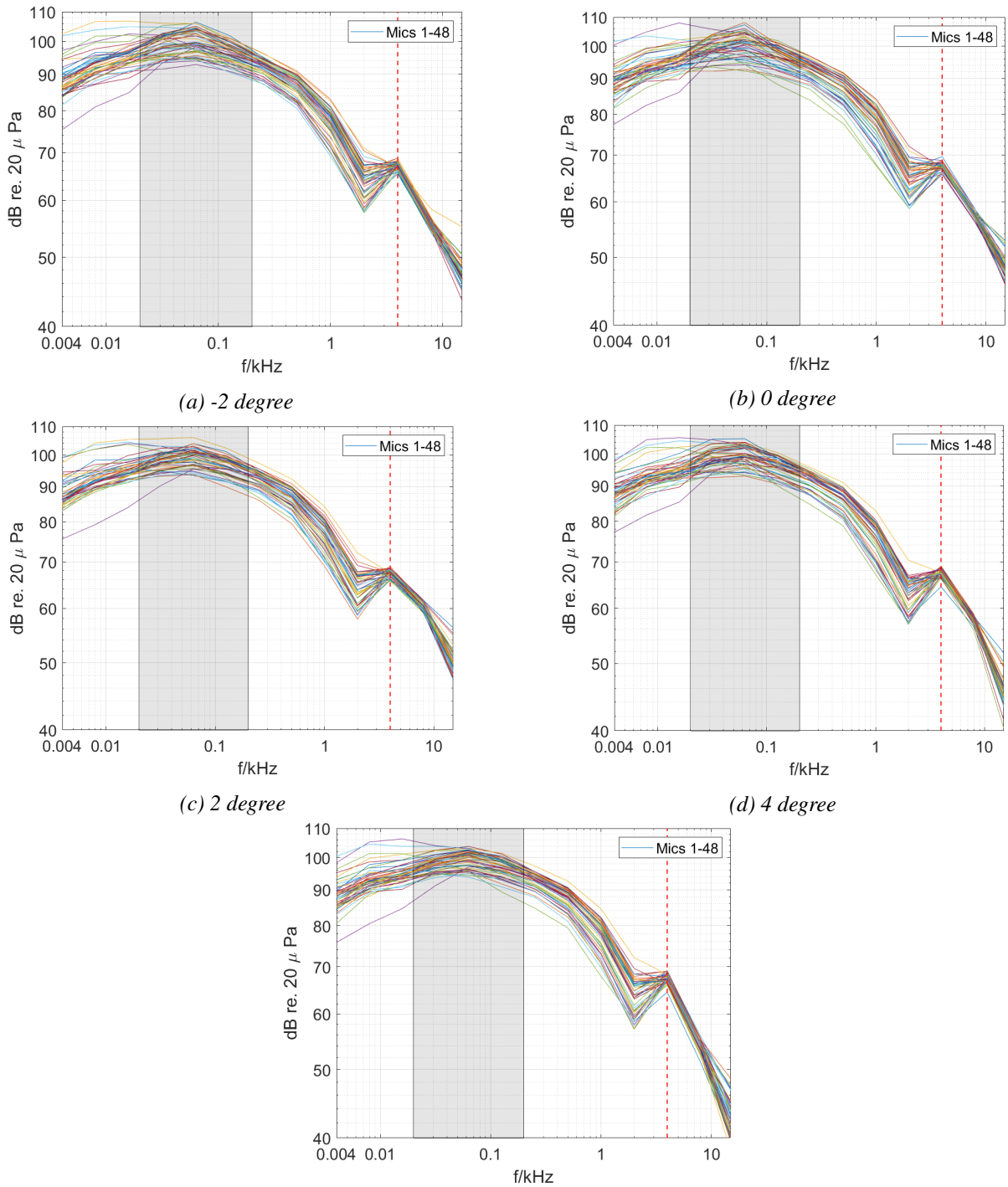

(a) -2 degree

(b) 0 degree

(c) 2 degree

(d) 4 degree

(e) 8 degree

Figure 5.8: Measured noise levels computed with a $1/3$ octave band filter for varying pitch angles at 5 m/s windspeed. The grey filled area indicates the low-frequency range from $20-200$ Hz, and the red dashed line indicates a peak in sound pressure level at a frequency of 3.98 kHz.

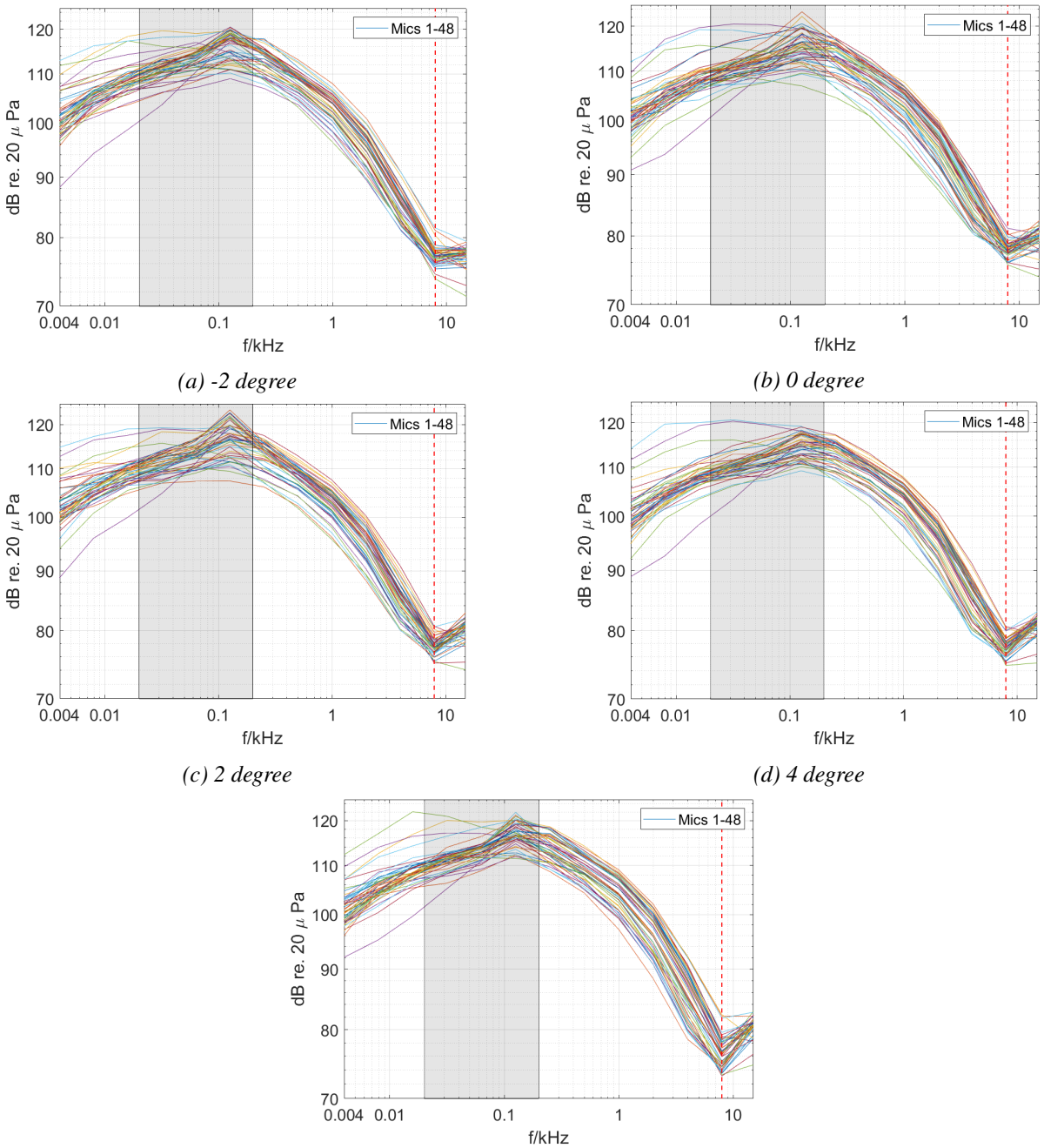

(a) -2 degree

(b) 0 degree

(c) 2 degree

(d) 4 degree

(e) 8 degree

Figure 5.9: Measured noise levels computed with a $1/3$ *octave band for varying pitch angles at 13 m/s windspeed. The grey filled area indicates the low-frequency range from* $20-200$ *Hz, and the red dashed line indicates a dip in sound pressure level at a frequency of* 7.94 *kHz.*

5.1.5 Spectrogram

In this part, we will explore how the power of the spectral density changes over the duration of the measurements, but also illustrate why different spikes previously studied in the power spectras only appear under some operating conditions. As earlier, we will be looking more into cases with wind speeds of 5 m/s and 13 m/s, then for pitch angles of 2 degree and 8 degree. The frequency range (y-axis) was fixed to go from 0 to 10 kHz, as this is where most of the energy content lies. This is still, however, a large

range to be studying and some of the details around 100 Hz will naturally not show.

In Figure 5.10, several horizontal bands of increased amplitude can be identified, with the most dominant band located around frequencies of $4.2 - 4.6$ kHz. This band does not change with changing pitch, neither does it increase with stronger winds. Looking back at Figure 5.4, this can be directly linked with the large spike assumed to be non-aeroacoustic noise. A band can also be seen at around 8.8 kHz for all pitch angles, while other bands are only visible at some of the pitches. No variations with time are evident for any of the horizontal bands of amplitude. Given that the measurements were conducted in a semi-controlled environment, with continuous wind gusts of stable strengths, this will not be directly applicable for full-sized wind turbines, as operating conditions in nature will be more fluctuating and unstable. Comparing the spectrograms in Figures 5.10 and 5.11, the power spectral density has a power output approximately 10 dB higher for stronger winds. Recalling the power spectra in Figure 5.5 for a wind speed of 13 m/s, there were few and short spikes in the plot, giving grounds to why Figure 5.11 shows no good representation of horizontal bands of amplitude.

It can be difficult to determine if the horizontal bands disappear or just hides behind a higher sound level for increasing wind speeds. Figure 5.12 shows the spectrogram of all five different wind speeds at a 2 degree pitch angle. We observe here how the width of the dominant band, as discussed earlier, narrows with an increasing wind speed. Going from being an approximately 400 Hz wide band in the case for 5 m/s, it fades out to a narrow line at 13 m/s.

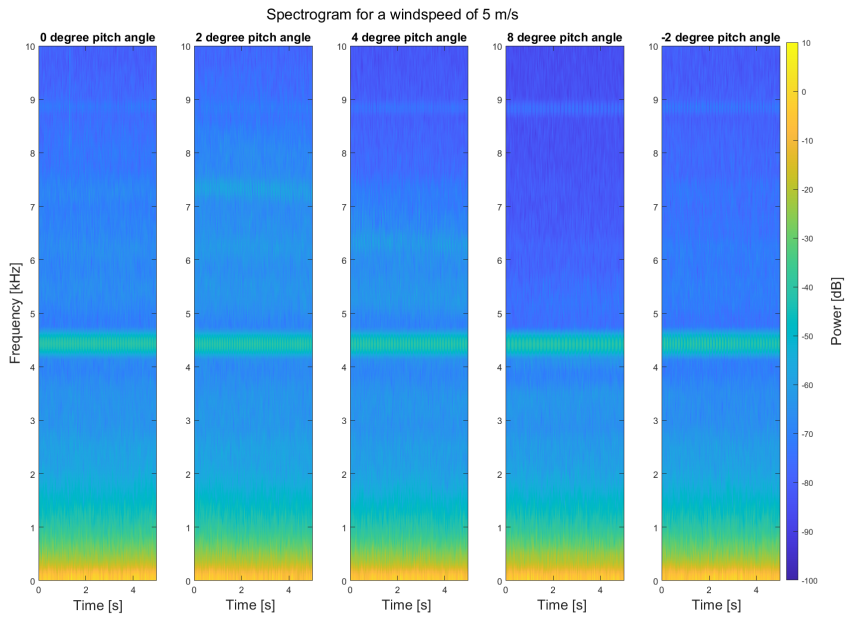

Figure 5.10: Spectrogram for varying pitch angles for a wind speed of 5 m/s. Pitch angles from left to right: 0 degree, 2 degree, 4 degree, 8 degree and -2 degree.

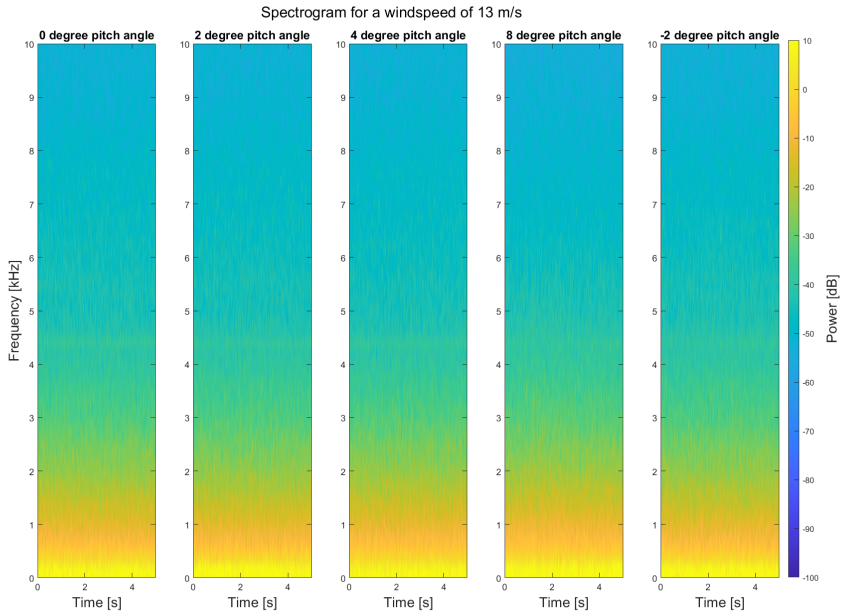

Figure 5.11: Spectrogram for varying pitch angles for a wind speed of 13 m/s. Pitch angles from left to right: 0 degree, 2 degree, 4 degree, 8 degree and -2 degree.

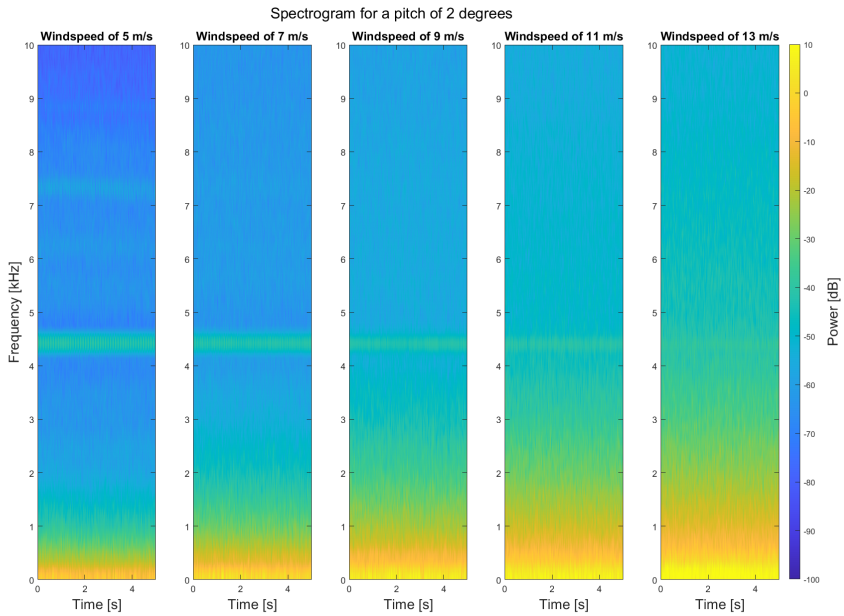

Figure 5.12: Spectrogram for varying wind speeds with a pitch angle of 2 degrees. Windspeeds from left to right: 5 m/s, 7 m/s, 9 m/s, 11 m/s and 13 m/s.

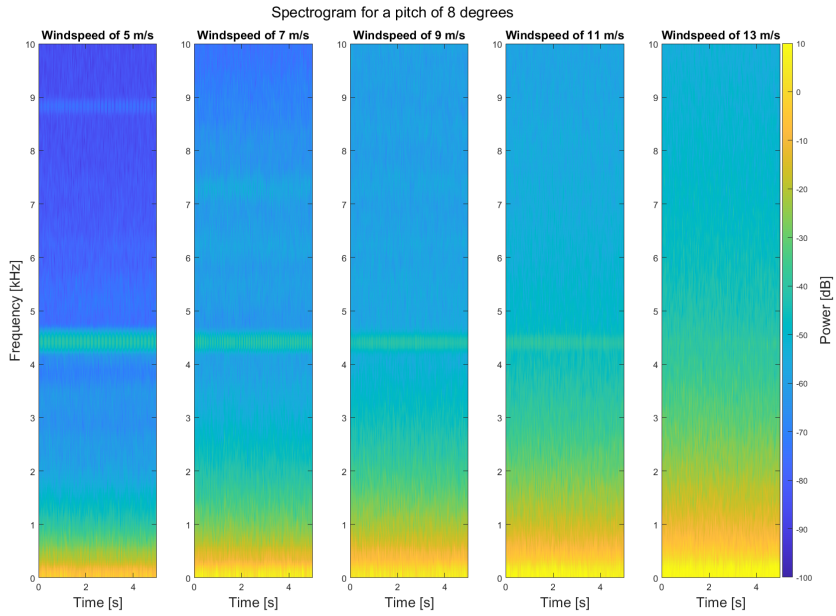

Figure 5.13: Spectrogram for varying wind speeds with a pitch angle of 8 degrees. Windspeeds from left to right: 5 m/s, 7 m/s, 9 m/s, 11 m/s and 13 m/s

5.1.6 Beamforming

Both a one dimensional and two-dimensional beamforming algorithm was used on the observational data from Stuttgart. These algorithms only account for sound sources at fixed locations and are therefore not directly applicable for our setup of a rotating wind turbine. The codes were, however, used to get an understanding of the beamforming method using delay-and-sum and to try to localise the sound source in a given plane. The distance between the scaled wind turbine and the microphone array, together with the distance between each microphone was used to calculate the time of arrival for each signal.

Figure 5.14 shows the directivity using the one-dimensional beamforming technique. The distance between each microphone was calculated to be 6.54 cm. Since the code we were using was originally for a linear microphone array, the test was conducted for three microphones along the ring array. We considered the distance between the three sensors to be small enough to be assumed linear. The figure can tell us how the directivity of the signal changes with increasing wind speed, pitch angle or frequency. It does however not tell us the location of the source. We get an indication of the direction, as the model takes into account one of the two angles of attack (θ or ϕ), however, this is not a sufficient way of localising a source in a two-dimensional plane.

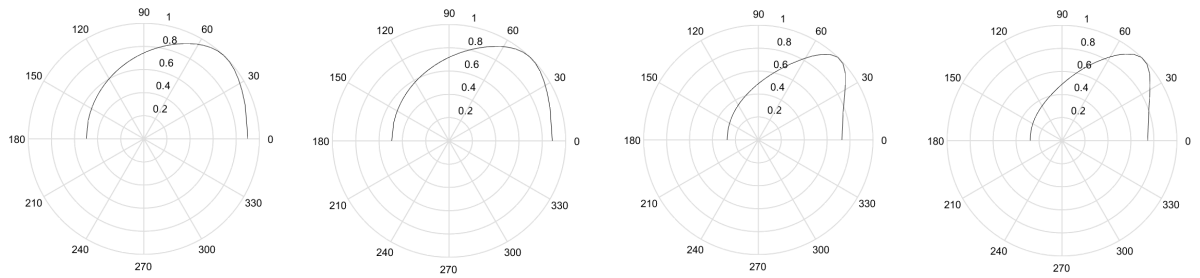

(a) 5 m/s with $\theta = 0$ degree *(b) 5 m/s with $\theta = 8$ degree* *(c) 13 m/s with $\theta = 0$ degree* *(d) 13 m/s with $\theta = 8$ degree*

Figure 5.14: Delay-and-sum beamforming showing directivity for four time signals with varying wind speeds and pitch angles. Source frequency of 1000 Hz.

Figures 5.15 and 5.16 illustrate the two dimensional acoustic source map for the wind turbine operating in windspeeds of 5 and 13 m/s respectively. By increasing the source frequency from 400 Hz to 1000 Hz, the algorithms capacity to localise sources seems to improve, showing several potential sources instead of one large one. This shows why spatial resolution is of the most importance for beamforming technique to be of use. If we consider the blades and rotor on wind turbines, this method would then be used to identify which areas the noise emerged from. Both aeroacoustic noise sources and mechanical noise sources could be recognised and located back to its origin. The colorbar indicates normalised channel gain, having 1 being the expected value at the sources location. Even though the plots show a pattern with some stronger and some weaker areas, the range of the colorbars only vary from between 0.8 to 1. This is strong values, indicating that the source could be located anywhere in the plane. Knowing that the signal used is from a rotating wind turbine, where noise often is generated along the blade airfoil or at the rotor, i.e in the whole plane, it somehow makes sense to get this result. To produce a detailed acoustic source map in the rotor plane, representing the distribution of acoustic source strength on the turbine blades and their subregions, it is necessary to transform the pressure signals at the microphones into a rotating frame of reference.

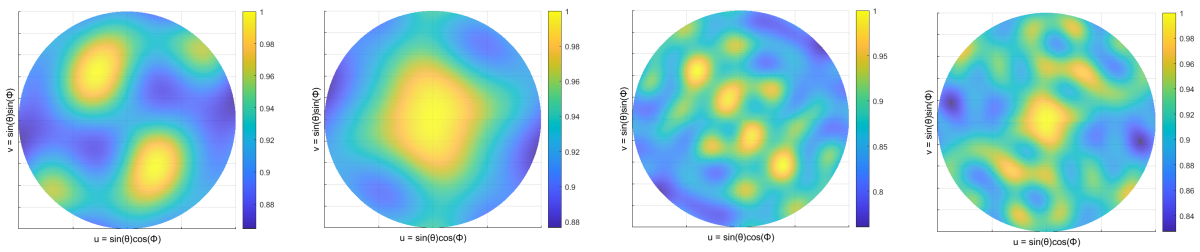

(a) 400 Hz, 5 m/s with $\theta = 0$ degree *(b) 400 Hz, 5 m/s with $\theta = 8$ degree* *(c) 1000 Hz, 5 m/s with $\theta = 0$ degree* *(d) 1000 Hz, 5 m/s with $\theta = 8$ degree*

Figure 5.15: Acoustic source map constructed from delay-and-sum beamforming. Wind speed of 5 m/s with pitch angles of 0 and 8 degree. Colorbar indicates normalised channel gain, where 1 is expected value at source location.

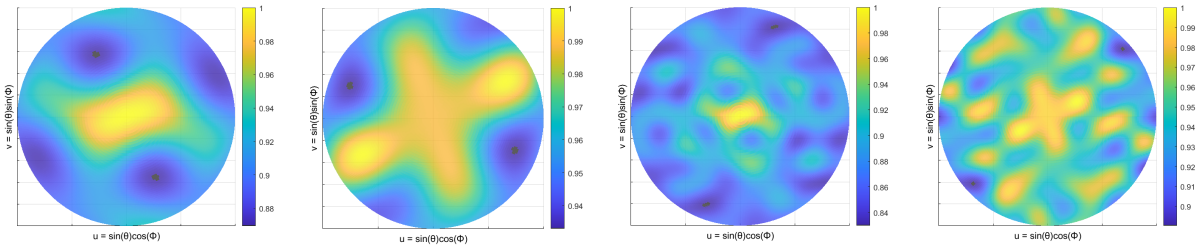

(a) 400 Hz, 13 m/s with $\theta = 0$ degree *(b) 400 Hz, 13 m/s with $\theta = 8$ degree* *(c) 1000 Hz, 13 m/s with $\theta = 0$ degree* *(d) 1000 Hz, 13 m/s with $\theta = 8$ degree*

Figure 5.16: Acoustic source map constructed from delay-and-sum beamforming. Wind speed of 13 m/s with pitch angles of 0 and 8 degrees. Colorbar indicates normalised channel gain, where 1 is expected value at source location.

5.1.7 Amiet model

Values from FINO1 dataset from August 2015 is used to calculate and plot the turbulence intensity vs. mean wind speed at 80 m height, see Figure 5.17. The scattered measurements is fitted against a 5th degree polynomial curve. The mean wind speed and corresponding turbulence intensity, listed in Table 5.2, have been used to describe the turbulent flow properties in the implementation of the Amiet model. Table 5.3 lists the airfoil geometry variables for the NACA4412 airfoil used in the model.

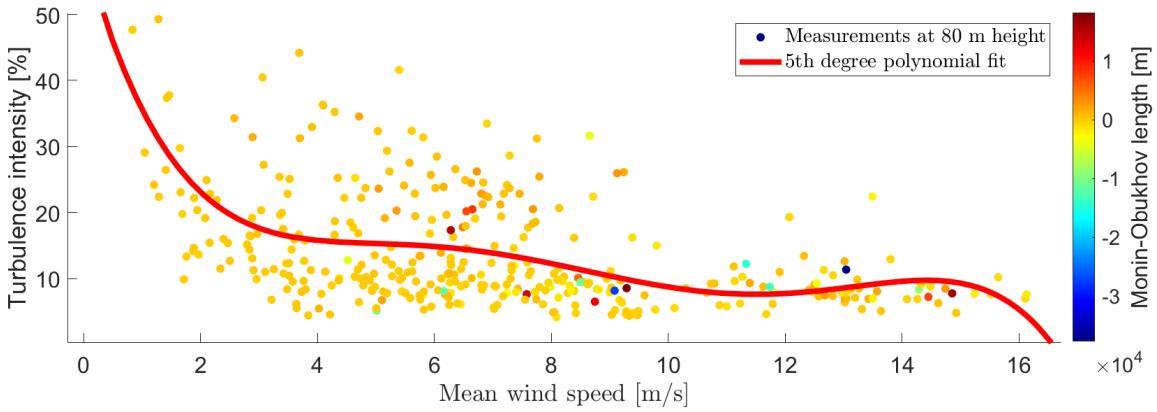

Figure 5.17: Turbulence intensity vs mean wind speed for FINO1 data from August 2015 measured at 80 m height. Colorbar shows values of Monin-Obukhov length, L [10^4m]

Table 5.2: Important values from FINO1 dataset used in further analysis.

Dataset	**FINO1 August 2015**
Mean wind speed (m/s)	7.022
Turbulent intensity for mean wind speed	0.056

Table 5.3: Airfoil geometry for the NACA4412 airfoil on a scaled wind turbine.

Airfoil geometry	**NACA4412**
Airfoil half chord (m)	0.0575
Airfoil half span (m)	0.275
Number of chordwise points	100
Number of spanwise points	101

The response of the airfoil can assume two forms when subjected to a subsonic, oblique gust, i.e. the gust has a velocity lower than the velocity of sound in the medium, depending on the size of the spanwise wavenumber K_y compared to a critical spanwise wavenumber K_y^{crit} expressed as (Graham, 1970; Hirono et al., 2020):

$$K_y^{crit} = \frac{K_x M}{\beta}, \tag{5.1}$$

with K_x being the chordwise wavenumber, M is the Mach number and $\beta = 1 - M^2$. The turbulence is operating at a frequency of about 1.8 kHz.

For $|K_y| < K_y^{crit}$ the gust is labelled as supercritical, meaning that a surface pressure jump is created over a large area along the airfoil chord, while for a subcritical gust when $|K_y| > K_y^{crit}$ the surface pressure jump that is created will decay exponentially over the airfoil (Hirono et al., 2020). This is shown in Figure 5.18, for four different conditions of turbulent gust; supercritical with normal incident ($K_y = 0$), supercritical with oblique incidence ($K_y = 0.35 \cdot K_y^{crit}$), supercritical with oblique incident close to critical ($K_y = 0.75 \cdot K_y^{crit}$) and subcritical ($K_y = 1.25 \cdot K_y^{crit}$). Due to its exponential decay, the subcritical gusts only affects the leading edge surface of the airfoil, and will not affect regions towards the trailing edge.

Under supercritical conditions, the airfoil will act as an efficient radiator of far-field noise. Likewise, the acoustic radiation from adjoining regions will cancel each other out for subcritical gusts, resulting in low radiation of far-field noise (Hirono et al., 2020). The figure also shows how the airfoil responds to normal vs. oblique incidence gusts, with the response wavefronts travelling towards the spanwise direction for oblique gusts instead of following the downstream direction as it does for normal incidence gusts.

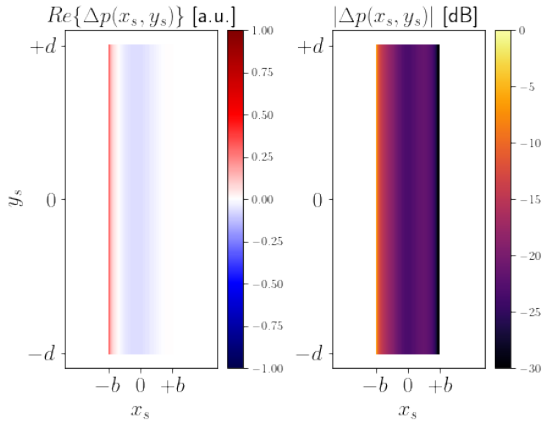

(a) Supercritical gust with normal incidence ($K_y = 0$).

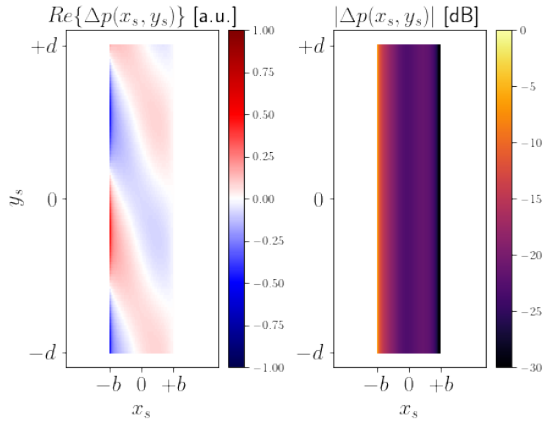

(b) Supercritical gust with oblique incidence ($K_y = 0.35 \cdot K_y^{crit}$).

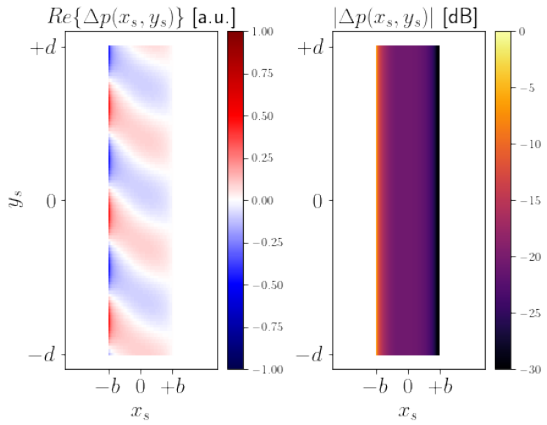

(c) Supercritical gust with oblique incidence close to critical($K_y = 0.75 \cdot K_y^{crit}$).

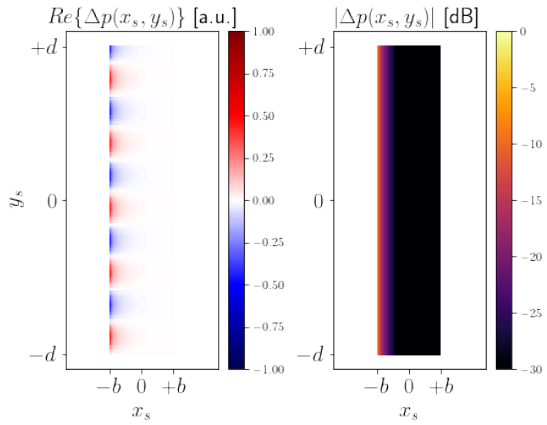

(d) Subcritical gust ($K_y = 1.25 \cdot K_y^{crit}$).

Figure 5.18: Airfoil response for a single gust with $k_0c = 5$ under varying conditions of turbulent gust. Real part of pressure jump (left) and source strength distribution over the airfoil (right).

Figure 5.19 shows the normalised directivity in both the XZ-plane (left) and the YZ-plane (right) for the same four scenarios as above. To describe the airfoil acoustic directivity, we used the effective lift function, $\mathcal{L}$, also called the airfoil response function. A significant difference in directivity strengths is observed between the supercritical and subcritical conditions. For supercritical gusts, the normalised directivity in the YZ-plane shows a high directivity with the value of the main lobe ranging between -15 and -10 dB. When studying the subcritical case in the same plane, the main lobe has a value of -30 dB. This corresponds with the previously discussed surface pressure jump, where supercritical gusts radiates the sound much further than the subcritical.

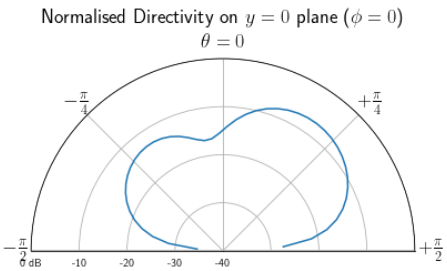

(a) Supercritical gust with normal incidence,y=0 plane

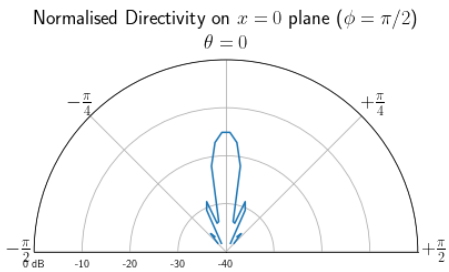

(b) Supercritical gust with normal incidence, x=0 plane

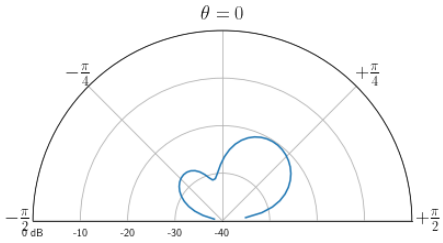

(c) Supercritical gust with oblique incidence, y=0 plane

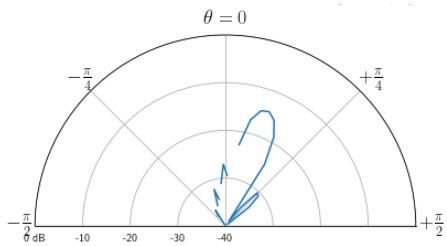

(d) Supercritical gust with oblique incidence, x=0 plane

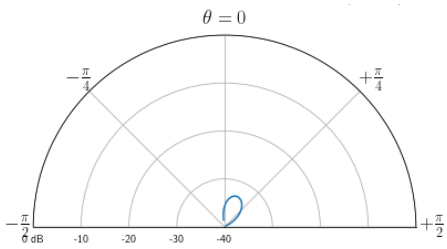

(e) Supercritical gust with oblique incidence / close to critical, y=0 plane

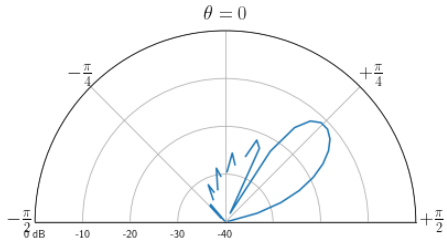

(f) Supercritical gust with oblique incidence / close to critical, x=0 plane

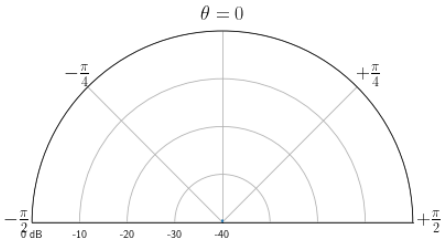

(g) Subcritical gust, y=0 plane

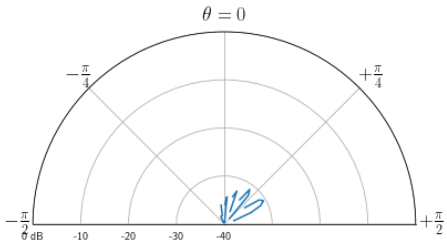

(h) Subcritical gust, x=0 plane

Figure 5.19: Normalised directivity under various conditions. Operating frequency of about 1.8 kHz.

Subcritical gusts have, however, shown to be a significant source of the acoustic radiation for low frequencies, as the cancellation effects along the span is incomplete (Hirono et al., 2020). Figure 5.20 shows the normalised direction for a subcritical gust with a frequency of approximately 450 Hz. When compared with the directivity for a frequency of about 1.8 kHz in Figures 5.19g) and h) the strength of the main lobe has increased with 10 dB in both the XZ- and YZ-plane.

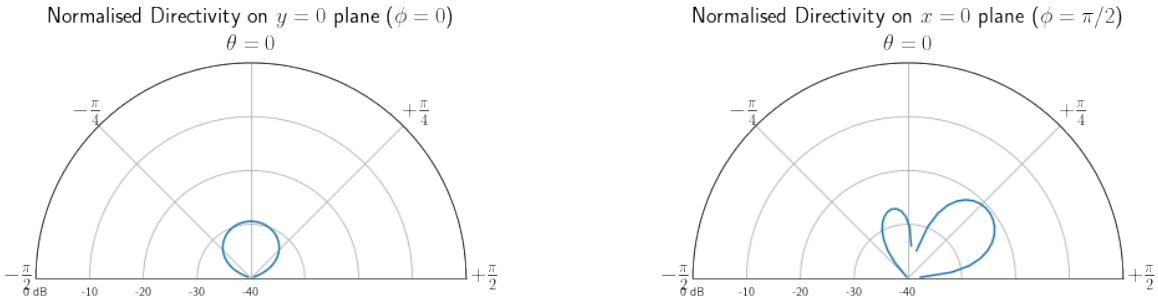

(a) Subcritical gust, y=0 plane

(b) Subcritical gust, x=0 plane

Figure 5.20: Normalised directivity for a subcritical gust ($K_y = 1.25 \cdot K_y^{crit}$) for low frequency, about 450 Hz.

Another interesting fact, that is not shown in these figures, is how with increasing frequency and/or airfoil span, the width of the main lobe will decrease - giving the noise a more sharp directivity. Similarly, the main lobe will broaden its width with low frequencies and/or a shorter span.

Figure 5.21 shows the near-field radiation over the two dimensional cut of the flat airfoil. Due to no solid boundary to support the surface pressure jump at the ends, the amplitude of the acoustic pressure is zero both upstream and downstream from the airfoil (Hirono et al., 2020). Studying the difference in radiation between the cases for supercritical gust with b) normal and d) oblique incidences, we observe how there is no noticeable change in the acoustic field on the y=0 plane. This plane is not affected by the incidence angle at the YZ-plane. There is however a shift towards the left for the acoustic field on the x=0 plane. Here the radiation waves shifts to radiation in an similar oblique direction as the turbulent gust, giving a stronger directivity to the field. By increasing the spanwise wavenumber K_y close to critical (as in e) and f)), the acoustic field increases in strength and radiation angle. These finding correlates with the plots for normalised directivity in Figure 5.19, as well as the surface pressure jumps shown in Figure 5.18.

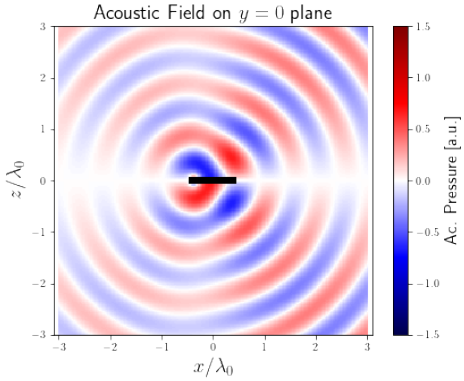

(a) Supercritical gust with normal incidence,y=0 plane

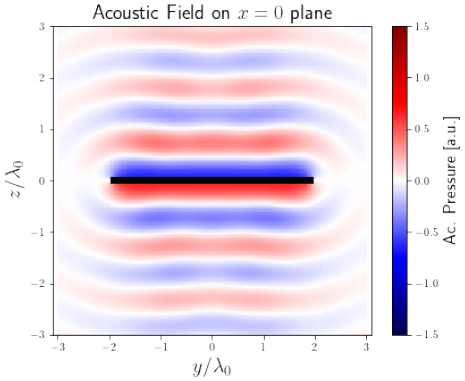

(b) Supercritical gust with normal incidence, x=0 plane

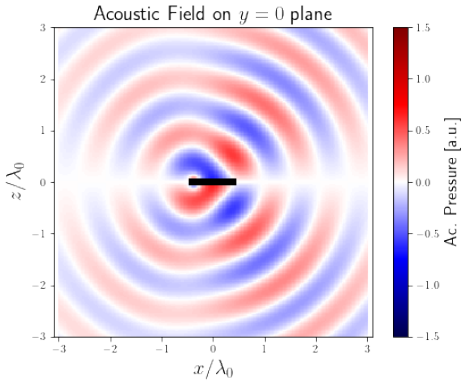

(c) Supercritical gust with oblique incidence, y=0 plane

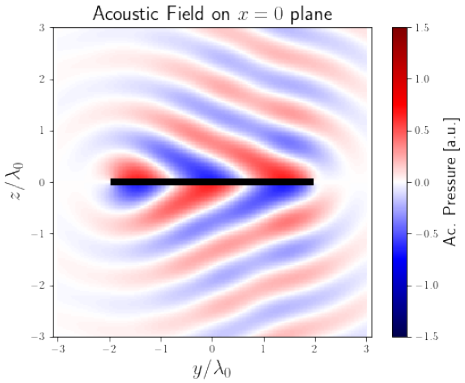

(d) Supercritical gust with oblique incidence, x=0 plane

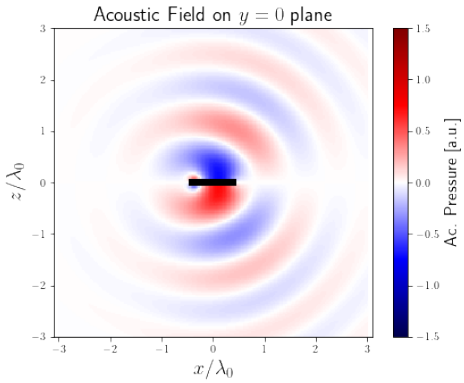

(e) Supercritical gust with oblique incidence / close to critical, y=0 plane

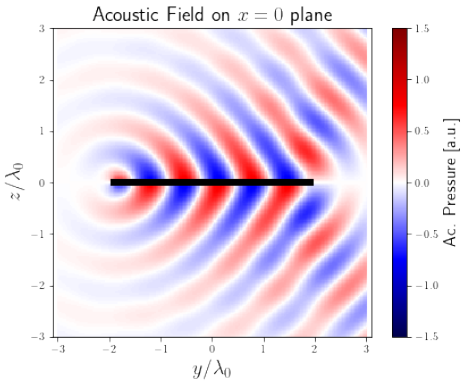

(f) Supercritical gust with oblique incidence / close to critical, x=0 plane

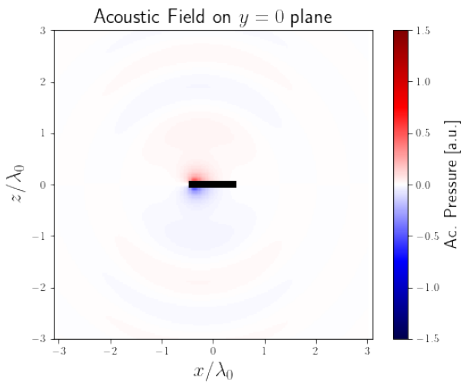

(g) Subcritical gust, y=0 plane

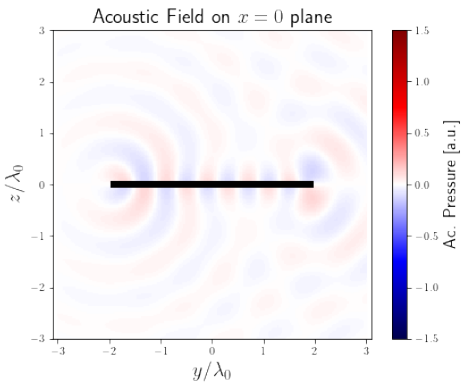

(h) Subcritical gust, x=0 plane

Figure 5.21: Near-field radiation over the 2D cut of airfoil

5.2 Propagation of noise

Now that the generation of wind turbine noise and its properties are studied and explained, the next step is propagation of this noise under different atmospheric conditions and for a varying source frequencies.

5.2.1 Parabolic equation model

No terrain

The propagation is first studied with no topography present, but with a surface impedance calculated from the formula of Delany and Bazley (1970), given as:

$$Z_g = z_0 \left(1 + 0.08 \left(\frac{f}{\sigma} \right)^{-0.754} \right) + i11.9 \left(\frac{f}{\sigma} \right)^{-0.732}, \tag{5.2}$$

where z_0 is the surface height [m], f is frequency [Hz], and σ = 60 $kNms^{-4}$ is the effective flow resistance used in this case. This surface impedance was kept constant for all cases, but could be changed in future work to study how it affects propagation in terms of absorption and reflection.

Figure 5.22 shows the transmission loss with height and range for the different cases. The transmission loss describe the decrease in intensity of a sound wave as it propagates outwards from a source (Kinsler et al., 1999). For each stability condition (unstable, neutral and stable), we ran the simulation for four different source frequencies; 100 Hz, 200 Hz, 300 Hz and 500 Hz. Wind turbines usually generate noise of low frequencies, up till 200 Hz. It is however interesting to see how the model responds to higher frequencies as well, managing to illustrate the variability of each stability condition better.

For a source frequency of 100 Hz, shown in Figures 5.22a), b), and c), the sound waves seem to have quite similar propagation behaviours for all stabilities. By increasing the frequency we observe how the source directs the noise emission in a more narrow manner. While for a low frequency the sound waves reflect upon the surface at approximately 200 m, the noise does not reflect on the ground until a 1000 m range for a frequency at 500 Hz. Looking back at Figure 4.4, we have a temperature inversion for the stable atmosphere, i.e. the temperature of the air increases with height, providing a sound speed profile, c, with the same characteristics. Transmitted sound waves always bend towards neighbouring regions of lower sound speeds, as formulated by Kinsler et al. (1999). Bending and refraction is therefore an evident feature in the propagation for a stable atmosphere, and can also be seen sign off at high frequencies under neutral conditions. Refraction is weakest at low frequencies. This can be explained by the wind and temperature gradients close to the ground becoming to small in scale compared to the wavelength of the sound. Refraction at low frequencies does therefore only occur at larger distances (Piercy et al., 1977). Downwards refraction have a tendency to enhance the sound level (Piercy et al., 1977), giving rise to the perception that noise

from wind turbines, especially the amplitude modulations, are louder at night, i.e. at stable conditions.

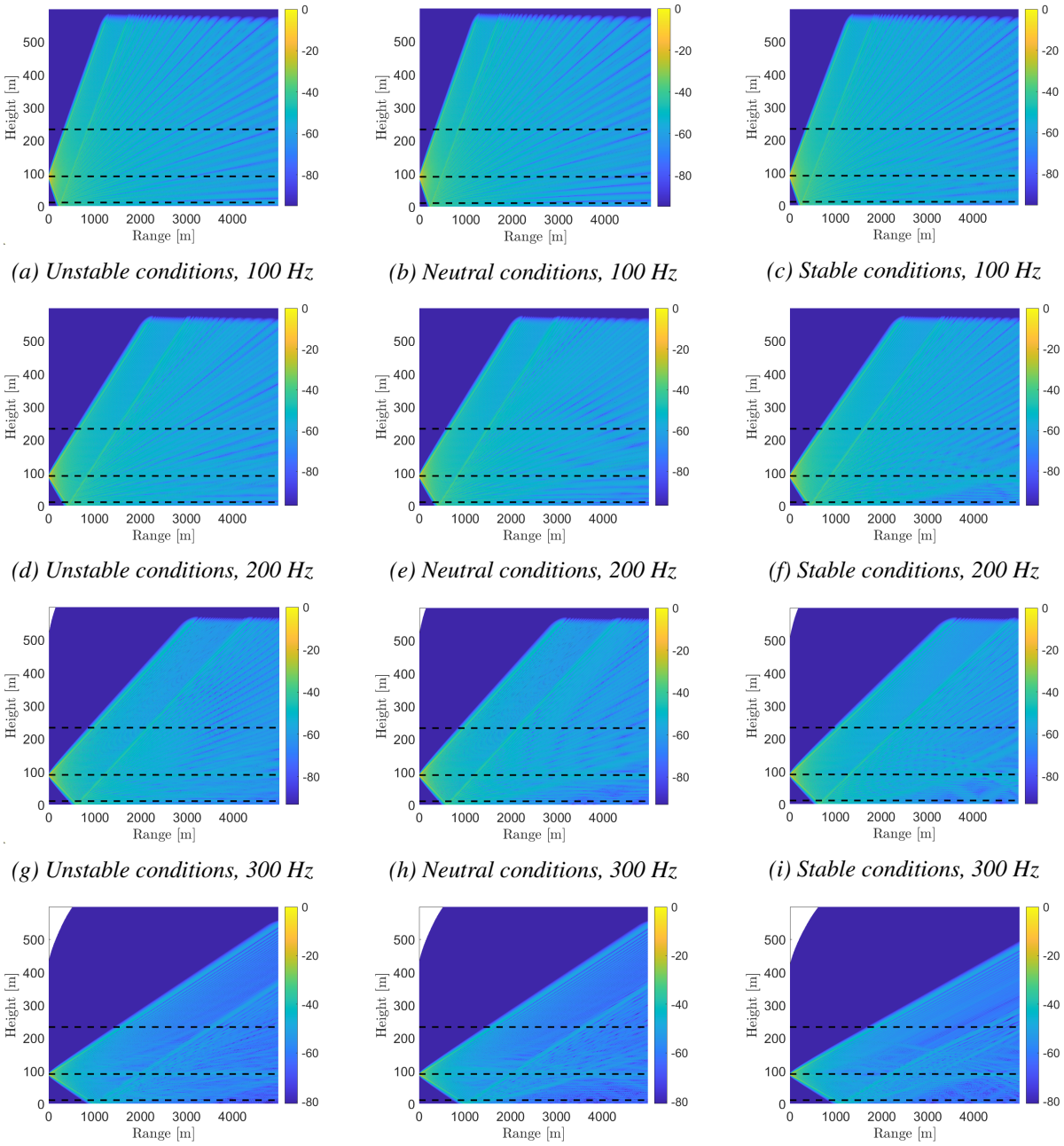

(a) Unstable conditions, 100 Hz *(b) Neutral conditions, 100 Hz* *(c) Stable conditions, 100 Hz*

(d) Unstable conditions, 200 Hz *(e) Neutral conditions, 200 Hz* *(f) Stable conditions, 200 Hz*

(g) Unstable conditions, 300 Hz *(h) Neutral conditions, 300 Hz* *(i) Stable conditions, 300 Hz*

(j) Unstable conditions, 500 Hz *(k) Neutral conditions, 500 Hz* *(l) Stable conditions, 500 Hz*

Figure 5.22: Transmission loss for three different stability conditions and for varying frequencies (100, 200, 300 and 500 Hz). Unstable condition, L = -100; Neutral condition, L = 0; Stable condition, L = 200. The black dotted lines indicate the heights 10 m, 90 m and 200 m. The colorbar shows the transmission loss [dB].

Wanting to study each stability condition further, the transmission loss at heights; 10 m, 90 m (hub height), and 200 m was plotted for all conditions and frequency cases. Values for the transmission loss at 1500 m range and 3000 m range at these three heights are listed in Table 5.4, with the difference between the two ranges seen in Table 5.5.

There is a clear correlation between an increase in frequency and the spreading of the sound waves, as discussed earlier. It is visualised in subfigures a) 10 m height and c) 200 m height for all stability conditions. For an unstable atmosphere, see Figure 5.23, the signal at 100 Hz reaches the 200 m height measurement point 1100 m before the high frequency signal of 500 Hz. The same applies to the measurement point at ground level (10 m), with higher frequencies travelling further before bending towards the ground. The transmission loss at hub height is always 0 dB at the source, with a rapid increase in transmission loss the first hundred metres, eventually fluctuating at levels between -45 dB and -70 dB. Studying the values listed in Table 5.4, we observe no noticeable relations for the different cases. Some comments can however be made.

The largest transmission loss in hub height at 1500 m distance from the source, is observed to be -66 dB for an unstable atmosphere with a source frequency of 300 Hz. At a distance of 3000 m the transmission loss for the same case have decreased with 7.5 dB, meaning the sound waves can have gained energy from higher altitudes where the sound is bending downwards or from sound waves reflected on the ground and back up in the atmosphere, and therefore decreases in a lesser rate than previously. If we compare the plots at 90 m height for a 500 Hz source with the plots of propagation, see Figure 5.22, we also here observe an increase in the plot around 2000 m range, corresponding to the range where the reflected sound waves from the ground converge with the original source signal.

Something of particular interest for the acceptance of wind turbines is the noise level at the surface, determining at which distance from houses wind farms can be built. It is therefore useful to study the difference in transmission loss at different ranges. The largest difference between the two ranges are for a neutral atmosphere with a source frequency of 500 Hz (see Figure 5.24), where the transmission loss increases by 18 dB by doubling the distance. For the unstable condition and a frequency of 200 Hz, we observe almost the same reduction. Figure 5.25 shows the transmission loss for a stable atmosphere.

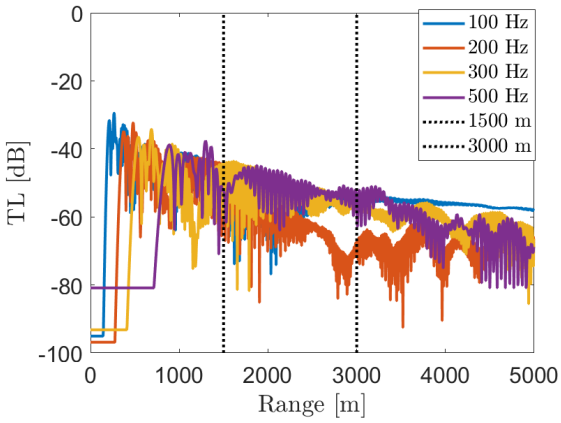

(a) 10 m height.

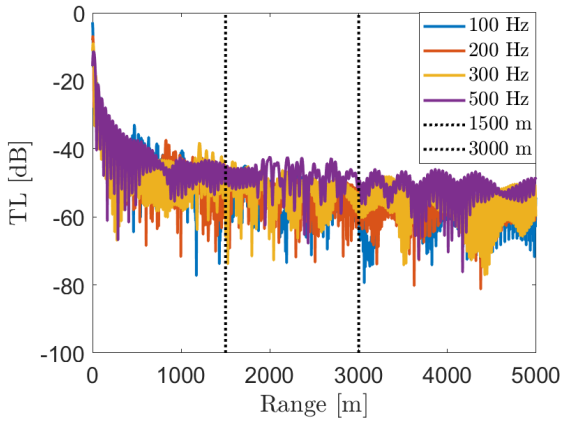

(b) 90 m height.

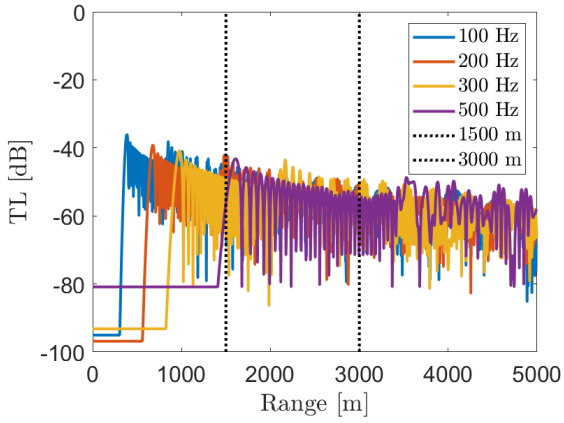

(c) 200 m height.

Figure 5.23: Comparison of transmission loss for an unstable atmosphere at three different heights; a) 10 m height (surface); b) 90 m height (hubheight); c) 200 m height. The black lines indicates the range at 1500 m and 3000 m.

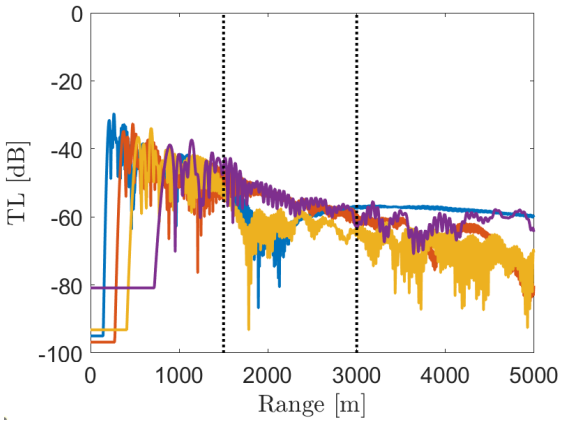

(a) 10 m height.

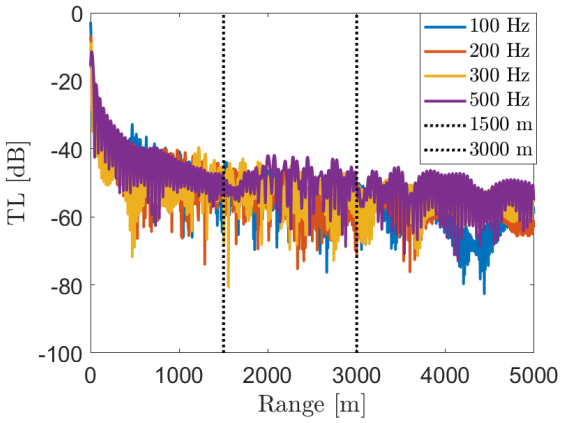

(b) 90 m height.

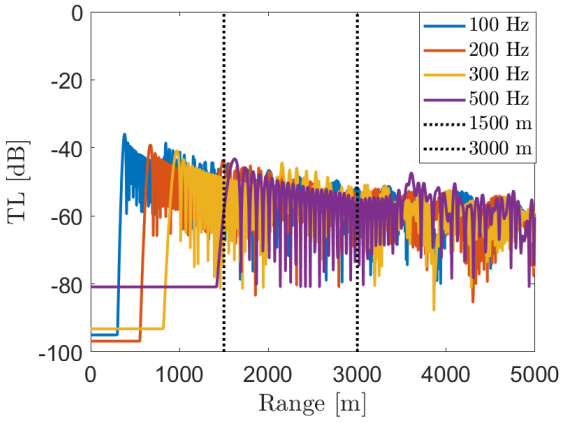

(c) 200 m height.

Figure 5.24: Comaprison of transmission loss for a neutral atmosphere at three different heights; a) 10 m height (surface); b) 90 m height (hubheight); c) 200 m height. The black lines indicates the range at 1500 m and 3000 m.

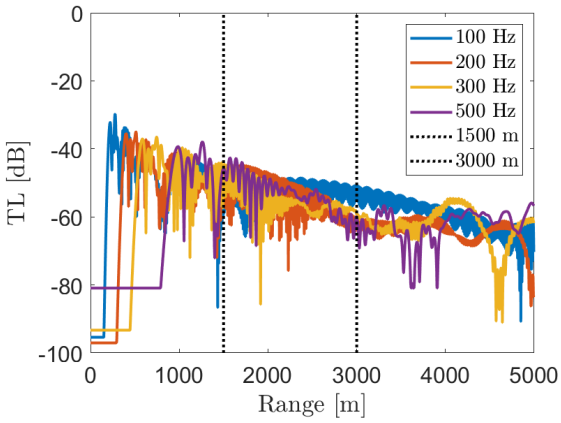

(a) 10 m height.

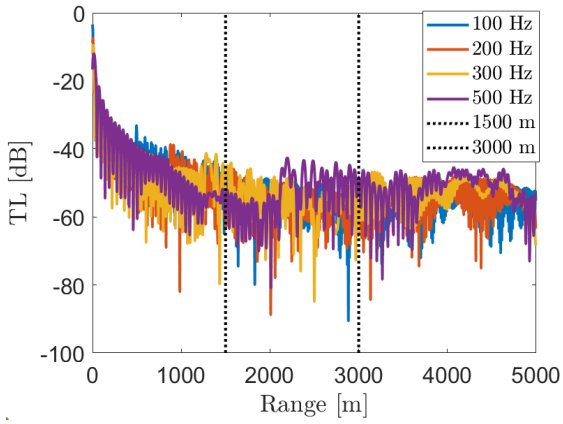

(b) 90 m height.

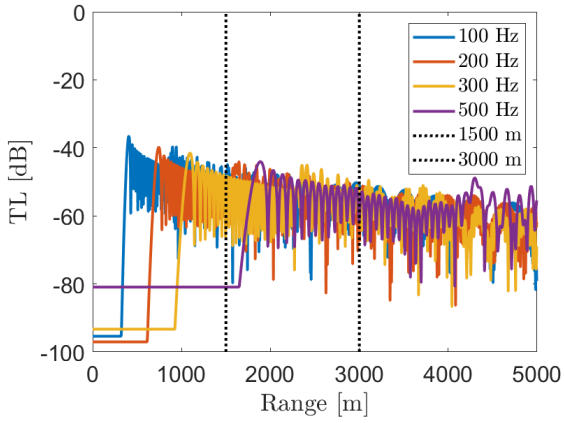

(c) 200 m height.

Figure 5.25: Comparison of transmission loss for a stable atmosphere at three different heights; a) 10 m height (surface); b) 90 m height (hubheight); c) 200 m height. The black lines indicates the range at 1500 m and 3000 m.

Table 5.4: Values of transmission loss [dB] for all three stability conditions at varying source frequencies measured at a range of 1500 m and 3000 m. No terrain.

Stability	Frequency [Hz]	TL [dB] at 1500 m range			TL [dB] at 3000 m range		
		10 m	90 m	200 m	10 m	90 m	200 m
Neutral	100	-52.08	-44.94	-64.56	-56.99	-57.39	-55.05
	200	-46.04	-51.87	-44.94	-62.08	-54.86	-58.69
	300	-52.13	-51.85	-51.19	-64.06	-58.17	-62.63
	500	-45.11	-49.21	-58.39	-63.16	-53.99	-55.55
Stable	100	-51.34	-48.65	-47.52	-50.74	-53.75	-57.29
	200	-47.27	-50.97	-63.35	-60.61	-51.25	-57.41
	300	-46.39	-47.79	-56.19	-59.30	-61.16	-54.13
	500	-45.74	-57.14	-80.92	-59.96	-46.26	-61.69
Unstable	100	-48.24	-48.10	-60.32	-55.19	-62.51	-52.00
	200	-52.92	-49.10	-50.81	-70.52	-56.20	-63.07
	300	-45.40	-65.88	-66.94	-57.36	-58.37	-53.55
	500	-52.39	-49.44	-56.10	-56.82	-68.18	-66.01

Table 5.5: The change in transmission loss between 1500 m and 3000 m for three heights and varying atmospheric stabilities and frequencies. No terrain.

Stability	Frequency [Hz]	Change in TL [dB]		
		10 m	90 m	200 m
Neutral	100	-4.91	-12.45	9.51
	200	-16.04	-2.99	-13.75
	300	-11.93	-6.32	-11.44
	500	-18.05	-4.78	2.84
Stable	100	0.60	-5.10	-9.77
	200	-13.34	-0.28	5.94
	300	-12.91	-13.37	2.06
	500	-14.22	10.88	19.23
Unstable	100	-6.95	-14.41	8.32
	200	-17.6	-7.19	-12.26
	300	-11.96	7.51	13.39
	500	-4.43	-18.74	-9.91

With terrain

Introducing terrain to the propagation model allows us to further investigate sound propagation and if it affects the transmission loss over distance in any way. A 70 m high and 200 m long obstruction was placed at an 800 m range from the sound source. This is the recommended distance between wind turbines and housings in Norway based on studies from NVE (2022a). As seen in Figure 5.26, this changes propagation behaviours in several cases. The first, most noticeable difference is that the area behind the obstruction experience a shadow zone, where the noise from the wind turbine does not reach the ground. The sound waves propagates from the top of the obstruction instead, in what seems to be the same angle as from the original source. We can observe a slightly stronger refraction at higher frequencies here than without the terrain, with it even being visible at lower frequencies in all three stability conditions.

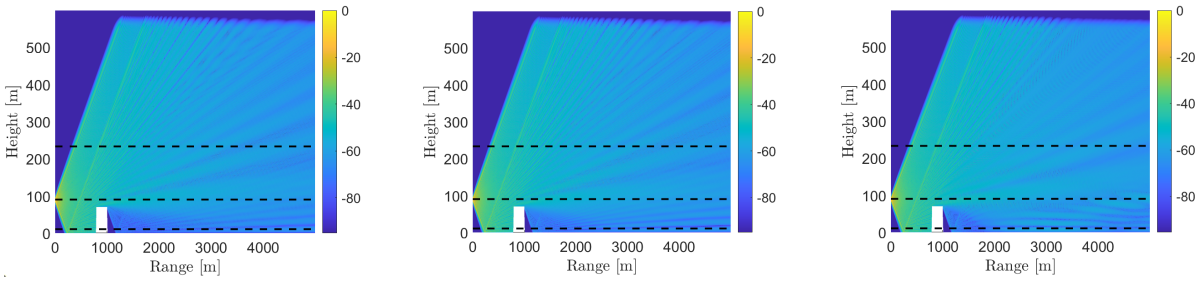

(a) Unstable conditions, 100 Hz

(b) Neutral conditions, 100 Hz

(c) Stable conditions, 100 Hz

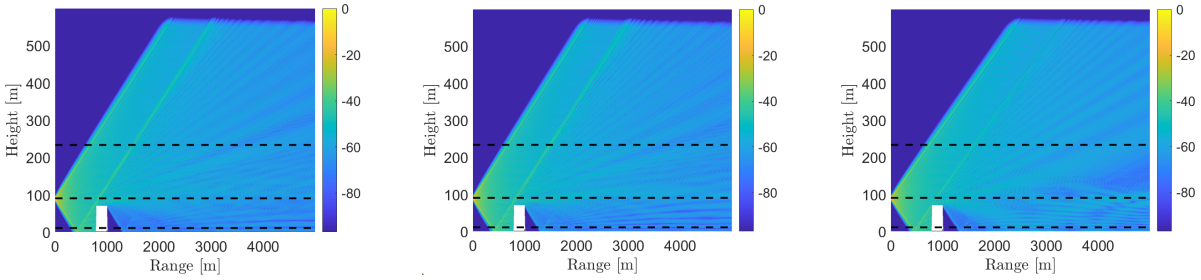

(d) Unstable conditions, 200 Hz

(e) Neutral conditions, 200 Hz

(f) Stable conditions, 200 Hz

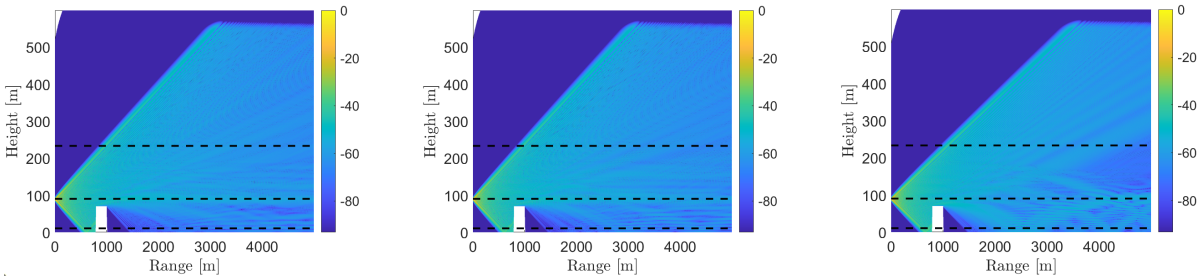

(g) Unstable conditions, 300 Hz

(h) Neutral conditions, 300 Hz

(i) Stable conditions, 300 Hz

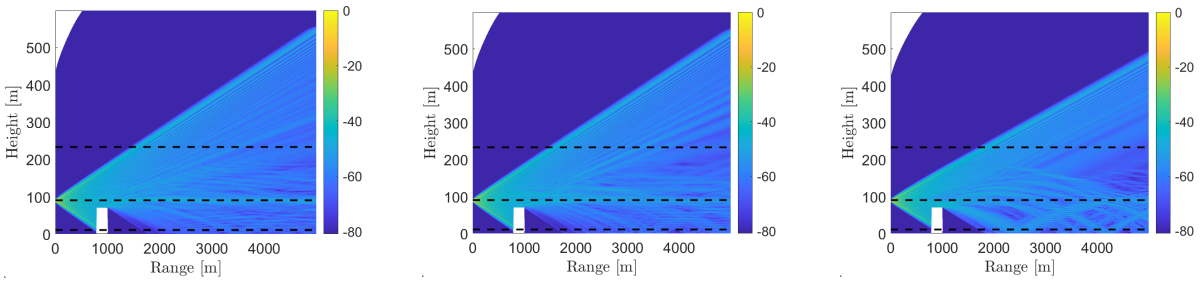

(j) Unstable conditions, 500 Hz

(k) Neutral conditions, 500 Hz

(l) Stable conditions, 500 Hz

Figure 5.26: Transmission loss for three different stability conditions and for varying frequencies (100, 200, 300 and 500 Hz) with terrain. Unstable condition, L = -100; Neutral condition, L = 0; Stable condition, L = 200. The black dotted lines indicate the heights 10 m, 90 m and 200 m. The colorbar shows the transmission loss [dB].

Figures 5.27, 5.28 and 5.29, shows the transmission loss at three different height for an unstable, neutral and stable atmosphere respectively. The transmission loss the first 800 m from the source is, as one would expect, identical to the previous tests with no terrain. After the obstruction there are clear differences, especially for the height close to the surface (10 m). Comparing the values in Table 5.4 and Table 5.6, the transmission loss measured at the first range checkpoint (1500m), is significantly higher at 10 m height when the obstruction is present. For a source frequency of 300 Hz, the difference with and without terrain is at staggering 40 dB for an unstable atmosphere.

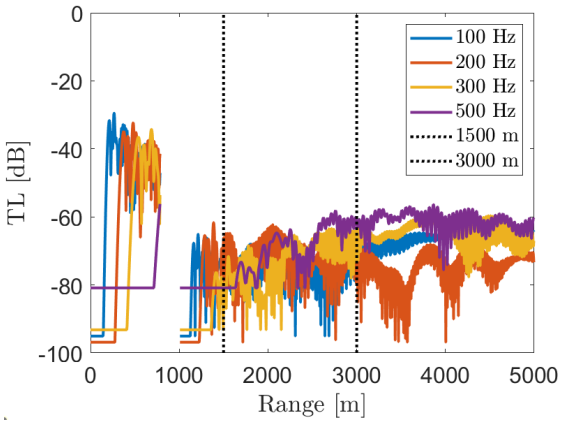

(a) 10 m height.

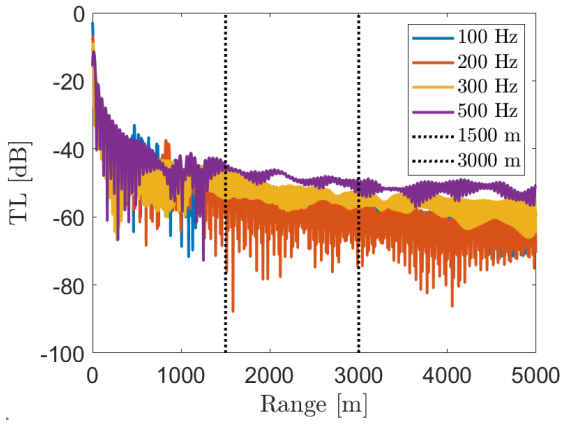

(b) 90 m height.

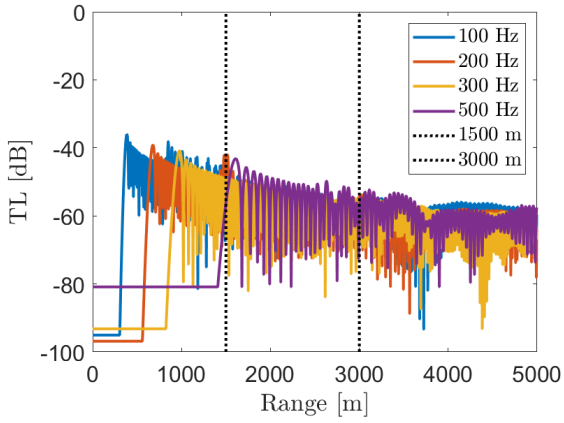

(c) 200 m height.

Figure 5.27: Comparison of transmission loss for an unstable atmosphere at three different heights; a) 10 m height (surface); b) 90 m height (hubheight); c) 200 m height. The black lines indicates the range at 1500 m and 3000 m.

While the transmission loss at 10 m height is generally lower for all three stability conditions at 1500 m range, it is interesting to study the values of transmission loss when increasing the distance in the case of a stable atmosphere. Table 5.7 shows how the transmission loss actually decreases by 12-16 dB for all variations of source frequency. The transmission loss at 3000 m therefore ends up at approximately the same levels as the ones calculated with no terrain.

At 200 m height, only very small variations in the case with terrain and without are observed, for either one of the checkpoints at 1500 m and 3000m. We therefore assume that the obstruction have minimal to none effect on the propagation at higher altitudes.

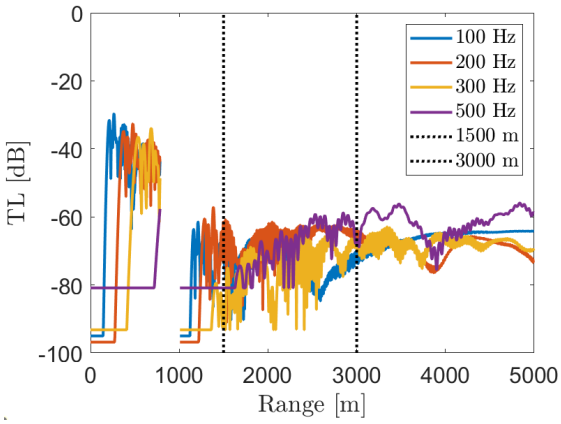

(a) 10 m height.

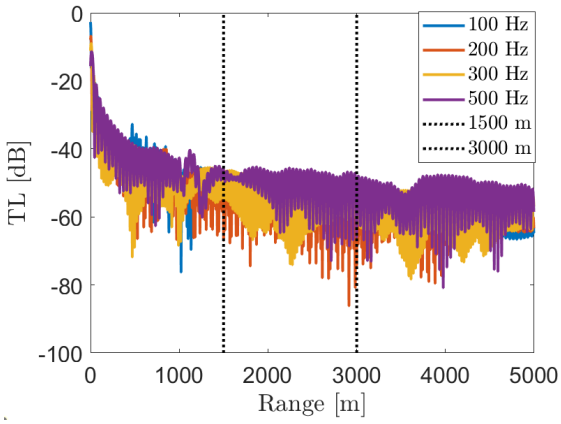

(b) 90 m height.

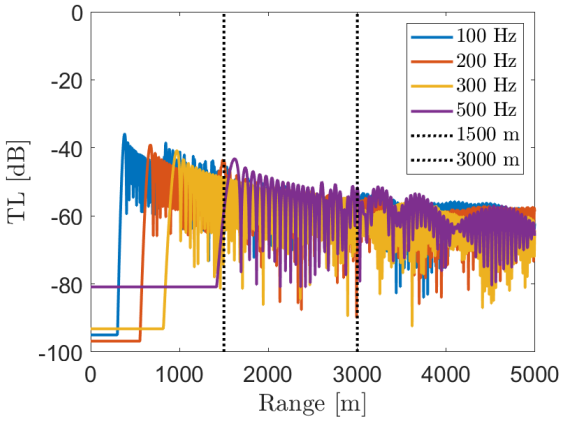

(c) 200 m height.

Figure 5.28: Comparison of transmission loss for a neutral atmosphere at three different heights; a) 10 m height (surface); b) 90 m height (hubheight); c) 200 m height. The black lines indicates the range at 1500 m and 3000 m.

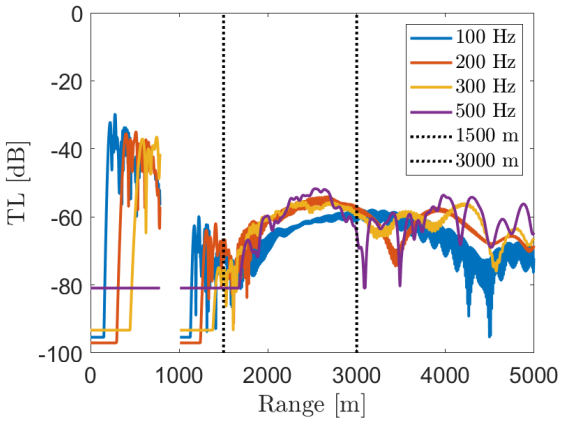

(a) 10 m height.

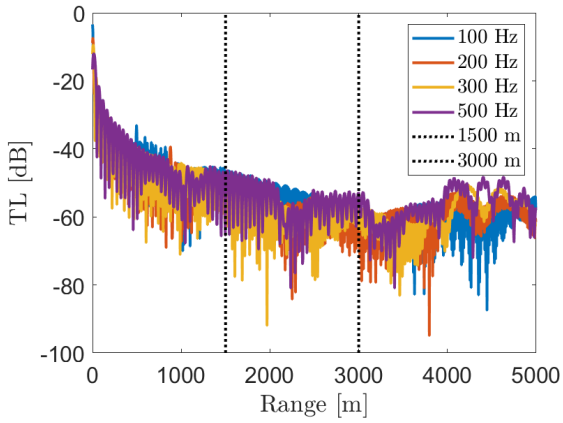

(b) 90 m height.

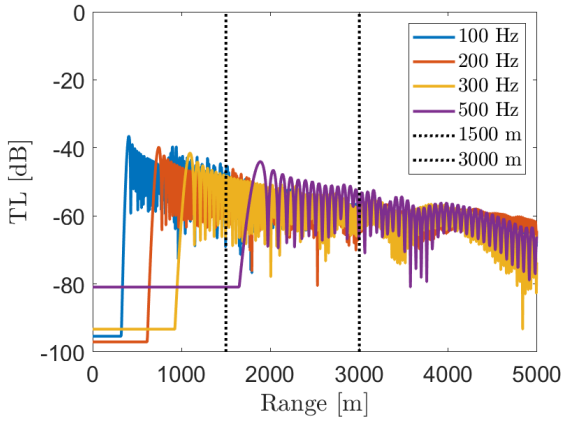

(c) 200 m height.

Figure 5.29: Comparison of transmission loss for a stable atmosphere at three different heights; a) 10 m height (surface); b) 90 m height (hubheight); c) 200 m height. The black lines indicates the range at 1500 m and 3000 m.

Table 5.6: Values of transmission loss [dB] for all three stability conditions at varying source frequencies measured at a range of 1500 m and 3000 m. With terrain.

Stability	Frequency [Hz]	TL [dB] at 1500 m range			TL [dB] at 3000 m range		
		10 m	90 m	200 m	10 m	90 m	200 m
Neutral	100	-66.30	-52.01	-65.38	-70.13	-54.76	-62.43
	200	-61.47	-66.89	-44.75	-66.68	-60.36	-55.59
	300	-86.46	-48.84	-51.19	-68.16	-53.09	-65.80
	500	-80.87	-46.18	-58.39	-66.64	-71.03	-51.69
Stable	100	-71.76	-48.54	-48.22	-59.21	-59.35	-59.11
	200	-72.08	-54.24	-63.34	-57.19	-60.47	-61.22
	300	-75.09	-50.02	-56.19	-58.79	-60.14	-62.35
	500	-80.92	-55.50	-80.92	-64.74	-54.31	-64.39
Unstable	100	-71.30	-47.25	-65.40	-75.06	-58.15	-56.63
	200	-66.10	-49.59	-50.55	-71.88	-57.74	-67.84
	300	-86.17	-47.81	-66.94	-64.03	-58.22	-54.95
	500	-80.87	-45.93	-56.10	-61.51	-64.51	-61.72

Table 5.7: The change in transmission loss from a range of 1500 m to 3000 m for three heights, varying atmospheric stabilities and frequencies. Including terrain.

Stability	**Frequency [Hz]**	**Change in TL [dB]**		
		10 m	**90 m**	**200 m**
Neutral	100	-3.83	-2.75	2.95
	200	-5.21	6.53	-10.84
	300	18.30	-4.25	-14.61
	500	14.23	-24.85	6.70
Stable	100	12.55	-10.81	-10.89
	200	14.89	-6.23	2.12
	300	16.30	-10.12	-6.16
	500	16.18	1.19	16.53
Unstable	100	-3.76	-10.9	8.77
	200	-5.78	-8.15	-17.29
	300	-22.14	-10.41	11.99
	500	19.36	-18.58	-5.62

Chapter 6

Summary and conclusion

Noise from wind turbines has been and will continue to be a key subject in studies and research in the pursuit of improving the overall performance and the environment in close proximity to the turbines. In this thesis, various models and techniques have been studied and tried implemented to give a holistic impression of the complexity of assessing noise generation and propagation from wind turbines in the atmosphere.

Despite not being able to implement beamforming in a rotating frame of reference, the method has been introduced together with the discussion of some advantages and disadvantages regarding the delay-and-sum approach. For future work, a natural extension would be to transform the measured pressure levels at the microphones into a rotating frame of reference and use this to make a more accurate acoustic source map.

The airfoil analysis using the Amiet model for leading edge noise has been proven important for the understanding of gust influence on surface pressure and near-field radiation. Next, a series of test cases were conducted with the parabolic equation method to study the acoustic pressure field with and without terrain under three different atmospheric stabilities and for varying frequencies. Here, it was illustrated how the propagation changes for a stable, neutral and unstable atmosphere. We did however not find any significant difference in transmission loss in the different tests, except for when introducing an obstacle in the propagation path. Further sensitivities should be explored and more comprehensive testing against observations made. It would be of interest to study the propagation variations when changing surface roughness, the height of the source and using other types of terrain.

Bibliography

ABB. Direct drive generators - ABB Permanent magnet (PM) generators (ABB wind turbine generators), 2019. URL https://new.abb.com/motors-generators/generators/generators-for-wind-turbines/permanent-magnet-generators/direct-drive-generators.

R. K. Amiet. Acoustic radiation from an airfoil in a turbulent stream. *Journal of Sound and Vibration*, 41(4):407–420, 8 1975. ISSN 0022-460X. doi: 10.1016/S0022-460X(75)80105-2.

Adnan Z. Amim. How Renewable Energy Can Be Cost-Competitive, 2015. URL https://www.un.org/en/chronicle/article/how-renewable-energy-can-be-cost-competitive.

Mohammed Ba Alawi. The integration of wind turbines for generating sustainable energy in skyscrapers. 2018.

Mostafa Bakhoday Paskyabi and Farzan Rashidi. Split Step Wavelet Galerkin Method Based on Parabolic Equation Model for Solving Underwater Wave Propagation. 2005.

Franck Bertagnolio, Helge Aa Madsen, Andreas Fischer, and Christian Bak. Validation of an aero-acoustic wind turbine noise model using advanced noise source measurements of a 500 kW turbine. *Open Archives of the 16th International Symposium on Transport Phenomena and Dynamics of Rotating Machinery, ISROMAC 2016*, pages 1–9, 2019.

P.J Bevel. Fourier Transform, 2010. URL https://www.thefouriertransform.com/.

Arno J. Brand, Joachim Peinke, and Jakob Mann. Turbulence and wind turbines. *J. Phys.: Conf. Ser.*, 318, 2011. doi: 10.1088/1742-6596/318/7/072005.

H.K Brock. The AESD Parabolic Equation Model. *Numerical Modeling Division Naval Oceanographic Laboratory*, 1 1978.

Thomas F. Brooks, D. Stuart Pope, and Michael A. Marcolini. Airfoil self-noise and prediction. *NASA Reference Publication*, (1218), 1989. ISSN 01488589.

Sofia Caires, Jan-Joost Schouten, Lasse Lønseth, Vegar Neshaug, Irene Pathirana, and Ola Storas. Uncertainties in offshore wind turbulence intensity. 2019.

Sigrid Carstairs. Windpower, Microplastics & Bisphenol-A Time to Bust the Myths and Discuss the Facts. | LinkedIn, 2021. URL https://www.linkedin.com/pulse/windpower-microplastics-bisphenol-a-time-bust-myths-facts-carstairs/.

Laura (International Energy Agency) Cozzi and Tim (International Energy Agency) Gould. World Energy Outlook 2021. pages 1–386, 2021. URL www.iea.org/weo.

M. E. Delany and E. N. Bazley. Acoustical properties of fibrous absorbent materials. *Applied Acoustics*, 3(2):105–116, 4 1970. ISSN 0003-682X. doi: 10.1016/0003-682X(70)90031-9.

Republic of South Africa Department of Energy. Noise levels of wind farms - fact sheet, 2018. URL http://www.energy.gov.za/files/windEnergyCampaign/NoiselevelsofwindfarmsFactSheet5.pdf.

Jian-Jiun Ding. Time Frequency Analysis Tutorial. 2017.

DNV. Produktpresentasjon: IEC 61400-11:2012, 2012. URL https://www.standard.no/no/Nettbutikk/produktkatalogen/Produktpresentasjon/?ProductID=1019323.

Alex Dopico. How do you calculate 1 3 octave band frequencies?, 2020. URL https://janetpanic.com/how-do-you-calculate-1-3-octave-band-frequencies/.

Esther Dornhelm, Helene Seyr, and Michael Muskulus. Vindby - A seriuos Offshore Wind Farm Design Game. *Energies*, 12, 2019.

A. P. Dowling and J. E. Ffowcs Williams. *Sound and Sources of Sound*. Ellis Horwood Limited, 1983.

Engineering Toolbox. Strouhal Number, 2014. URL https://www.engineeringtoolbox.com/strouhal-number-d_582.html.

Equinor. Floating wind, 2022. URL https://www.equinor.com/energy/floating-wind.

Paul C Etter. Advanced Applications for Underwater Acoustic Modeling. 2012:28, 2012. doi: 10.1155/2012/214839.

EU-Japan Centre. Offshore Wind Energy: Deepening EU-Japan Cooperation | Online Workshop | EU-Japan, 2021. URL https://www.eu-japan.eu/events/offshore-wind-energy-deepening-eu-japan-cooperation-online-workshop.

European Centre for Medium-Range Weather Forecasts. Friction velocity: Parameter details, 9 2019. URL https://apps.ecmwf.int/codes/grib/param-db/?id=228003.

European Commision. Wind Energy, 2022. URL https://ec.europa.eu/info/research-and-innovation/research-area/energy-research-and-innovation/wind-energy_en.

European Environment Agency. Glossary: Lden, 2001. URL https://www.eea.europa.eu/help/glossary/eea-glossary/lden.

European Environment Agency. EEA greenhouse gases, 2021. URL https://www.eea.europa.eu/data-and-maps/data/data-viewers/greenhouse-gases-viewer.

European Parliament. The European Green Deal. Technical report, 2019.

P D Fleming and S D Proben. The Evolution of Wind-Turbines : An Historical Review. 18:163–177, 1984.

Floating Wind Turbunes. Anchoring Systems - Floating Wind Turbines, 2022. URL http://floatingwindfarm.weebly.com/anchoring-systems.html.

Julius Fritzell. Sound propagation modelling with applications to wind turbines. (September), 2019.

Michelle Froese. How vortex generators boost wind-turbine performance and AEP, 10 2017. URL https://www.windpowerengineering.com/vortex-generators-boost-wind-turbine-performance-aep/.

J.R Garratt. *The atmospheric boundary layer*. Cambridge University Press., 1992.

GE Global Research. How loud is a wind turbine, 2014. URL https://www.ge.com/news/reports/how-loud-is-a-wind-turbine.

Kenneth E Gilbert and Michael J White. Application of the parabolic equation to sound propagation in a refracting atmosphere. *Citation: The Journal of the Acoustical Society of America*, 85:630, 1989. doi: 10.1121/1.397587. URL https://doi.org/10.1121/1.397587.

J. M.R. Graham. Similarity rules for thin aerofoils in non-stationary subsonic flows. *Journal of Fluid Mechanics*, 43(4):753–766, 1970. ISSN 14697645. doi: 10.1017/S0022112070002719. URL https://doi.org/10.1017/S0022112070002719.

Jørgen Grythe. Beamforming algorithms-beamformers. Technical report, Norsonic, 2015.

Joe Hammond and Paul White. Signals and Systems. In *Handbook of Signal Processing in Acoustics*. Springer, New York, NY, 2008.

Colin H. Hansen. Fundamentals of Acoustics. *American Journal of Physics - AMER J PHYS. 19.*, 1951. ISSN 0002-9505. doi: 10.1119/1.1932798. URL https://www.researchgate.net/publication/228726743_Fundamentals_of_acoustics.

Martin O L Hansen and Osti Did. Basic Rotor Aerodynamics applied to Wind Turbines. 1998.

Martin O.L. Hansen. *Aerodynamics of Wind Turbines*. 2008. ISBN 9789896540821.

John P. Harrison. Wind Turbine Noise. *Bulletin of Science, Technology & Society*, 31 (4):256–261, 2011. ISSN 0270-4676. doi: 10.1177/0270467611412549.

Erich Hau. *Wind Turbines: Fundamentals,Technologies, Application, Economics*, volume 2nd Editio. Springer Germany, 2006.

F. Casagrande Hirono, P. F. Joseph, and F. M. Fazi. An open-source implementation of analytical turbulence-airfoil interaction noise model. *Aiaa Aviation 2020 Forum*, pages 1–21, 2020. doi: 10.2514/6.2020-2544.

Home-X. Is 40 dB loud for a fridge?, 2022. URL https://homex.com/ask/is-40-db-loud-for-a-fridge.

Harvey H. Hubbard and Kevin P. Shepherd. Wind turbine acoustics. *NASA*, pages 153–183, 1988. doi: 10.2495/978-1-84564-205-1/05.

IEA. World Energy Outlook. 2019. URL https://www.iea.org/reports/africa-energy-outlook-2019.

IEA. Global Energy Review 2021. *Global Energy Review 2021*, 2021. doi: 10.1787/90c8c125-en.

INC Engineering Co. Ltd. Wind Turbine Noise Issues, 2022. URL https://www.ihi.co.jp/inc/laneng/consul/consul05.html.

International Energy Agency. Wind energy technology roadmap. *European Wind Energy Conference and Exhibition 2010, EWEC 2010*, 2013.

International Renewable Energy Agency. *Renewable Power Generation Costs in 2019*. 2020. ISBN 978-92-9260-244-4. URL https://www.irena.org/-/media/Files/IRENA/Agency/Publication/2018/Jan/IRENA_2017_Power_Costs_2018.pdf.

IRENA. *Future of Wind: Deployment, investment, technology, grid integration and socio-economic aspects*. 2019. ISBN 9789292601553. URL https://www.irena.org/-/media/Files/IRENA/Agency/Publication/2019/Oct/IRENA_Future_of_wind_2019.pdf.

John K. Kaldellis and D. Zafirakis. The wind energy (r)evolution: A short review of a long history. *Renewable Energy*, 36(7):1887–1901, 2011. ISSN 09601481. doi: 10.1016/j.renene.2011.01.002.

Jade Vande Kamp. What is a Spectrogram? - Signal Analysis - Vibration Research, 2020. URL https://vibrationresearch.com/blog/what-is-a-spectrogram/.

L.E. Kinsler, A.R. Frey, A.B. Coppens, and J.V. Sanders. *Fundamentals of Acoustics (4th Edition)*. 1999. ISBN 978-0-471-84789-2.

Kjeller Vindteknikk. Vindkart for Norge 9 2009. 2009.

Angeliki Koulouri and Jacopo Moccia. Saving water with wind energy. *Wind Europe*, 2014. URL www.ewea.org/report/saving-water.

Joyce Lee and Feng Zhao. Global Wind Report 2021. *Global Wind Energy Council*, pages 1 – 80, 2021. URL http://www.gwec.net/global-figures/wind-energy-global-status/.

Carlo; Lehto, Panu; Di Napoli. Signal analysis of wind turbine acoustic noise School of Electrical Engineering. page 80, 2014.

W. Y. Liu. A review on wind turbine noise mechanism and de-noising techniques. *Renewable Energy*, 108:311–320, 2017. ISSN 18790682. doi: 10.1016/j.renene.2017.02.034.

Clara Lohmann. TDBF - Delay-and-Sum Beamforming in the Time Domain, 2017. URL https://www.gfaitech.com/knowledge/faq/delay-and-sum-beamforming-in-the-time-domain.

Wei Ma, Huan Bao, Ce Zhang, and Xun Liu. Beamforming of phased microphone array for rotating sound source localization. *Journal of Sound and Vibration*, 467: 115064, 2020. ISSN 10958568. doi: 10.1016/j.jsv.2019.115064. URL https://doi.org/10.1016/j.jsv.2019.115064.

Rufin Makarewicz and Roman Gołębiewski. Amplitude Modulation of Wind Turbine Noise. *SF Journal of Aviation and Aeronautical Science*, 1, 2018. ISSN 2643-8119. URL https://scienceforecastoa.com/.

Rohith Mars, Vaninirappuputhenpurayil Gopalan Reju, Andy W.H. Khong, Yusuke Hioka, and Kenta Niwa. Beamforming techniques using microphone arrays. In *Academic Press Library in Signal Processing, Volume 7: Array, Radar and Communications Engineering*, pages 585–612. Academic Press, 1 2017. ISBN 9780128118870. doi: 10.1016/B978-0-12-811887-0.00012-2.

Heather Rae Martin. *Development of a scale model wind turbine for testing of offshore floating wind turbine systems*. PhD thesis, The University of Maine, 12 2009. URL https://citeseerx.ist.psu.edu/viewdoc/download?doi=10.1.1.456.3102&rep=rep1&type=pdf.

I McCowan. Microphone Arrays: A tutorial. (April):1–36, 2001.

P Moriarty and P Migliore. Semi-Empirical Aeroacoustic Noise Prediction Code for Wind Turbines. (December), 2003.

National Instruments. Understanding FFTs and Windowing Overview. 2020.

NORWEA. Faktaark: Vindkraft, plast og Bisfenol A., 2021. URL https://norwea.no/norwea-mener/2021/3/26/faktaark-vindkraft-plast-og-bisfenol-a.

NREL. Wind Powering America Fact Sheet Series Wind Energy Myths Wind Energy Myths Wind Energy Myths. *NREL*, 2005. URL www.eere.energy.gov/windandhydro/windpoweringamerica/pdfs/xcel_wind_.

NVE. Kunnskapsgrunnlag om virkninger av vindkraft på land - Støy, 2022a. URL https://nve.no/energi/energisystem/vindkraft/kunnskapsgrunnlag-om-virkninger-av-vindkraft-paa-land/stoey/.

NVE. Skyggekast fra vindturbiner , 2022b. URL https://nve.no/energi/energisystem/vindkraft/kunnskapsgrunnlag-om-virkninger-av-vindkraft-paa-land/skyggekast-fra-vindturbiner/.

NVE. Vindkraft, 2022c. URL https://www.nve.no/energi/energisystem/vindkraft/.

Christof Ocker, Esther Blumendeller, Philipp Berlinger, Wolfram Pannert, and Andrew Clifton. Localization of wind turbine noise using a microphone array in wind tunnel measurements. *Wind Energy*, (December 2020):1–19, 2021. ISSN 10991824. doi: 10.1002/we.2665.

S Oerlemans. Wind turbine noise : primary noise sources. pages 1–57, 2011.

Office of Energy Efficiency & Renewable. How do wind turbines work, 2013. URL https://www.energy.gov/eere/wind/how-do-wind-turbines-work.

Office of Energy Efficiency & Renewable Energy. Wind Energy Projects and Shadow Flicker, 2011. URL https://windexchange.energy.gov/projects/shadow-flicker.

Office of Energy Efficiency and Renewable Energy. How wind energy can help us breath easier, 2021a. URL https://www.energy.gov/eere/wind/articles/how-wind-energy-can-help-us-breathe-easier.

Office of Energy Efficiency and Renewable Energy. Wind Turbines: the Bigger, the Better | Department of Energy, 8 2021b. URL https://www.energy.gov/eere/articles/wind-turbines-bigger-better.

Edis Osmanbasic. The Future of Wind Turbines: Comparing Direct Drive and Gearbox | Engineering.com, 2020. URL https://www.engineering.com/story/the-future-of-wind-turbines-comparing-direct-drive-and-gearbox.

Panagiota Pantazopoulou. CHAPTER 20 Wind turbine noise measurements and abatement methods. In *Wind Power Generation and Wind Turbine Design*. 2010. doi: 10.2495/978-1-84564-/205-1. URL www.witpress.com,.

Ramón Pichs Madruga, Kristin Seyboth, Patrick Eickemeier, Patrick Matschoss, Gerrit Hansen, Susanne Kadner, Steffen Schlömer, Timm Zwickel, and Christoph Von Stechow. Renewable Energy Sources and Climate Change Mitigation Special Report of the Intergovernmental Panel on Climate Change Edited by Ottmar Edenhofer Youba Sokona. 2012. URL www.cambridge.org.

J E Piercy, T F W Embleton, and L C Sutherland. Review of noise propagation in the atmosphere. *Citation: The Journal of the Acoustical Society of America*, 61:1403, 1977. doi: 10.1121/1.381455. URL https://doi.org/10.1121/1.381455.

J.N. Pinder. Mechanical Noise from Wind Turbines. *Wind Engineering*, 16(3):158–168, 1992.

Trevor J Price. James Blyth-Britain's first modern wind power pioneer. *Wind Engineering*, Volume 29(No.3):191–200, 2005.

K. Deergha Rao and M.N.S. Swamy. Spectral Analysis of Signals. *Digital Signal Processing*, pages 721–751, 2018. doi: 10.1007/978-981-10-8081-4{_}12. URL https://link.springer.com/chapter/10.1007/978-981-10-8081-4_12.

Anthony L. Rogers, James F. Manwell, and Sally Wright. Wind Turbine Acoustic Noise. *Renewable Energy Research Laboratory. Department of Mechanical and Industrial Engineering. University of Massachusetts at Amherst*, 2002. ISSN 09574565.

Yannick Rozenberg and Gilles Robert. Wall-Pressure Spectral Model Including the Adverse Pressure Gradient Effects. 2012. doi: 10.2514/1.J051500. URL http://arc.aiaa.org.

Leandro De Santana. Fundamentals of Acoustic Beamforming. pages 1–26, 2017.

SKYbrary Aviation Safety. Stall , 2020. URL https://skybrary.aero/articles/stall.

Statkraft. Fosen Vind, 2021. URL https://www.statkraft.com/about-statkraft/where-we-operate/norway/fosen-vind/.

Roland B. Stull. *An Introduction to Boundary Layer Meteorology*. Kluwer Academic Publishers, Vancouver, 1 edition, 1988. URL https://ebookcentral.proquest.com/lib/bergen-ebooks/reader.action?docID=3108101#.

Svensk Vindenergi. Vindkraften är hållbar. 2021. URL https://svenskvindenergi.org/wp-content/uploads/2021/05/Vindkraften-ar-hallbar-ett-faktablad-fran-Svensk-Vindenergi.pdf.

Robert Z. Szasz and Laszlo Fuchs. Wind turbine acoustics. *WIT Transactions on State of the Art in Science and Engineering*, 34:1755–8336, 2010. ISSN 1755-8336. doi: 10.2495/978-1-84564. URL https://www.witpress.com/Secure/elibrary/papers/9781845642051/9781845642051005FU1.pdf.

The Editors of Encyclopedia. Acoustic impedance, 2017. URL https://www.britannica.com/science/acoustic-impedance.

The FuE-Zentrum FH Kiel GmbH. FINO1 - research platform in the North Sea and the Baltic No. 1, 2022. URL https://www.fino1.de/en/.

The Offshore Boundary-Layer Observatory. The OBLEX-F1 measurement campaign, 2016. URL https://oblo.w.uib.no/activities/the-oblex-f1-measurment-campaign/.

Y Tian and B Cotté. Wind Turbine Noise Modeling Based on Amiet's Theory: Effects of Wind Shear and Atmospheric Turbulence. *ACTA ACUSTICA UNITED WITH ACUSTICA*, 102:626–639, 2016. doi: 10.3813/AAA.918979.

Yuan Tian. Modeling of wind turbine noise sources and propagation in the atmosphere. 2016. URL https://tel.archives-ouvertes.fr/tel-01335869v2.

Renzo Tonin. Sources of wind turbine noise and sound propagation. *Acoustics Australia*, 40(1):20–27, 2012. ISSN 08146039.

Luís Filipe da Conceição Vargas. Wind Turbine Noise Prediction. 2008.

Saeed V Vaseghi. *Advanced Digital Signal Processing and Noise Reduction, 3rd Edition*. John Wiley & Sons, Ltd, 2006.

Vestas. V236-15.0 MW, 2022. URL https://www.vestas.com/en/products/offshore/V236-15MW.

M. West, K. Gilbert, and R. A. Sack. A tutorial on the parabolic equation (PE) model used for long range sound propagation in the atmosphere. *Applied Acoustics*, 37(1): 31–49, 1992. ISSN 0003682X. doi: 10.1016/0003-682X(92)90009-H.

Wind Denmark. Fakta om grøn energi | Green Power Denmark, 2022. URL https://greenpowerdenmark.dk/fakta-om-groen-energi.

Wind Europe. Cross-sector industry platform outlines best strategies for the recycling of wind turbine blades | WindEurope, 2020. URL https://windeurope.org/newsroom/press-releases/cross-sector-industry-platform-outlines-best-strategies-for-the-recycling-of

Wind Europe. About Wind Energy, 2022a. URL https://windeurope.org/about-wind/history/.

Wind Europe. Environment & planning, 2022b. URL https://windeurope.org/policy/topics/environment-planning/.

World Health Organization. Health consequences of air pollution on populations, 2019. URL https://www.who.int/news/item/15-11-2019-what-are-health-consequences-of-air-pollution-on-populations.

Werner Würz. Gust Wind Tunnel, 2022. URL https://www.iag.uni-stuttgart.de/en/institute/test-facilities/gust-wind-tunnel/.

Xunren Yang. *Atmospheric Acoustics*. De Gruyter, Inc., 2016. URL https://ebookcentral.proquest.com/lib/bergen-ebooks/reader.action?docID=4587092&ppg=236.